Impurity Injection Experiments on the Alcator C-Mod Tokamak

by

Michael A. Graf

B.A.Sc., University of Toronto (1990)

Submitted to the Department of Nuclear Engineering
in partial fulfillment of the requirements for the degree of

Doctor of Philosophy

at the

MASSACHUSETTS INSTITUTE OF TECHNOLOGY

June 1995

Signature of Author .....
Department of Nuclear Engineering
May 12, 1995

Certified by .....
James L. Terry
Research Scientist, Plasma Fusion Center
Thesis Supervisor

Certified by .....
Ian H. Hutchinson
Professor, Department of Nuclear Engineering
Thesis Reader

Accepted by .....
Allan F. Henry
Chairman, Departmental Graduate Committee

Impurity Injection Experiments on the Alcator C-Mod Tokamak

by

Michael A. Graf

Submitted to the Department of Nuclear Engineering
on May 12. 1995, in partial fulfillment of the
requirements for the degree of
Doctor of Philosophy

ABSTRACT

A number of impurity injection experiments has been performed on the Alcator C-Mod tokamak. A laser ablation impurity injection system has been built and operated successfully. In conjunction with a high resolution survey VUV spectrometer and various other spectroscopic diagnostics, this injector system has been used to measure impurity transport behaviour during a variety of operating conditions. Measurements of the impurity confinement time have been made for a range of plasma parameters and scaling relationships have been developed. Modelling of the impurity transport has also been conducted using the MIST code. Substantial improvements have been made to the database of atomic physics rate coefficients for molybdenum as a result of this thesis. Agreement between modelled and observed spatial profiles of high charge states of molybdenum is now good. This modelling has been used to infer intrinsic molybdenum concentrations in the plasma during a variety of operating conditions including high power RF operation. Experiments which measure the screening efficiency of the plasma with respect to an external source of impurities have also been conducted using the laser ablation system as well as an impurity gas injection system and have shown that more than 90% of the source impurities are typically kept out of the main plasma during diverted operation. The impurity modelling developed as part of this thesis has also been extended to the measurement of neutral hydrogen density profiles by making use of charge exchange reactions with injected impurity ions. Strong up-down asymmetries in these profiles have been observed during diverted operation.

Thesis Supervisor: James L. Terry
Title: Research Scientist, Plasma Fusion Center

Thesis Reader: Ian H. Hutchinson
Title: Professor, Department of Nuclear Engineering

Acknowledgements

The author would like to thank all of the people involved in the completion of this thesis. As with any project performed as part of a large group, there have been significant contributions made by countless individuals. I will do my best to acknowledge as many of them here as I can.

Thanks to all of my classmates over the years. Artur, Chris, Tom Gerry, Chris, Pete, Darren, John, Tom. Jeff, Dave, Jim, Dan, Paul, Ying, Rob, Mark, etc..., have all helped to make what might have otherwise been unbearable, a lot more fun.

Thanks to J.G. for teaching me how to slow down my backswing by letting me watch his, to J.R. for at least always calling 'around' before hitting me with the ball, and to Valerie for always coming up with a reason to take lunch.

Thanks to my supervisor, J.T., for his infinite patience and constant guidance during what must have, at times, seemed like a long five years. Your friendship is one of the most highly valued things which I bring away from my experiences here.

Thanks as well to my thesis reader, Ian Hutchinson, for helping to steer the course of my development as part of the C-Mod group and for his patience in reviewing the final product.

Many thanks to the scientists and engineers who have made C-Mod the highly successful program that it is. Thanks to Steve Wolfe, Steve Horne, Bob Granetz, John Goetz, Earl Marmar, and the other physics operators who routinely run the machine with skill and daring. Thanks to Vinnie, Andy, Sam, Jerry, Wanda, Bill, Bob, Tommy, and the others who provide the engineering support without which none of this work could have been accomplished. A special thank you to Frank Silva for helping to keep a prospective physicist's feet on the ground and head out of the clouds (among other places).

Much of the data used in this thesis arose from the ongoing research of a number of individuals. In particular, the hardware used to produce the x-ray spectra was built and operated by John Rice. Many thanks to him for sharing his expertise and friendship

over the years, both in the areas of hardware design and atomic physics modelling. The bolometry data were generated by John Goetz, whose tireless efforts at finding the perfect inversion algorithm are much appreciated. The Z_{eff} data were generated by Earl Marmar and Cindy Christensen. Gratitude is expressed to them for tolerating endless badgering about their calibrations. I would also like to thank Mark May for designing and building the MLM instrument and allowing us to use it as extensively as we have. Many of the results contained herein would not have been possible without his efforts.

My family also deserves heartfelt thanks for the support (both emotional and financial) they have provided throughout my academic career. I would not be who I am today without you.

Finally, a special note of thanks to Jane, to whom this thesis is dedicated, for her love and understanding over the past five years. For encouraging me when I needed it, and for helping me to keep the proper perspective, I am deeply grateful.

Contents

List of Figures

List of Tables

Chapter 1

Introduction

1.1 Nuclear Fusion and the Tokamak Concept

1.1.1 The Tokamak

The tokamak has long been one of the leading concepts for making nuclear fusion a viable energy source. The tokamak concept was first introduced in the 1950's in the Soviet Union [1]. Since then, dozens of machines of varying complexity have been built to investigate various aspects of tokamak plasmas. Today the tokamak represents the dominant effort in the field of magnetic confinement fusion research. A brief overview of the characteristics which make the tokamak unique is therefore appropriate at this time.

A tokamak relies on a large toroidal magnetic field (usually denoted B_ϕ or B_t) and large toroidal plasma current, I_p, to confine electrons and ions in a toroidal vacuum chamber. The plasma current is typically generated by the application of a toroidal loop voltage induced by a solenoidal winding at the center of the torus. In addition to the magnetic field applied in the toroidal direction and those generated by the plasma current itself, various other external magnetic fields are applied in order to ensure a radial force balance and maintain a plasma which is in a state of magnetohydrodynamic (MHD) stability. Yet other external fields may be applied to the plasma in order to produce

specific shapes or transient motions. Numerous additional coils are generally required to produce these fields. A typical arrangement for these coils for the Alcator C-Mod tokamak is shown in Figure 1-1 along with a typical highly shaped plasma which they are capable of producing [2].

1.1.2 The Alcator C-Mod Tokamak

The Alcator C-Mod tokamak at the Plasma Fusion Center at MIT is the device on which all of the experimental work for this thesis was performed. This tokamak is the third in a series of high field, high density, compact tokamaks built at MIT since the 1970's. The name Alcator derives from the italian *Alto Campo Torus* meaning 'high field torus' and is indicative of the philosophical approach taken in the design of all the tokamaks in the Alcator series. The first such tokamak, Alcator A, went into operation in 1976 and had a major radius of 0.54 m, a minor radius of 0.10 m, and a toroidal field on axis of 8 Tesla. Discharges in Alcator A typically lasted a few hundred milliseconds, carried plasma currents of up to 400 kA, and achieved central electron temperatures of up to 2 keV. Alcator C, the next machine in the series went into operation in 1978 with a major radius of 0.64 m, a minor radius of 0.16 m, and a toroidal field of 13 Tesla. Discharges in Alcator C also were typically a few hundred milliseconds in duration with plasma currents of up to 800 kA and central electron temperatures of about 2 keV. The present machine, Alcator C-Mod, saw its first plasmas in 1992. To date it has operated highly shaped plasmas with major a radius of up to 0.69 m, minor radius of up to 0.23 m, and toroidal field of 5.4 Tesla. Plasma currents of over 1 MA have been achieved in discharges which last up to 1.5 seconds. Central electron temperatures over 4 keV have also been observed. These major machine parameters and how they compare with the previous generations of the Alcator series are summarized in Table 1.1.

Alcator C-Mod represents a major improvement over the previous two machines in the series both in terms of expected performance and in operational flexibility. The ability to produce highly elongated plasmas with either single or double null divertor configura-

	Alcator A	Alcator C	Alcator C-Mod
operation period	1976-1981	1978-1986	1992-?
major radius (m)	0.54	0.64	0.69
minor radius (m)	0.1	0.16	0.22
toroidal field (T)	8	13	5.3 (9)
plasma current (MA)	0.4	0.8	1.2 (3)
line averaged density ($10^{20}m^{-3}$)	1.0-10	1.0-10	0.8-4.0
central electron temperature (keV)	2	2.5	4 (6)
discharge duration (s)	.5	.5	1.5 (7)
plasma elongation	1.0	1.0	1.0-1.8
plasma cross-section	limited	limited	diverted

Table 1.1: Comparison of major machine parameters in the Alcator series. Values in parentheses are expected for future operation.

tions allows for the investigation of entirely new modes of operation which were wholly unavailable in the previous machines. Divertor studies therefore represent a major area of emphasis in the C-Mod program. Important questions which need to be addressed in the area of divertor studies include those related to the impurity behaviour characteristics. Specifically, any differences in either impurity transport or source rates between diverted and limited discharges need to be investigated. If the divertor concept is to live up to expectations, it is necessary that it provide some significant benefit in the area of impurity particle control and power handling capability.

Another major area of emphasis in the C-Mod program is the use of large amounts of auxiliary heating power. Specifically, ion cyclotron range-of-frequencies (ICRF) heating waves in the 80 MHz range are introduced via two antennas at levels of up to 4 MW at present. Efforts at ICRF heating in Alcator C and A were made at only the few hundred kilowatt level. Alcator C-Mod offers the possibility of one day investigating ICRF powers of up to 8 MW. This represents a significant extension of capabilities. Important questions which need to be addressed at these high auxiliary power densities include the effects on either impurity transport or impurity source rates. It was observed on Alcator C that even small amounts of RF power led to serious impurity problems [3]. If the results obtained there were to be extrapolated to the anticipated powers planned

for C-Mod, the level of impurity radiation expected would be prohibitive.

Underlying all of the major areas of emphasis in the C-Mod program is another very unique feature found in a tokamak of this size and performance, namely the choice of material for the plasma facing components (PFCs). While most other tokamaks opt for PFCs of as low Z material as possible (carbon and beryllium are two common choices), the Alcator line of tokamaks has experimented with high Z wall materials instead. Alcator C-Mod is equipped with PFCs made entirely of molybdenum. The philosophy behind this selection is related to the compatibility of these high Z materials, or rather, the suspected incompatibility of more common low Z materials with any fusion reactor with a high power density. C-Mod in particular presents an opportunity to evaluate one candidate high Z material under the highest power density conditions of any major tokamak operating today. In conjunction with smaller machines around the world, significant additions to a database of results obtained with high temperature, fusion plasmas are being made. Some of the reasons why these contributions are necessary and important can be found in the discussion of plasma impurities below.

1.2 Plasma Impurities

Plasma impurities play an important role in tokamaks for a number of reasons. Their presence can affect plasma performance in various ways, some of which are detrimental and some of which are not. A few of these effects are discussed below.

The ultimate goal of a fusion reactor is to provide a net source of energy. To do this, a state of energy 'breakeven' in which the fusion energy produced in the plasma is equal to the total energy losses it experiences must first be achieved. One of the factors which limits the realization of this goal is the large amount of energy which is lost from the plasma via radiation. The principal mechanisms by which energy is radiated from the plasma include line radiation, bremsstrahlung, and recombination. Each of these mechanisms scales rather strongly with the amount of impurity present in the plasma

(see Chapter 6) and with the atomic number, Z, of the impurity species. It can be shown [4] that for even relatively small concentrations of some impurities in the plasma, sufficient energy would be lost via radiation to prevent a breakeven condition from being achieved. This problem is significant enough in machines with only low Z intrinsic impurities such as carbon or oxygen but is potentially increased many-fold when high Z impurities such as molybdenum (Z=42) need to be considered.

In addition to enhanced radiative losses, plasma impurities also serve to dilute the working fuel ions (H isotopes, typically). Given the quasi-neutral requirement of tokamak plasmas and the operational constraint that the electron density in the tokamak be held below some maximum value determined by macroscopic parameters such as the plasma current, machine size, and toroidal field strength [5, 6], and the fact that each impurity atom contributes many more electrons to the plasma than does each fuel atom poses a serious limitation on the fuel ion density which is realizable.

One application in which impurities may prove beneficial to tokamak performance involves control of power deposition in diverted plasmas. The divertor concept, as outlined above, seeks to direct the magnetic field lines from the edge of the plasma onto specially designed target plates in the hopes of reducing impurity influx. Much work has been done both experimentally and theoretically in recent years with different divertor geometries and wall materials with the goal of finding an optimum solution compatible with future reactor-type operational constraints.

It is becoming increasingly clear that in order to deal successfully with the large power fluxes which are predicted for next generation machines, schemes which are able to dissipate this power before it actually reaches the divertor target plate must be found. One such scheme involves creating a highly radiating region around the edge of the plasma. This radiating region would serve to reduce the flux of power flowing along the field line to the plate by reducing the ion and electron temperature on the field lines leading to the target. One effective way of establishing such a radiating region is believed to be through the introduction of controlled amounts of impurities with radiative

characteristics tailored to the existing edge plasma parameters. For such a scheme to be successful, the behaviour of the impurity after its introduction into the plasma must be understood to ensure that its detrimental effects do not outweigh any advantage it may provide.

1.3 Standard Tokamak Diagnostics

The diagnostics used to observe tokamak plasmas are many and varied according to the nature of the quantity being diagnosed. Generally, though, diagnostics can fall into the categories of measuring either electromagnetic fields, radiation, or particles. For the purposes of this thesis, most direct observations of the effects of impurities on the tokamak plasma are obtained via measurements of radiation. The analysis which is required to interpret properly those observations, however, makes necessary use of a large number of other diagnostic systems. Some of these are described below. Other key diagnostics, such as those that measure electron density and temperature are described throughout the text of this thesis as appropriate.

1.3.1 Magnetic Diagnostics

Central to diagnosing the position and shape of the plasma is an extensive array of magnetic diagnostics which measure magnetic field, magnetic flux, and plasma current at a number of discrete locations around the vacuum vessel [7]. The measurements are then used to reconstruct the shape of the magnetic surfaces both inside and outside the plasma. This reconstruction is done with the EFIT code [8] and routinely provides a reliable calculation of the plasma magnetic geometry. The instances where this magnetic geometry is important to the interpretation of spectroscopic observations are noted throughout this thesis.

1.3.2 X-Ray Spectroscopy

A crystal x-ray spectrometer array with high energy resolution is used on Alcator C-Mod for observing line emission in the 2.5-4.0 Å region of the spectrum [9]. Each of the five von Hamos type spectrometers can be independently positioned to give a radial view of the plasma along chords with an overall coverage of impact parameters at the magnetic axis which range from about 32 cm below to about 32 cm above the midplane. Note that this range of possible views extends almost to the lower x-point of typical diverted discharges. Chapters 4 and 8 describe ways in which this spatial coverage has been exploited for the purpose of measuring profiles of certain intrinsic plasma impurities and neutrals respectively. This x-ray spectrometer array is also absolutely calibrated for sensitivity through a consideration of crystal reflectivity and beamline and detector geometries.

In addition to the high resolution x-ray spectrometers, there also exist four separate filtered arrays of 38 p-i-n diodes providing spatial coverage of most of the plasma cross-section during typical operation [10]. The extent of this coverage is shown in Figure 1-2. Each chord of these arrays provides a high time resolution line integrated brightness measurement of soft x-ray emission in the plasma. The spatial resolution of each chord is about 10 mm at the nominal plasma major radius in the poloidal plane and about 10 mm in the toroidal plane. The diodes are filtered with beryllium foil which serves to cut off photons with energy less than about 1 keV. This limits the response of the arrays to photons of wavelength less than about 10 Å. The short wavelength limit of the arrays is determined by the thickness of the diodes themselves. In this case, the diodes are sensitive to photons of energies up to about 10 keV. Tomographic inversion of the brightness signals obtained by these arrays is routinely done to yield emissivity profiles of soft x-ray emission.

1.3.3 Visible Bremsstrahlung

A quantity which provides a convenient measure of the total contamination of the plasma by impurities is known as Z_{eff} and can be defined as:

$$Z_{eff} = \frac{\sum n_i Z_i^2}{\sum n_i Z_i} \tag{1.1}$$

where n_i and Z_i are the total density and the charge of species i in the plasma. A pure hydrogen (or deuterium) plasma will therefore have $Z_{eff} = 1$. This definition of Z_{eff} arises conveniently from a consideration of the bremsstrahlung radiation emitted by the plasma. It can be shown (see Chapter 6) that the rate at which bremsstrahlung radiation is emitted is proportional to Z_{eff}. This quantity can therefore be thought of as the factor by which the total bremsstrahlung emission from the plasma exceeds that of a pure hydrogen (or deuterium) plasma at the same electron density.

The total bremsstrahlung emission profile from the plasma is measured using an array of 32 absolutely calibrated chordal views of the plasma coupled to an array of photomultiplier detectors. The array views the plasma through an interference filter which selectively passes photons in a narrow band about 4600 Å [11]. Emission in this range, which lies in the visible region of the spectrum, is known to contain no strong line emission from any typical plasma impurity species and is therefore dominated by bremsstrahlung continuum. An absolute measurement of the bremsstrahlung emission in this spectral region can therefore be used, along with the local electron density and temperature, to calculate the local Z_{eff} of the plasma. In practical terms, the array gives a bremsstrahlung brightness profile which is then inverted using standard techniques to yield an emissivity profile.

A note of caution should be given at this time regarding the inversions done using these bremsstrahlung data. Since the bremsstrahlung emission in the plasma depends on the electron density squared, Z_{eff} becomes a quantity which, when measured in this way, is highly sensitive to errors in the determination of the electron density profile. It has been noticed, and will again be pointed out at the relevant places in this thesis, that when

the line-averaged electron density in the plasma is high ($\geq 2 \times 10^{20} m^{-3}$), the inferred value of Z_{eff} can fall below 1. Clearly this is an unphysical result and has been attributed to errors in the measurement of the high electron densities. Solutions to compensate for this uncertainty, which include the use of a more robust, localized measurement of n_e using a Thomson scattering technique, are underway during the writing of this thesis.

1.4 Organization of the Thesis

This thesis is structured as follows.

Chapter 1 provides a broad introduction to some of the fundamental concepts and issues involved in tokamak research today. This introduction sets the context of and motivation for the experiments described in the remainder of the thesis. Some of the key diagnostics used to support those experiments are also described in appropriate detail in this chapter.

Chapters 2 and 3 describe some of the hardware specifically designed to conduct many of the experiments carried out as part of this thesis. Chapter 2 describes the techniques used to introduce controlled amounts of impurities into the plasma. Special emphasis is given to the laser ablation injection system which provides a unique type of impurity injection not available on all tokamaks. Also discussed are the various methods of injecting gaseous impurities into the machine. Chapter 3 describes in detail the ongoing development of an absolutely calibrated, time-resolved, high resolution VUV spectrometer which provides the majority of the data used in the analysis of impurities in Alcator C-Mod. Details of the detector system and the absolute sensitivity calibration are also given.

Chapter 4 presents the results of trace impurity transport and confinement scaling measurements made on Alcator C-Mod during the 1993 and 1994 operational campaigns. Details of the analysis methods used in determining these scalings and the implications of the results for future operation of the machine are also presented in this chapter.

Chapter 5 describes the atomic physics and transport model used for much of the quantitative analysis in this thesis. Included are a description of the numerical code package used to solve the coupled differential equations as well as the atomic rate coefficients for the relevant processes used as inputs to the code. Significant modifications to the database of these coefficients for molybdenum have been made as a direct result of some of the experiments described in this chapter. The significance of these modifications is highlighted here.

Chapter 6 presents a study of intrinsic impurity behaviour in a variety of different operating regimes. These include plasmas which can be categorized as ohmic, high power RF, limited, diverted and detached, L-mode, and H-mode. Many of the important impurity related questions outlined earlier are answered by the experiments described in this chapter.

Chapter 7 describes measurements made of the efficiency with which the plasma is able to screen out an external source of injected impurities. A number of different impurities was injected using the available techniques to provide an extensive database.

Chapter 8 reports on an analysis technique making use of charge exchange reactions with injected impurities which was used to infer a neutral particle density profile in Alcator C-Mod. This chapter is included to highlight the diagnostic usefulness of these impurity injections beyond the obvious. Further applications and extensions of this analysis technique are also discussed.

The appendices provide more details of the atomic physics rate coefficients and calculations used in much of the analysis. Detailed tables and functional fits of new rates for molybdenum, in particular, are also provided.

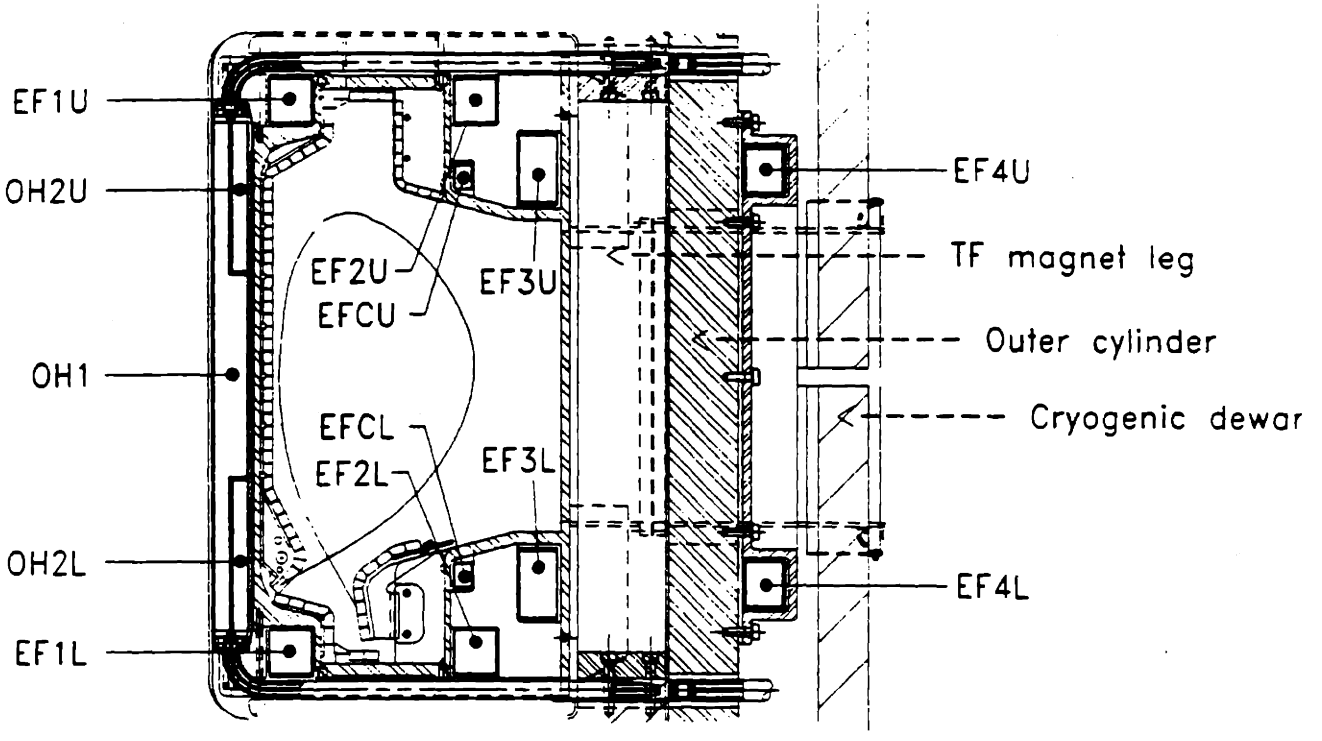

Figure 1-1: The set of poloidal field coils used on the Alcator C-Mod tokamak. Also shown are details of the highly shaped divertor and inner wall areas which are surfaced with molybdenum plasma facing components. The magnetic geometry of a typical highly shaped plasma as calculated by the EFIT code is also shown.

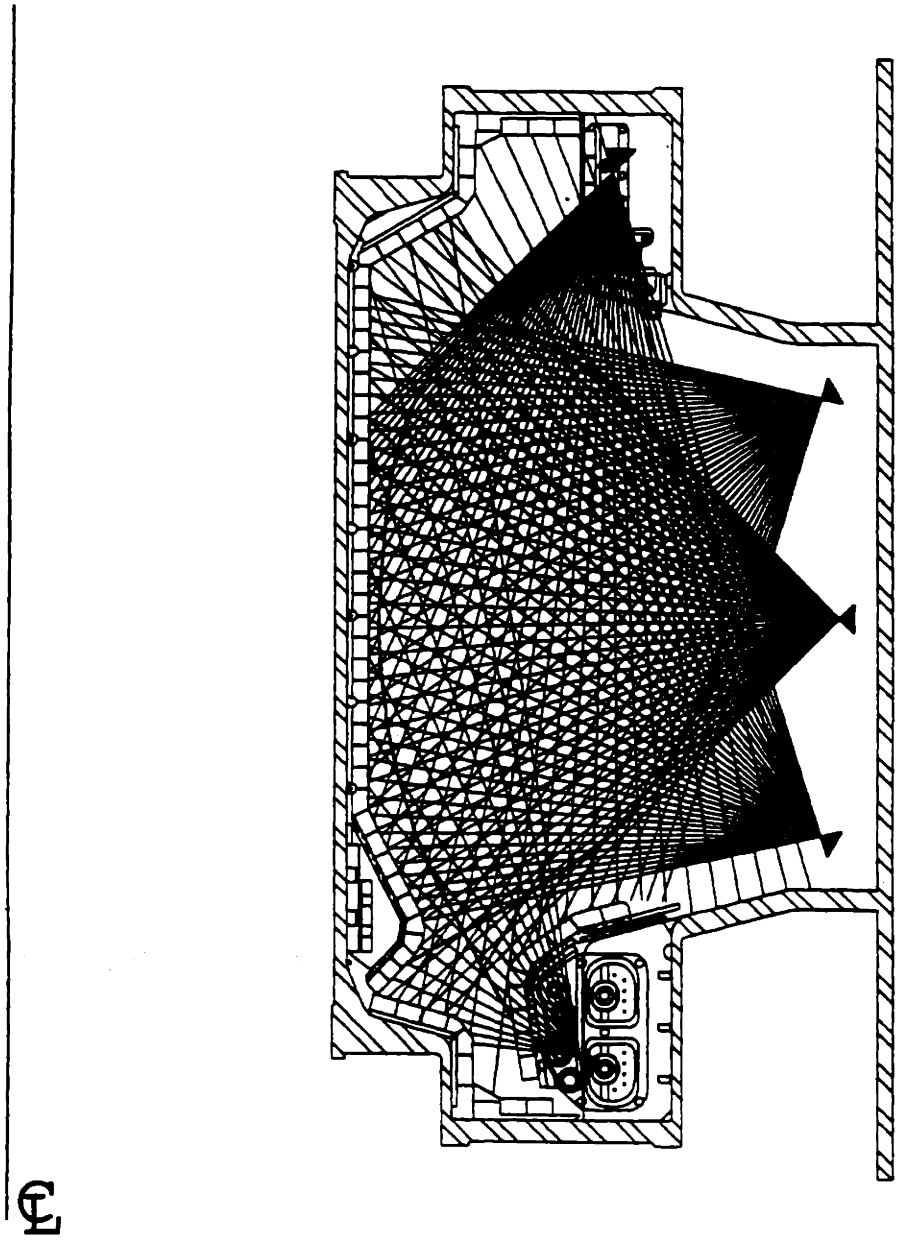

Figure 1-2: X-ray diode arrays on Alcator C-Mod.

Chapter 2

Laser Ablation Impurity Injection

2.1 Introduction

A proper investigation of impurity transport in tokamak plasmas requires the ability to control the impurity source with some precision. Investigations based solely on intrinsic plasma impurities suffer from the ambiguity inherent in an impurity source which may be varying in time and space. There is a number of techniques available which allow for well defined injections of various impurity species. Each method is best suited to a particular type of experiment. When quantities of gaseous impurities are desired, simple calibrated gas puff injections are usually sufficient. These gas injections can be of trace amounts of impurity or of amounts large enough to have macroscopic effects on the plasma. Gas injections generally involve recycling impurities (that is, ones which are not easily adsorbed to the walls of the machine), although certain low recycling gaseous impurities are also available. This method can inject impurity neutrals with only relatively low energy [12]. For experiments which require impurities to be deposited as neutrals deep within the plasma, pellet injection techniques which can fire macroscopic amounts of impurity at velocities of up to 1 km/s [13] are available. These injections, however, are invariably highly perturbing to the background plasma. Injections which can still be considered trace, but which provide impurity neutrals with some finite energy,

can be achieved using the so-called laser ablation technique [14]. This method uses a high power laser pulse incident on a target material to create a population of energetic neutral atoms with a directed velocity toward the plasma.

2.2 The Laser Ablation Injection System

2.2.1 Hardware

The design of the Alcator C-Mod laser ablation injection system meets a number of operational requirements and constraints. Many of these constraints are related to space limitations at the diagnostic ports of the machine. Due to the geometry of the vertical diagnostic ports, no practical access from either above or below the plasma is available. This means that any laser ablation injections are introduced through a horizontal port. Similarly, access to the plasma midplane is limited. The ultimate location for the injection system was chosen to be at a horizontal port about 20 cm above the midplane. Also as a result of space restraints, the laser ablation targets are placed no nearer than about 1 meter from the plasma.

Each target is a two inch square standard glass slide with a vacuum deposited layer of the desired impurity material on the plasma facing side. The thickness of the deposited layer is typically 1 μm, but layers from 0.5-5 μm thick were also used in initial tests. For increased versatility, the injector is designed to accommodate up to nine different target slides at any given time. Slides are arranged in rows of three on three faces of a hexagonal carousel and can be selected and positioned remotely on a between-shot basis by a combination of rotation and linear motion of the carousel and linear motion of the laser beam. The carousel is housed in an independent vacuum chamber with a volume of about 40 liters which is pumped by a 60 ℓ/s turbo pump. A rotary/linear multi-motion feedthrough with an 8 inch stroke is used for control of the carousel position. The ultimate base pressure in the injector chamber when fully loaded with slides is 1×10^{-8} Torr. A schematic of the injector chamber is shown in Figure 2-1.

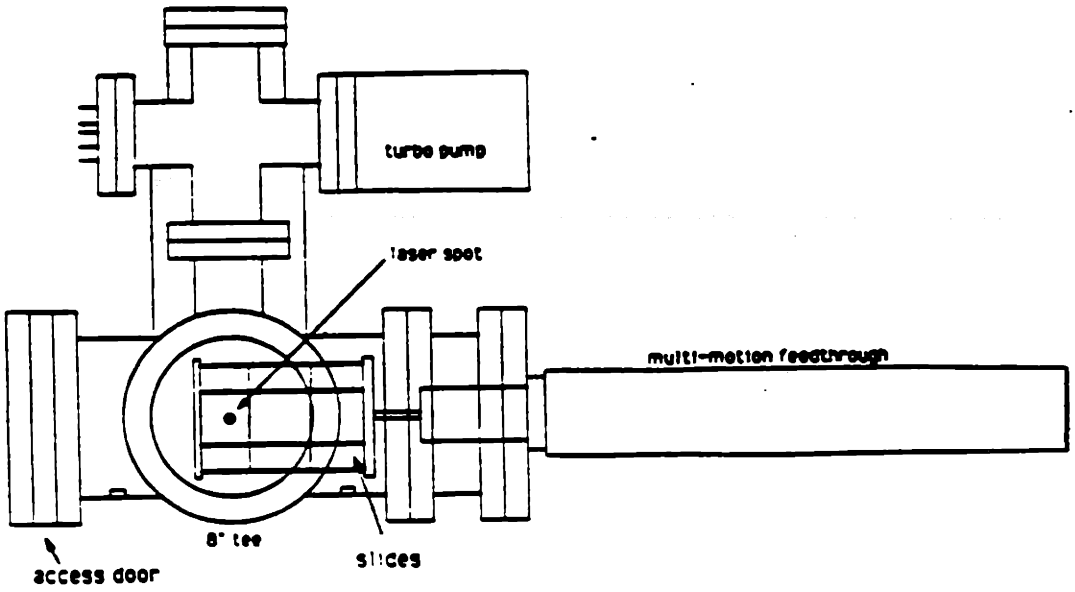

Figure 2-1: Schematic of the laser ablation impurity injector system as viewed from behind (ie. looking toward the plasma).

The laser beam used for the ablation is incident normal to the target slide through an 8 inch diameter glass vacuum window. Its source is a Q-switched ruby laser operated at 694 nm with a single $\frac{1}{2}$ inch diameter oscillator rod which can generate a 30 ns pulse of up to 3 Joules. A HeNe alignment laser, collinear with the ruby laser, is used for visual monitoring of the beam position. The alignment is sufficiently free of drift that active position feedback is not required. Good alignment (within 10% of the target spot size) could be maintained indefinitely. The lasers themselves are housed in a diagnostic lab outside of the C-Mod cell, about 10 meters away from the target slides. The beams pass through a penetration hole in the thick concrete neutron shield wall which encloses the cell and then strike a remotely controlled 4 inch diameter mirror located about 1 meter above the targets. The beams are then directed down to a 2 inch mirror located about 50 cm from the targets. This mirror can be moved remotely in the vertical direction to

allow for spot selection on the target slide. The final leg of the beam path is through a 2 inch diameter lens with a 20 cm focal length. The lens is placed about 10 cm in front of the vacuum window to the injector chamber with its focal point about 5 cm in front of the target so that the beam is expanding at the time it actually strikes the slide. This is done to avoid any tightly focussed reflections from the target or the window on the 2 inch mirror or the window itself. Tests had indicated that a tightly focussed beam from the laser was capable of damaging the ordinary glass vacuum window. The judicious selection and placement of the lens therefore eliminated the need for either a quartz window or an anti-reflection coating on a standard window.

A photodiode filtered for the laser wavelength is used to measure the energy of each pulse. During normal operation, a glass slide is used to reflect about 4% of the beam energy onto the photodiode which was calibrated with a calorimetric energy monitor. The response time of the diode is not fast enough to follow the actual 30 ns laser pulse, but a reproducible signal is nonetheless obtained on a microsecond timescale with the appropriate selection of amplifier time constants. A typical diode signal from a 2 Joule laser pulse digitized at 1 MHz is shown in Figure 2-2. The flash lamp trigger in this case was at 550.0 ms and the actual Q-switching occurred at 550.625 ms. The large spike at that time is noise pick-up from the 12 kV charge being switched on the Pockell's cell during the Q-switching. The total area under the diode signal curve is assumed to be proportional to the total energy in the pulse. The calibration curve which relates that area, in units of Volt-microseconds, to the pulse energy in Joules is shown in Figure 2-3. The calibration was found to be highly linear over the range of expected operating energies.

2.2.2 Reproducibility of Injections

A series of molybdenum injections was made into a number of identical discharges as part of an experiment to measure spatial profiles of molybdenum emission (see Chapter 4). This series of injections also served the purpose of measuring the reproducibility of the

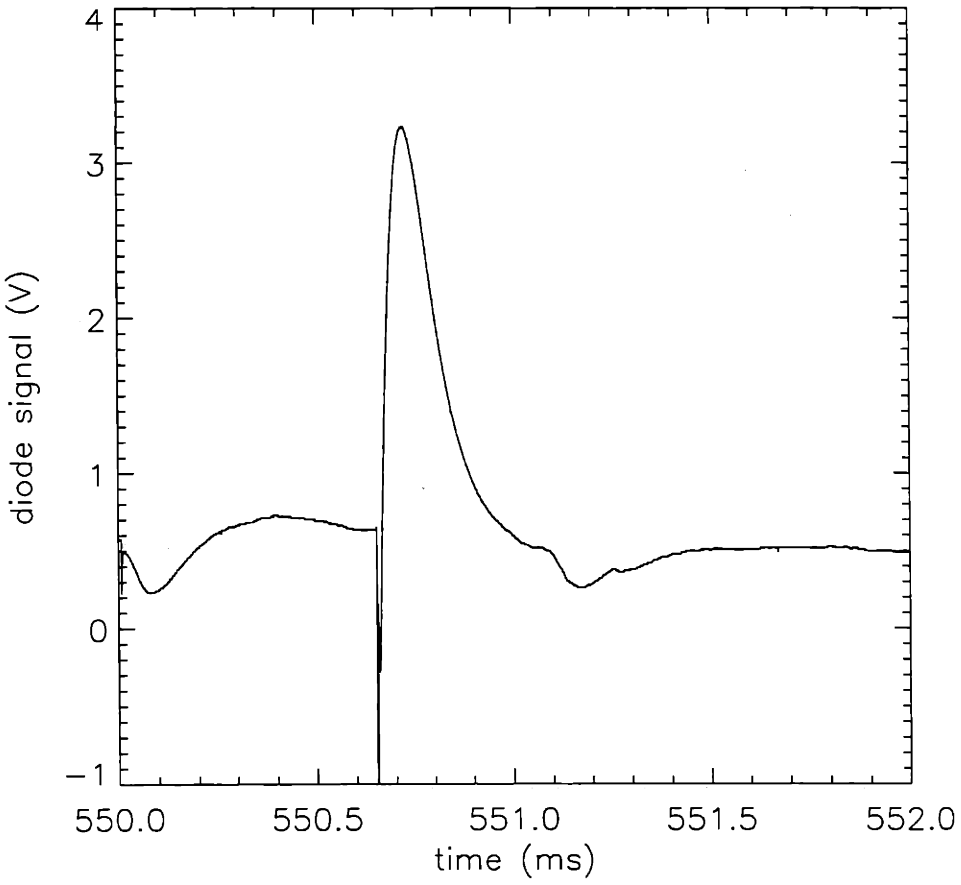

Figure 2-2: Diode signal from a 2 Joule laser pulse. The net area under the signal is 355 Vμs.

injection system. This reproducibility could be monitored in a number of ways. First, a visual examination of the ablated spots on the target slides was used as a qualitative evaluation of the injections. The beam size at the target was chosen to give a spot size of about 4 mm. This visual examination found the spots to be highly reproducible, with no obvious changes from one spot to the next. A more quantitative comparison could be had by comparing the relative strength of signals measured on the multi-layer mirror polychromator (see Chapter 3) when observing high charge states of molybdenum at the centre of the plasma. Since the discharges all had similar plasma parameters, the brightness measured in this way should be highly indicative of the reproducibility of the

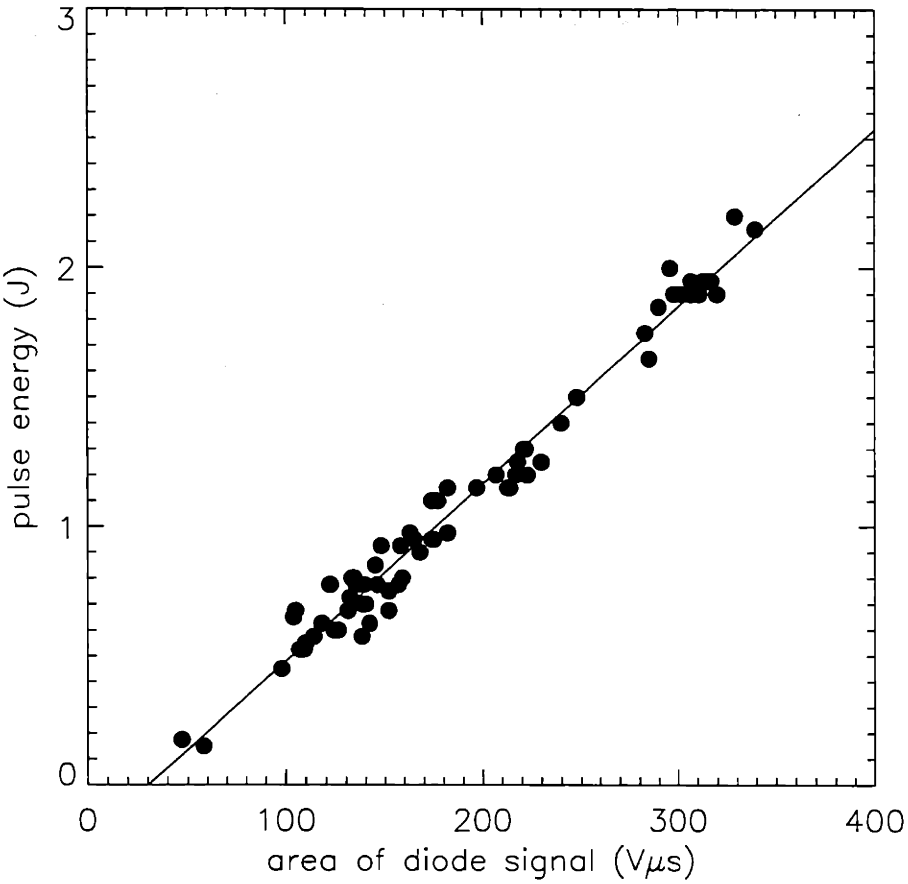

Figure 2-3: Calibration curve for laser energy monitor.

source injection. The brightnesses measured over this series of discharges are shown in Figure 2-4. The variation in the brightnesses is less than about 30% of the nominal value. Given that the variation of the discharge parameters (especially electron density) was also about 30% for these discharges it can be concluded that the laser ablation injections are reproducible to at least within that tolerance.

The energy of the ablated atoms is also a quantity of interest for use in interpreting the observed effects of an injection made with this technique. If the energy density of the laser beam at the slide is sufficiently high, the ablated particles may be ions and thus be swept to the walls of the beamline by the magnetic fields which exist at the target position. The fields at the target location are estimated to be a few hundred Gauss

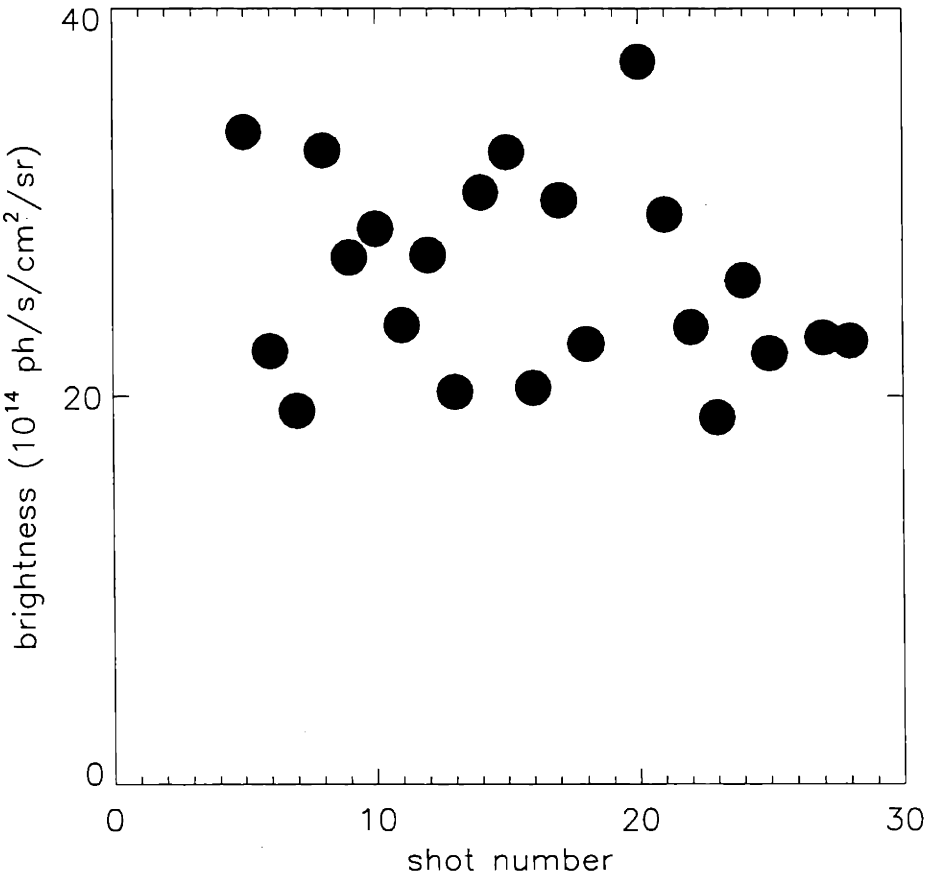

Figure 2-4: Observed brightnesses of a series of laser ablation injections of molybdenum into identical discharges.

during each discharge. This is sufficient to produce an ion gyroradius of a few to several tens of millimeters depending on the mass and charge of the ions. This is generally not a desirable result, since it would mean that very few of the ablated particles would reach the end of the beamline and actually be incident on the edge of the plasma. Although some ions will inevitably exist as a result of the ablation process, a more appropriate injection would be one in which the particle energy was low enough that most of the ablated particles are neutrals. Several investigations of this issue have been done previously [15] and have produced various relationships between laser fluence and mean particle energy. It is generally thought that the cloud of neutral atoms has a thermal distribution of

energies superposed on a directed energy of somewhere between 1 and 10 eV.

2.3 Other Injection Techniques – Gas Puff Injection

On Alcator C-Mod there exists a number of methods of injecting gaseous quantities of impurities at various locations around the plasma. Two main systems for performing these injections include the divertor gas injection system and the main gas fuelling system. The divertor gas injection system is capable of introducing calibrated amounts of impurity or fuel gas at up to 28 specified poloidal locations around the plasma. The gas is introduced through long capillary tubes (~3 m long, 1 mm diameter) which are fixed behind the molybdenum plasma facing tiles. The flow of gas is controlled by independent fast solenoid valves connected to the output of a holding plenum with a volume of about one liter. By specifying the pressure in this holding plenum and the duty cycle of the valve, the flow rate of gas into the machine can be controlled over the range from about 0.1 torr-l/s to several hundred torr-l/s. For trace impurity injections, it is only flow rates at the lowest end of this range which are useful. Due to the long length of capillary tubing which is required to deliver the gas at the specified location, the time response of this injection system is relatively slow ($\sim$ 200 ms).

The other system capable of providing calibrated gaseous impurity injections is the main gas fuelling system. This system uses piezo-electric valves to control the flow of gas from a four liter holding plenum to the plasma. These piezo-electric valves are located at five positions around the vacuum vessel, all at locations somewhat remote from the plasma (at least 15 cm away from the separatrix). The advantage of this system is that it provides a much faster time response than do the capillary tubes, owing to the large differences in conductance to the plasma. The drawback is that there does not exist the same spatial flexibility with regard to the injection location.

Shown in Figure 2-5 are the locations of each of these gas injection systems along with a schematic which shows where the ablated cloud of neutrals from the ablation

injection system is incident on the plasma. The flexibility of these injection systems will be discussed and their usefulness demonstrated in the chapters that follow.

Figure 2-5: Poloidal locations of the divertor gas injection system. Also shown is the region of the plasma where laser ablation injections are incident.

Chapter 3

A Time-Resolving, High Resolution VUV Spectrometer

3.1 Introduction

At typical operating temperatures in Alcator C-Mod, much of the line emission from impurities in the plasma occurs in the VUV region of the spectrum. It is therefore important to have spectroscopic diagnostics capable of monitoring and quantifying this emission. To this end, a number of different spectroscopic diagnostics have been installed on the machine. This chapter will describe in detail the design, calibration, and operation of a high resolution, time-resolving, absolutely calibrated, grazing incidence spectrometer which has been used to monitor the wavelength region from about 50 Å to 1100 Å. This device, referred to as the McPherson spectrometer after the company supplying the basic instrument, is used as the baseline diagnostic for the characterization of impurities in the tokamak.

The McPherson instrument originally was operated as a monochromator with a fixed entrance slit and a movable exit slit in a Rowland circle configuration. A single channel detector was placed at the exit slit, along the 2.2 meter diameter circle, and provided high time resolution measurements of a given narrow band of the spectrum. The wavelength,

λ, in order n, which is focussed along the Rowland circle is determined by the standard grating equation:

$$n\lambda = d(sin\alpha - sin\beta) \tag{3.1}$$

where α and β are the angles of incidence to and diffraction from the normal of a grating with line spacing d.

To increase the flexibility of this device, it has been upgraded to a time-resolving spectrograph with finite bandwidth through the use of a microchannel plate image intensifier and a Reticon [16] photodiode array detector. For use on Alcator C-Mod, this detector was re-designed to provide improved spectral resolution and reliability of operation. The new system was characterized using the old system as a bench-mark. Quantities such as instrumental broadening and uniformity of response across the grating and across the detector, and absolute system sensitivity all as functions of wavelength were measured and compared to the previous system. Schematically, the microchannel plate-based image intensifier and detector, taken from reference [3], are shown in Figure 3-1.

3.2 System Operational Characteristics

This VUV spectrometer system now allows for a great deal of operational flexibility. Custom designed electronics allow for different integration times to be used during different phases of the discharge. Up to four different integration states can be selected with a variable number of frames in each state. The selected integration times can be as short as 0.5 milliseconds if a reduced bandwidth is observed, or as long as 4096 milliseconds if very weak sources are being observed during calibration. This feature of multiple integration states is exploited during laser ablation injection experiments, for example, when it is known that a fast integration time is desired over only the duration of the injection. Typically integration times of 2 ms for a duration of about 100 ms are used during such laser ablation injections. This flexibility also proves useful for separating the start-up phase of the discharge, when most emission is very bright, from the current

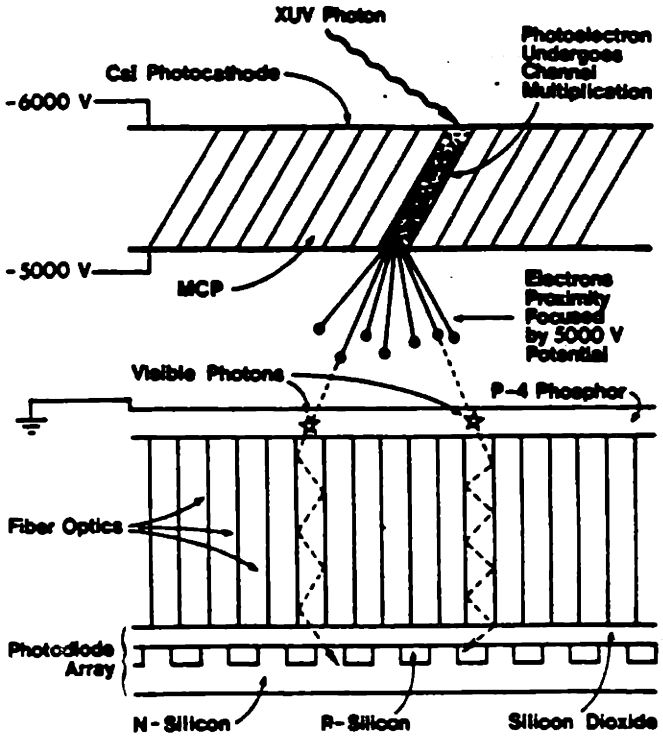

Figure 3-1: Schematic representation of the microchannel plate image intensifier and detector. Also shown are typical operating voltages of the various components.

flat-top phase of the discharge, when many line intensities drop by as much as an order of magnitude (see Chapter 6). In such cases, integration times as short as 4 ms are used during start-up while longer integration times are used during flat-top. This helps to make use of the maximum dynamic range available at fixed gain on the detector system.

The wavelength range being viewed can also be changed between shots anywhere within the effective limits of about 50-1100 Å. A standard stepper motor is used to move the entire detector assembly along the Rowland circle for this wavelength selection. The entire assembly can be positioned to within about 0.0005" with a reproducibility that keeps known spectral lines centered to better than about 0.05 Å.

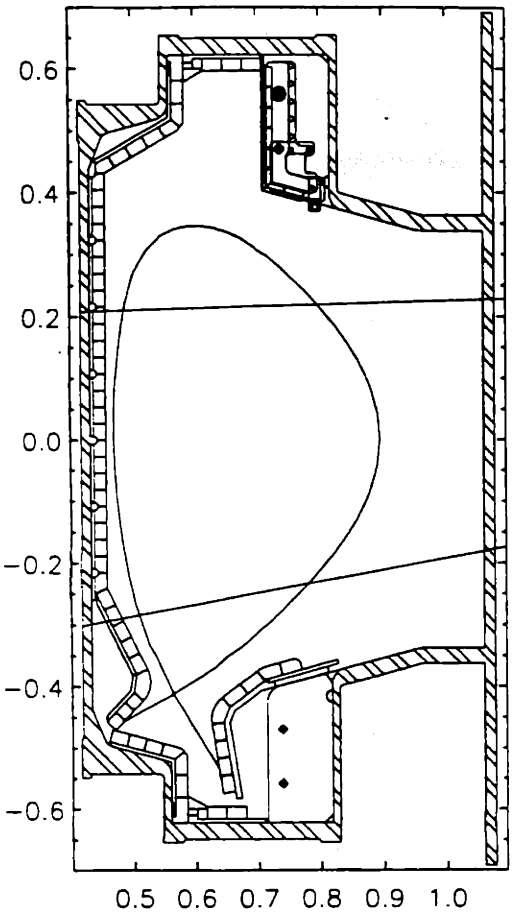

Figure 3-2: Range of viewing chords available to the VUV spectrometer. The spatial resolution at the magnetic axis is about 1.0 cm in the poloidal dimension and about 15 cm in the toroidal dimension.

The most common chord viewed by this spectrometer is typically one through the center of the plasma. The spectrometer has the capability, however, of viewing chords well above and below the plasma center. The grating itself is located about 3 meters away from the plasma radially and about 30 cm above the magnetic axis. Selection of a particular chordal view is obtained by pivoting the entire rigid grating/detector assembly about an axis through the entrance slit. The entire assembly weighs about 500 kilograms and is pivoted using an industrial screw jack. This technique allows for reproducible positioning of the instrument to within about 3 mm at the jack which corresponds to

about 1 cm at the plasma. The complete range of chordal views available is shown in Figure 3-2 where it is superposed on a typical diverted plasma equilibrium. This positioning feature is demonstrated extensively during the investigation of the spatial profiles of various molybdenum lines and is outlined in Chapter 4.

3.3 System Calibration

A number of different calibrations was performed on the new spectrometer system. The instrumental broadening was measured at various points across the detector in order to optimize the spectral resolution. The uniformity of response across the face of the detector was also measured to evaluate the effectiveness of the new repeller plate. A wavelength calibration was made and compared with geometric calculations. An absolute sensitivity calibration was also performed in different orders over some of the wavelength range of the instrument. The results of each of these procedures are outlined in the sections that follow.

3.3.1 Instrumental Broadening

It was hoped that the design of the new detector would allow for improved spectral resolution by reducing the lateral spread of photons as they travel along the coherent fiber bundle. To verify this reduction, measurements of the width of a zeroth order line were made. The source used for these measurements was a commercially available platinum lamp operated at about 250 volts and about 10 milliamps. This proved to be a relatively weak source, so long integration times (up to 4096 ms) were used to collect enough signal. The source was set at an grazing angle of incidence of about 82.5 degrees and the detector was set to observe specular reflections from the grating (i.e. the zeroth order line). A typical line observed in this way is shown in Figure 3-3 where the detector was positioned so as to place the line near the center of the diode array. Also shown in that figure is a Gaussian fit (dashed line) with FWHM of 7.5 pixels. The Gaussian fit

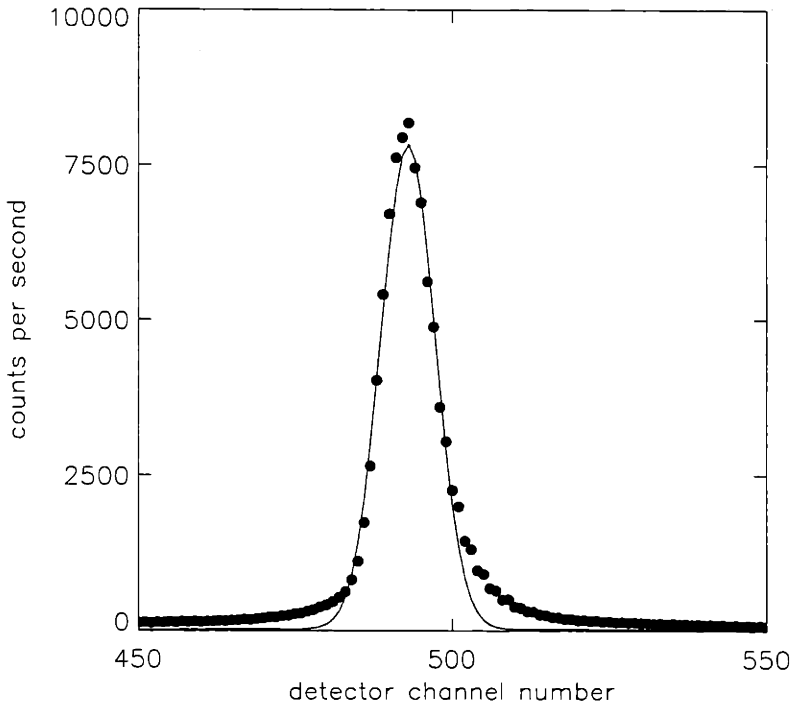

Figure 3-3: A zeroth order line from a platinum lamp source captured near the center of the detector. Also shown is a Gaussian fit to this line.

to this lineshape is good except at the wings of the line, where it underestimated the strength of the signal. This line shape shows a large improvement over that obtained using the old detector. In that case, a much larger fraction of the total number of counts under the peak were contained near the wings of the line.

Since the Rowland circle geometry truly focusses in the dispersion plane along the Rowland circle, and since the microchannel plate detector is flat, the entire detector cannot be in ideal focus at all times. As a way of measuring this effect, and of optimizing the alignment of the detector, the zeroth order platinum lamp line was scanned across the microchannel plate detector channels to measure the instrumental line broadening as a function of the position on the plate. This scan was also done using an incident angle of 82.5°. The result of this scan is shown in Figure 3-4 where the FWHM of the observed zeroth order platinum lamp line is plotted as a function of position on the microchannel

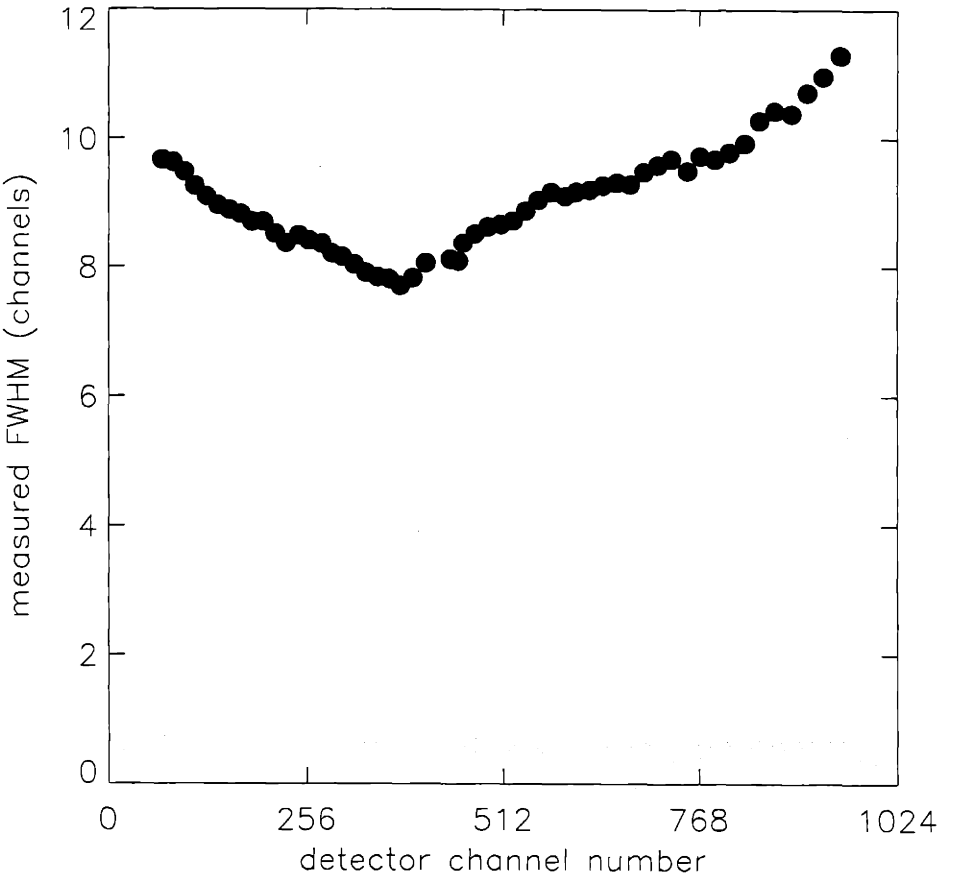

Figure 3-4: FWHM of the zeroth order platinum lamp line as a function of position on the detector for an angle of incidence of 82.5°.

plate. The position (in units of detector channel number) shown is the position of the center of the platinum lamp line on the detector. Low channel number corresponds to the short wavelength side of the detector, closest to the grating. The results shown represent the optimal alignment of the detector which was arrived at after numerous iterations. The criteria used to determine the best possible alignment included both the minimization of the broadening at the point along the detector closest to the ideal focus as well as the avoidance of a large variation in broadening across the entire length of the detector.

3.4 Detector Gain

3.4.1 High Voltage Calibration

In order to have a reliable absolute calibration of the device, the gain characteristics of the system as a whole were determined over the entire range of operating parameters. In particular, the detector can be operated with variable voltages across the micro-channel plate, across the phosphor, and across the repeller grid (see Figure 3-1). Experiments were therefore conducted to measure the gain of the detector assembly over the full range of these operating voltages. Using the platinum lamp in zeroth order at a fixed position (nominally centered) on the detector, the voltages on both the input and output faces of the micro-channel plate and on the repeller grid were systematically varied to map out the gain characteristics. A typical signal obtained is similar to that shown in Figure 3-3. The total number of counts measured under the peak of that line after subtraction of a background pedestal level was considered indicative of the strength of the signal received.

With the repeller held at a fixed value of -2300 V relative to the input side of the plate and with the voltage across the plate held at 750 V (output side relative to the input side), the accelerating voltage between the phosphor and the output side of the plate was varied over the range 3000 to 5000 V. In each case, the total number of counts under the peak was measured after integration for times ranging from 256 ms to 4096 ms. The number of counts per second measured in this way as a function of the phosphor voltage (normalized to the number measured at a phosphor voltage of 4900 V) is shown in Figure 3-5. A best fit polynomial function is also shown in that figure. The best fit for the normalized gain due to the phosphor voltage, G_{ph}, was determined to be:

$$G_{ph} = 5.43 \times 10^{-5}(V_{ph} - 3000) + 2.48 \times 10^{-7}(V_{ph} - 3000)^2 \qquad (3.2)$$

In a similar manner, the relative gain due to the plate voltage was measured at fixed repeller voltage (-2300 V) and fixed phosphor voltage (4500 V). Those results are summarized in Figure 3-6 and are shown along with a best fit polynomial to the plate

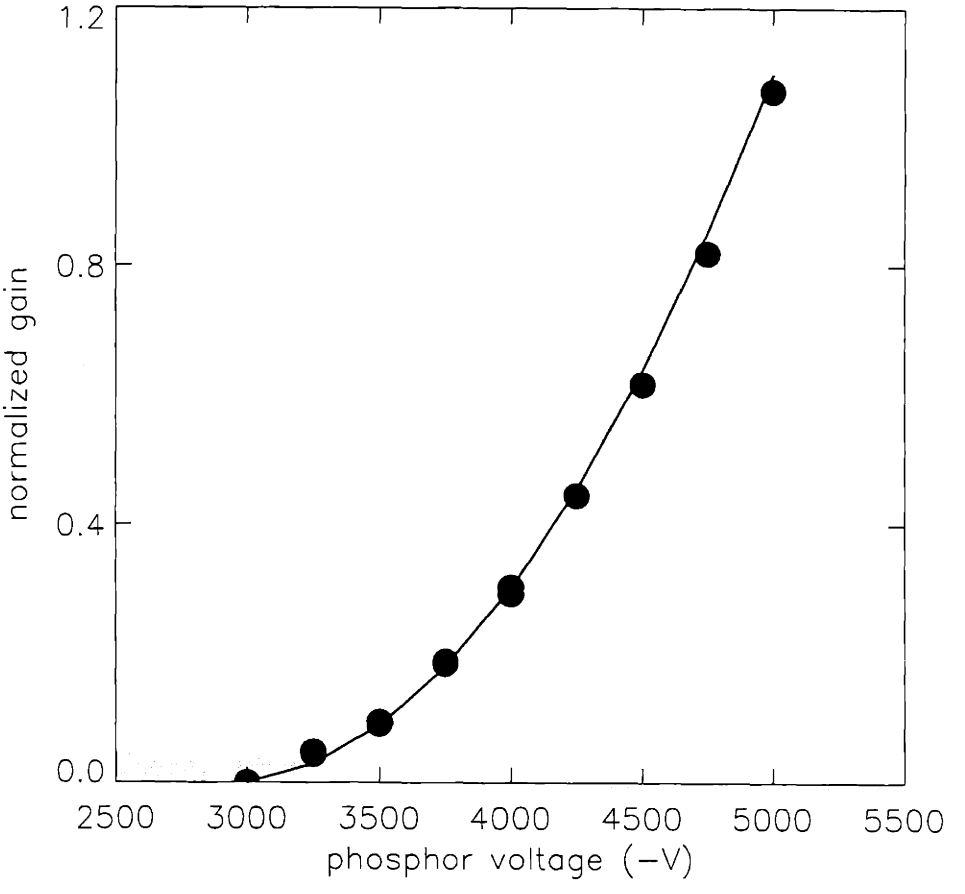

Figure 3-5: Total counts per second under the zeroth order platinum lamp line as a function of phosphor voltage with fixed plate voltage (850 V) and repeller voltage (-2300 V) normalized to a phosphor voltage of 4900 V.

gain, G_{pl}, as:

$$G_{pl} = -24.4 + 0.105V_{pl} - 1.49 \times 10^{-4}V_{pl}^2 + 7.05 \times 10^{-8}V_{pl}^3 \tag{3.3}$$

Knowing these two functions, G_{ph} and G_{pl}, the relative strength of a signal obtained at any voltage setting within the ranges of validity of the fits can be referred back to the original voltages used in the absolute calibration discussed in the following sections. This effectively extends the absolute calibration to virtually the entire practical operating range of voltages.

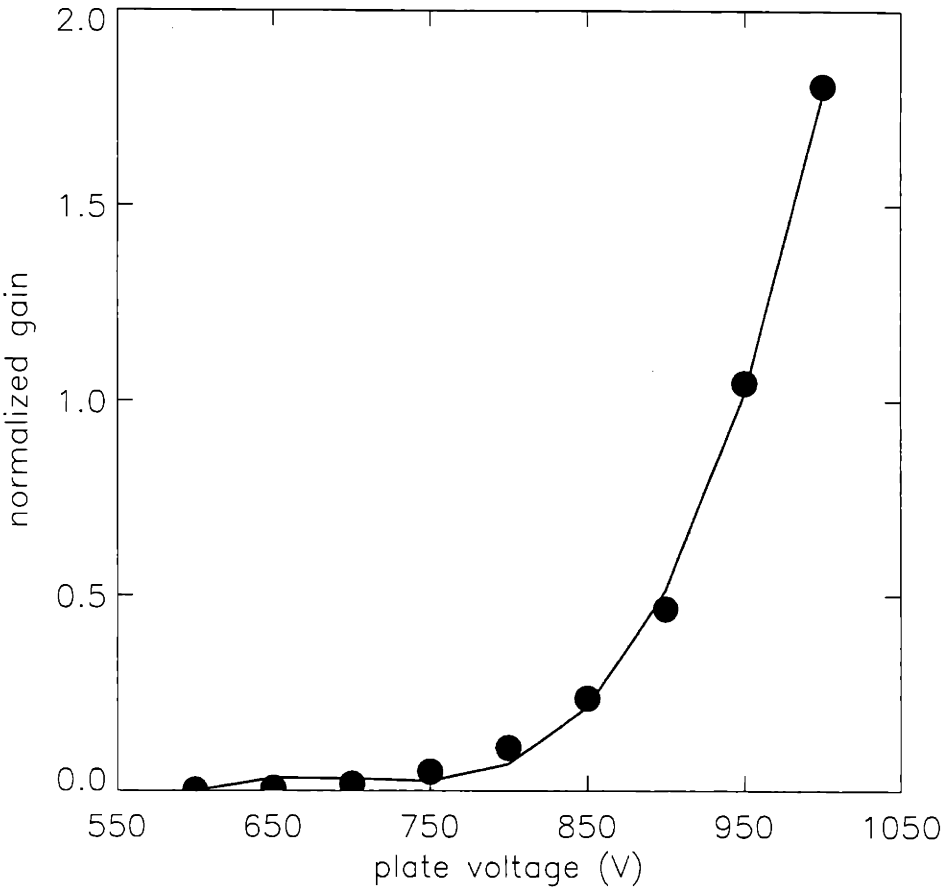

Figure 3-6: Total counts per second under the zeroth order platinum lamp line as a function of plate voltage with fixed phosphor voltage (4500 V) and repeller voltage (-2300 V) normalized to a plate voltage of 950 V.

3.4.2 Slit Width

The detector response to changes in slit width was also investigated. Although a linear response was expected, it was important from the point of view of ensuring the robustness of the absolute calibration at different detector settings to verify this relationship. Shown in Figures 3-7 and 3-8 are the total counts per second measured at different slit width settings for both large and small values of slit width. Each of these calibrations was obtained with a different source. This accounts for the differences in the count rate detected in each case. The large slit width data in Figure 3-7 were obtained using the

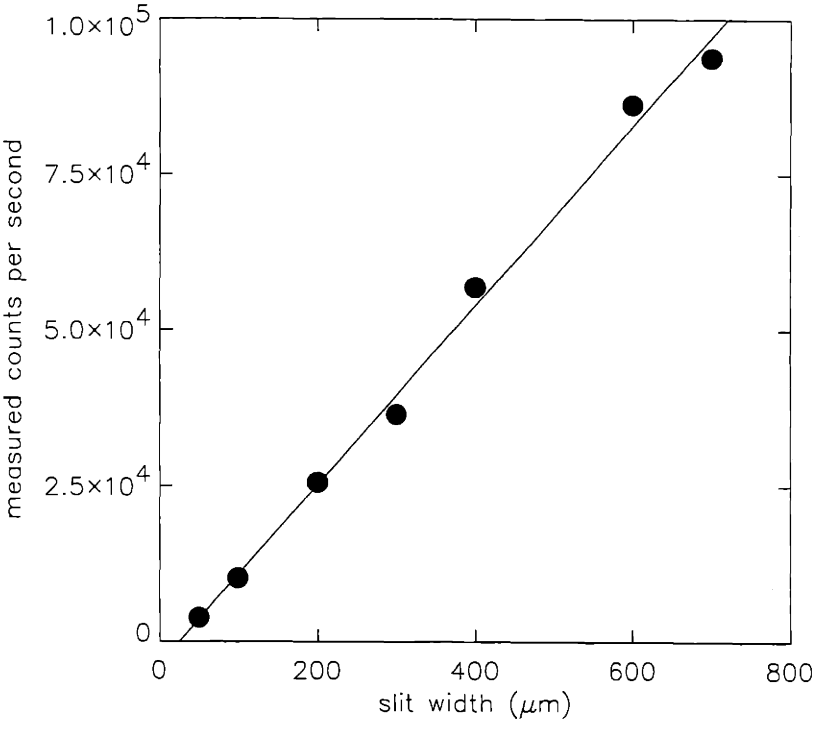

Figure 3-7: Total count rates at fixed detector gain as a function of entrance slit width for large slit widths.

carbon line generated by the Manson soft x-ray source discussed in the following section. The small slit width data in Figure 3-8 were obtained using the same platinum lamp line used earlier. Note first that there can be extrapolated from these plots (particularly Figure 3-8) an offset in the 'nominal' slit width as read on the entrance slit micrometer itself. This offset has been determined to be 23 μm and is consistent with data taken in both ranges of slit width. Also apparent from the plot is that the linearity of the signal with slit width is very good. This allows for confident use of calibration measurements made for large slit widths at the small slit widths typical when viewing the much brighter tokamak discharges.

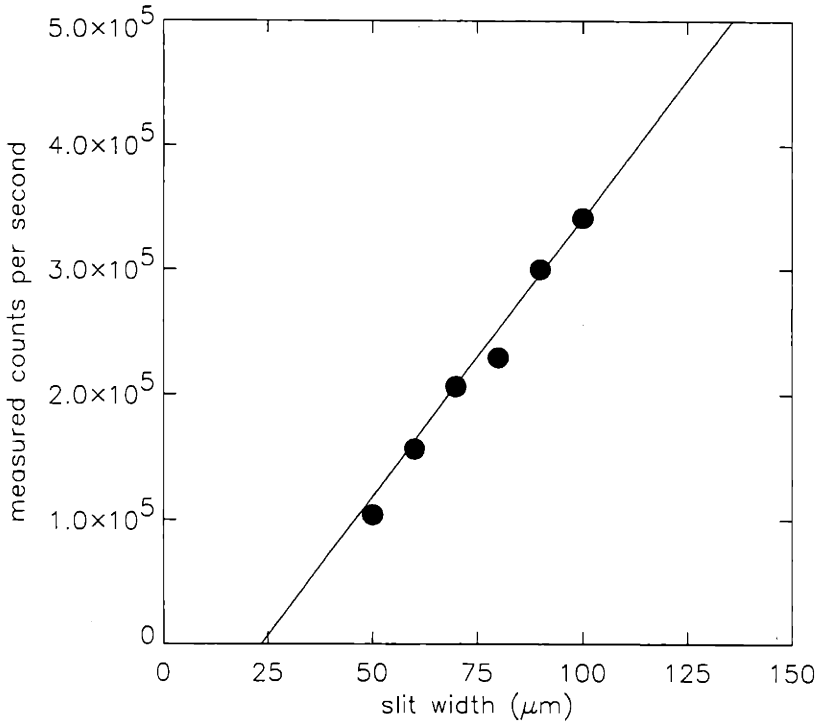

Figure 3-8: Total count rates at fixed detector gain as a function of entrance slit width for small slit widths.

3.5 Absolute Calibration

3.5.1 Short Wavelength Calibration

A soft x-ray source was used to calibrate absolutely the VUV spectrometer up to 114 Å. This source, known as a Manson source [17], utilizes an electron beam incident on an anode in order to produce x-rays (mostly K-shell) from the desired anode material. By selecting appropriate anodes, a range of well-defined soft x-ray and XUV lines from about 10 Å to 114 Å can be obtained. The x-ray calibration apparatus which uses the Manson source also allows for a gas-filled proportional counter to be inserted into the x-ray beamline at any time. With the beam targeted at the spectrometer grating, this capability allows for an absolute calibration of the entire spectrometer system. Table 3.1 summarizes the anode materials and the resulting lines which were used for this absolute

anode material	K-shell emission from	wavelength (Å)
$Mg(OH)_2$ solution	Mg	9.89
$Mg(OH)_2$ solution	O	23.6
AlN powder	N	31.6
graphite	C	44.7
B powder	B	67.0
BeO powder	Be	114.0

Table 3.1: Anode materials and lines from the Manson source used in the absolute calibration of the VUV spectrometer.

sensitivity calibration.

Each anode was placed into the source chamber in turn and exposed to the energetic focussed electron beam. Typical beam voltages were 3-5 kV at currents of 100-500 μamps. The spot size of the electron beam on the anode target was about 2 mm in diameter. The beamline between the face of the anode and the entrance slit of the spectrometer was on a movable two-dimensional pivot which allowed the source to be scanned both parallel and perpendicular to the lines of the grating. This feature was used to investigate the spatial uniformity of the grating. For absolute calibration purposes, however, a large entrance slit was used to both maximize the strength of the signal obtained and to illuminate the as much of the grating as possible to integrate over any non-uniformities which might be present. With the chosen source line positioned to strike the center of the detector at a grazing incidence angle of 88°, the total number of counts collected under the peak of the line was measured for a number of integration periods at fixed detector gain characteristics. Having obtained a sufficiently strong signal at the detector, the gas filled proportional counter was lowered into the beamline so as to collect the flux which was previously incident on the grating. The output from the proportional counter is routed through a multi-channel analyzer to yield an energy spectrum of collected photons where the photons due to the given line to be calibrated are well resolved from any secondary lines which may be present in the emission. Because the efficiency of the proportional counter is close to 100% for these photons, it gives the absolute flux of photons which were emitted by the source. Using the beamline geometry, this source flux can be converted to

a flux of photons incident on the grating. It is this flux which is incident on the grating which allows for a measurement of the absolute sensitivity. The system sensitivity as a function of wavelength at a given set of detector voltages is given by:

$$s(\lambda) = \frac{\text{number of counts at detector}}{\text{number of photons incident on grating}} \tag{3.4}$$

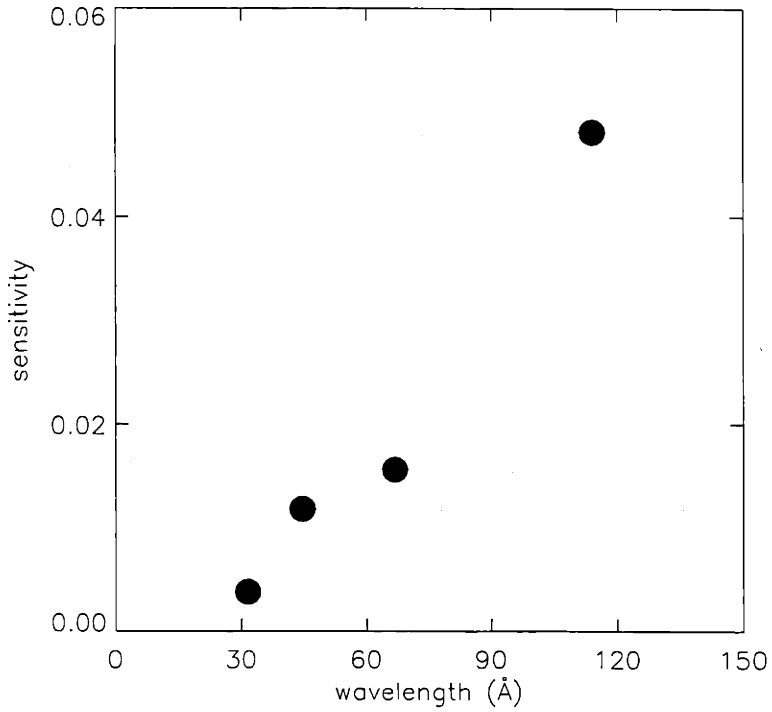

Figure 3-9: Measured first order sensitivity as a function of wavelength using the Manson source.

Listed in Table 3.2 are the measured sensitivities at different wavelengths in first order. These values for the system sensitivity, $s(\lambda)$, are also shown graphically in Figure 3-9. This procedure was also carried out for various lines in second order and also in third order where possible. The sensitivities obtained from those calibrations are shown in Figures 3-10 and 3-11. Note the general trend seen in all of these sensitivity curves of a generally increasing sensitivity as wavelengths approach 120 Å. This feature is expected from a consideration of the response characteristics of the CsI photocathode layer which

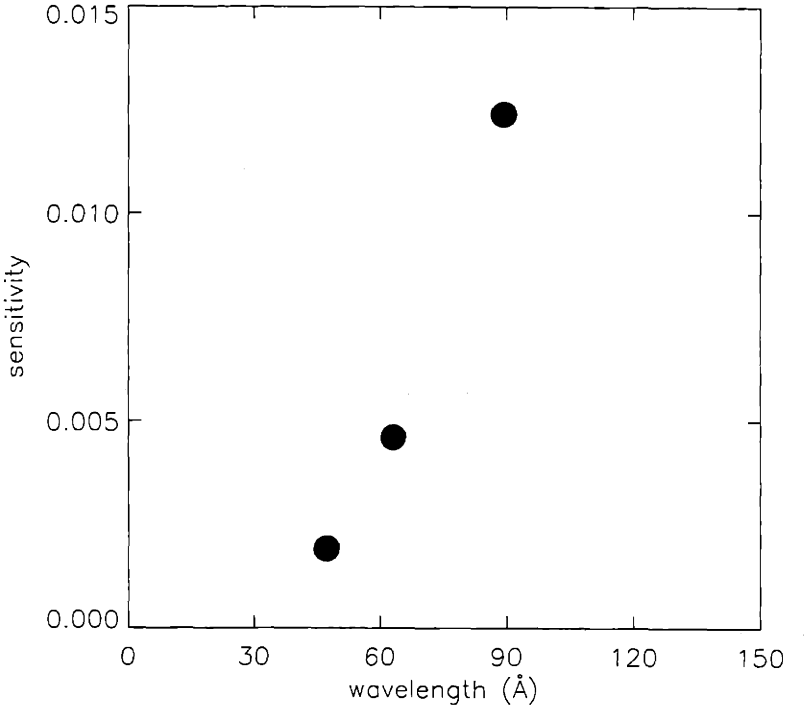

Figure 3-10: Measured second order sensitivity as a function of wavelength using the Manson source.

coats the input side of the microchannel plate image intensifier. This photocathode material has a peak in its responsiveness at about 120 Å [18]. The absolute sensitivity calibration carried out in this region of the spectrum with the Manson source is therefore consistent with this material feature. An extension of this calibration to even higher wavelengths is discussed in the following section.

anode	wavelength	first order sensitivity ($\times 10^{-2}$)
O	31.6	0.38
C	44.7	1.18
B	67.0	1.56
Be	114.0	4.82

Table 3.2: Measured absolute sensitivities in first order.

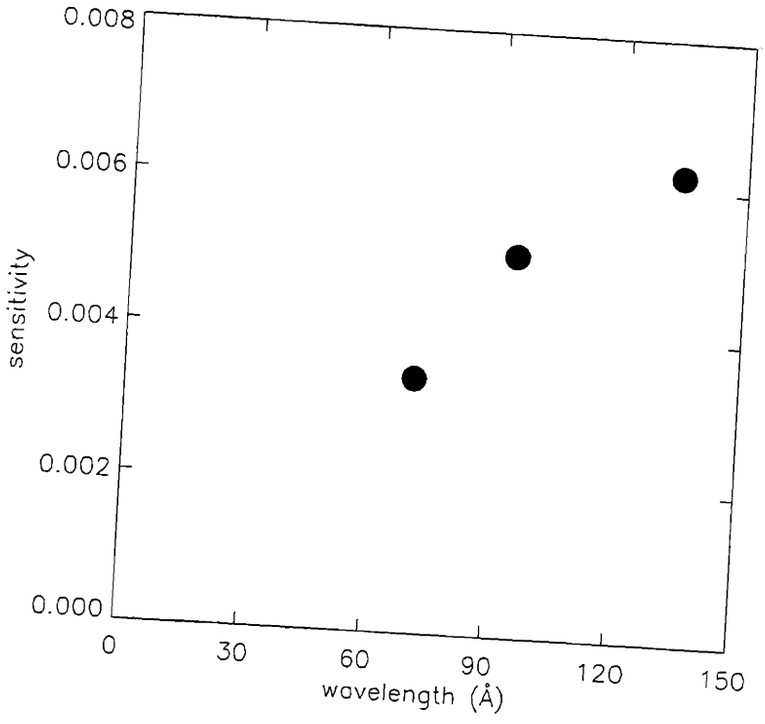

Figure 3-11: Measured third order sensitivity as a function of wavelength using the Manson source.

3.5.2 Long Wavelength Calibration

The Manson soft x-ray source was capable of providing a calibration for wavelengths shorter than about 114 Å in first order. Clearly, for the VUV spectrometer to realize its maximum utility, this calibration had to be extended over the entire wavelength range covered by the instrument. To do this, use was made of a technique [19] which exploits the known ratio of oscillator strengths between certain pairs of doublet lines of impurity ions with only one valence electron (i.e. ions in the lithiumlike, sodiumlike, copperlike, etc... charge states).

Shown in Table 3.3 is a list of relevant doublet lines which were available for use in Alcator C-Mod. The wavelengths of these lines, along with a description of how those lines come to exist in the tokamak are listed. The transitions are all $\Delta n = 0$ from $np_{\frac{3}{2},\frac{1}{2}} - ns_{\frac{1}{2}}$ where $n = 2, 3, 4$ for the Li-like, Na-like, and Cu-like ions respectively. It can

element, charge state	wavelengths (Å)	method of introduction
Mo 31+ (Na-like)	128, 176	intrinsic, laser ablation
Ni 25+ (Li-like)	165, 234	laser ablation
Fe 23+ (Li-like)	192, 256	laser ablation
Cr 21+ (Li-like)	223, 280	laser ablation
V 20+ (Li-like)	240, 294	laser ablation
Ti 19+ (Li-like)	259, 309	laser ablation
Sc 18+ (Li-like)	279, 326	laser ablation
Fe 15+ (Na-like)	335, 360	laser ablation
Mo 13+ (Cu-like)	373, 423	intrinsic, laser ablation
Ar 15+ (Li-like)	353, 390	gas puff
Cr 13+ (Na-like)	390, 412	laser ablation
Ti 11+ (Na-like)	460, 480	laser ablation
Si 11+ (Li-like)	500, 520	laser ablation
Ne 7+ (Li-like)	770, 780	gas puff

Table 3.3: Pairs of doublet impurity lines in the lithiumlike, sodiumlike, and copperlike configurations available for calibration.

be seen that there is, in general, overlap between the wavelengths spanned by one doublet and those spanned by the next. This in principle allows for a continuous extension of the absolute calibration from the last wavelength accessible by the soft x-ray source to much higher wavelengths. Using the sensitivity measured using the Manson source at 114 Å as a tie-down point, the change in sensitivity over the range 128-176 Å, say, can be measured by comparing the observed brightnesses of the Mo 31+ lines.

The brightness of these lines as observed by the spectrometer can be written as:

$$B = \int \varepsilon(\mathbf{r}) \cdot d\mathbf{l} \tag{3.5}$$

where $\varepsilon(\mathbf{r})$ is the emissivity of the particular line. If the assumption is made that the upper levels of these transitions are populated by collisional excitation only, then using a conventional approximation for the electron impact excitation rates [20] for resonance transitions, this emissivity can be written as:

$$\varepsilon \propto n_e n_I \frac{f}{\Delta E \sqrt{(T_e)}} \exp\left(\frac{\Delta E}{T_e}\right) \tag{3.6}$$

where n_e and n_I are the local electron and impurity ion densities respectively, f is the absorption oscillator strength, ΔE and T_e are the transition energy and local electron

temperature. Viewed along identical lines of sight, the brightness ratio of the pair of doublet lines can therefore be written as:

$$\frac{B_{\frac{3}{2}}}{B_{\frac{1}{2}}} = \frac{f_{\frac{3}{2}}}{f_{\frac{1}{2}}} \frac{\Delta E_{\frac{1}{2}}}{\Delta E_{\frac{3}{2}}} \exp\left(\frac{\Delta E_{\frac{1}{2}} - \Delta E_{\frac{3}{2}}}{T_e}\right) \tag{3.7}$$

where subscripts $\frac{3}{2}$ and $\frac{1}{2}$ refer to transitions between that j level and the ground state. In principle, this brightness ratio is a known number based only on the atomic physics parameters included in equation 3.7 and on the local electron temperature in the region where the emissivity of the given line is dominant.

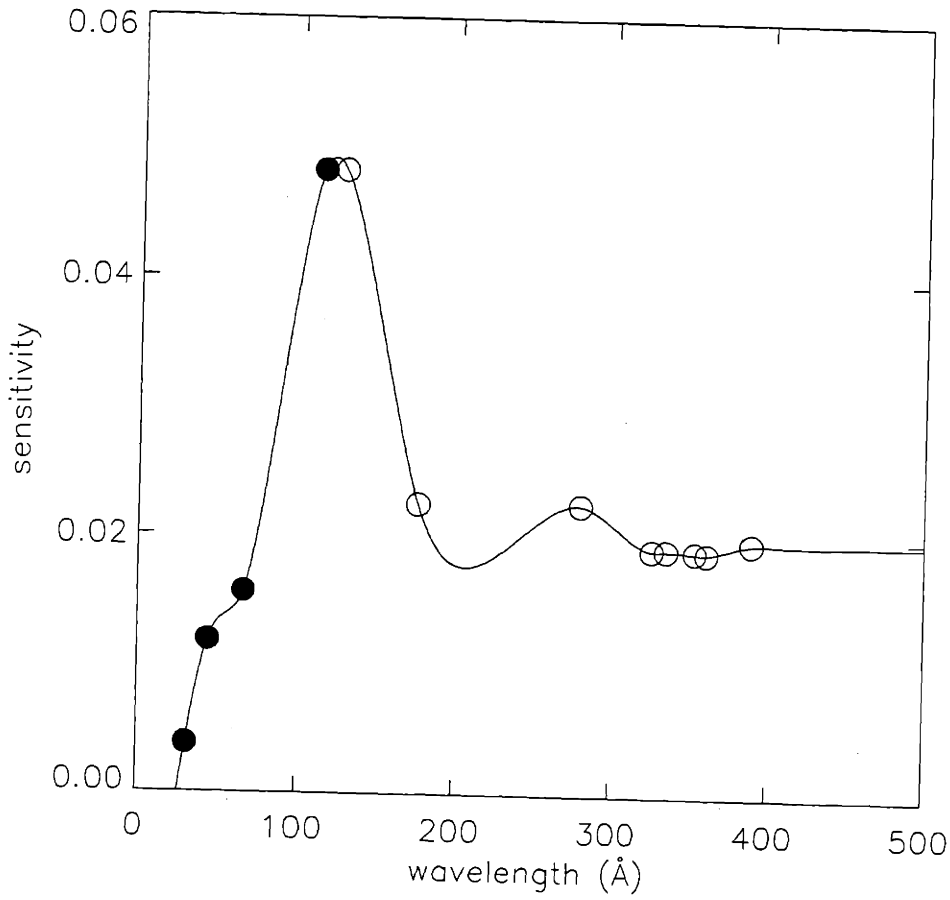

Figure 3-12: Spectrometer sensitivity as a function of wavelength in first order including the results of both the Manson source calibration (closed circles) and the doublet ratio calibration (open circles).

Modelling of the fractional abundance of the various impurities listed in Table 3.3 is able to determine the temperature where each of these lines emits most strongly (see Chapter 4 for more details of this fractional abundance modelling). Small errors in this determination are, in fact, not terribly important, since the exponential term in equation 3.7 is close to unity anyway as a result of the fact that most temperatures of highest emissivity are much larger than the difference in transition energies for the lines. Since the predicted ratio of the brightnesses of the doublet lines is known, a direct comparison with the observed ratio can now be made. If the sensitivity of the spectrometer over the wavelength range covered by the doublet lines is constant, then the observed brightness ratio should be equal to the predicted ratio. If the sensitivity has changed as a function of wavelength, however, there will be a difference between the observed and predicted ratios. This difference can then be used to correct for the sensitivity change over the relevant wavelength range. If this calibration is done in a stepwise manner beginning with a known sensitivity, a continuous function relating the sensitivity to the wavelength can be obtained. This was done on C-Mod using a number of the impurities listed in Table 3.3 using the sensitivity measured at 114 Å as the starting reference point. The results of this process are summarized by the sensitivity curve shown in Figure 3-12.

Notice that one of the first features which becomes apparent is the strong local maximum in the sensitivity at about 120 Å. As mentioned earlier, this is consistent with the shape of the response curve of the CsI photocathode. It can also be noted that from about 200 Å to 500 Å the sensitivity does not appear to change very much. Because of the inherent step-wise nature of this branching ratio technique, the estimated accuracy of the calibration at these higher wavelengths is decidedly lower than that obtained with the x-ray source directly. It is estimated that the accuracy of the sensitivity calibration up to about 120 Å is about $\pm 20\%$ based on the accuracy to which the flux from the Manson source could be measured. By the time the branching ratio method has extended this calibration to 500 Å it is estimated that the sensitivity is accurate to within about a factor of two.

wavelength region (Å)	instrumental resolution (FWHM Å)
40-60	1.5
60-80	3.0
80-100	4.5
100-140	7.0

Table 3.4: Typical instrumental resolution of the multi-layer mirror.

3.6 Cross-Calibration Using the Multi-Layer Mirror Polychromator

A multi-layer mirror polychromator has also been installed on Alcator C-Mod for viewing emission in the soft x-ray and XUV region of the spectrum [21]. This device is operated as a three channel polychromator capable of viewing simultaneously three distinct regions of the spectrum. During normal operation, the regions monitored are typically around 60 Å, 90 Å, and 130 Å. Of particular interest is the region around 120 Å since it contains the strong 3p-3s sodiumlike and magnesiumlike molybdenum lines. The multi-layer mirror is inherently a lower resolution device than the VUV spectrometer, and so some care has to be taken in the interpretation of signals obtained from it. Typical resolution for the device at different wavelengths is listed in Table 3.4.

The MLM instrument has been independently calibrated [21] at the Johns Hopkins University using techniques similar to those outlined for the VUV spectrometer. A different Manson soft x-ray source was used to provide several sensitivity points at different wavelengths of interest. The instrumental response function of the MLM instrument was also determined by scanning across the known natural width of the source lines.

With an independent calibration for both the VUV spectrometer and the MLM polychromator, a direct comparison of the signals obtained by these two instruments was made. This comparison is most important at the 128 Å region of the spectrum where the MLM instrument is used to monitor the sodiumlike molybdenum line. It is important to determine when this molybdenum line is dominant in the bandpass of the MLM instrument. When this is true, the signal obtained by the MLM instrument can be used

to infer molybdenum concentrations in the plasma. Shown in Figure 3-13 is the spectral region around 128 Å. The background continuum level which is subtracted away from the raw spectrum is also shown. In this region of the spectrum, the continuum is comprised of a contribution due to a large number of unresolved lines as well as a contribution due to some scattered light within the transmission system of the VUV spectrometer.

During low density operation ($\overline{n_e}_{20} \leq 0.8$), the molybdenum concentration in the plasma is typically high. In this case, the sodiumlike molybdenum line is dominant in the spectrum and agreement between the MLM instrument and the VUV spectrometer is found to be good. The signals typically agree to within about 15%. On the other hand, during high density operation ($\overline{n_e}_{20} = 1.8$), the molybdenum concentration in the plasma is low and the MLM instrument signal contains significant contribution from lines other than the sodiumlike molybdenum line. In these cases, agreement between the instruments is not as good. Discrepancies of up to a factor of two are sometimes found. These discrepancies at low molybdenum signal levels (brightness $\leq 4 \times 10^{14}$ ph/s/cm^2/sr can be accounted for by subtracting a roughly fixed baseline level from the MLM signal. This baseline level has been found to be about 2×10^{14} ph/s/cm^2/sr. For all of the subsequent analyses which make use of the MLM signals, this baseline level is already subtracted away.

3.7 Conclusions

This chapter has described the design and operation of the high resolution, time-resolving VUV spectrometer used on Alcator C-Mod. Details of the detector alignment and system gain characterization were given, along with a description of the techniques used to calibrate absolutely the sensitivity of the device. This absolute sensitivity calibration was performed from about 50 Å to about 500 Å using a combination of an x-ray source with an absolute detector and a method utilizing the constant emissivity ration between selected impurity doublet lines. The accuracy of the calibration is about ±20% at the

lower wavelengths and within about a factor of two at the higher wavelengths. Also demonstrated was good agreement in absolute sensitivity calibration with an independently calibrated lower resolution polychromator. The rewards of having performed this calibration will now be explored in the following chapters, where the use of the spectrometer to monitor and interpret various different impurity phenomena in the plasma will be discussed.

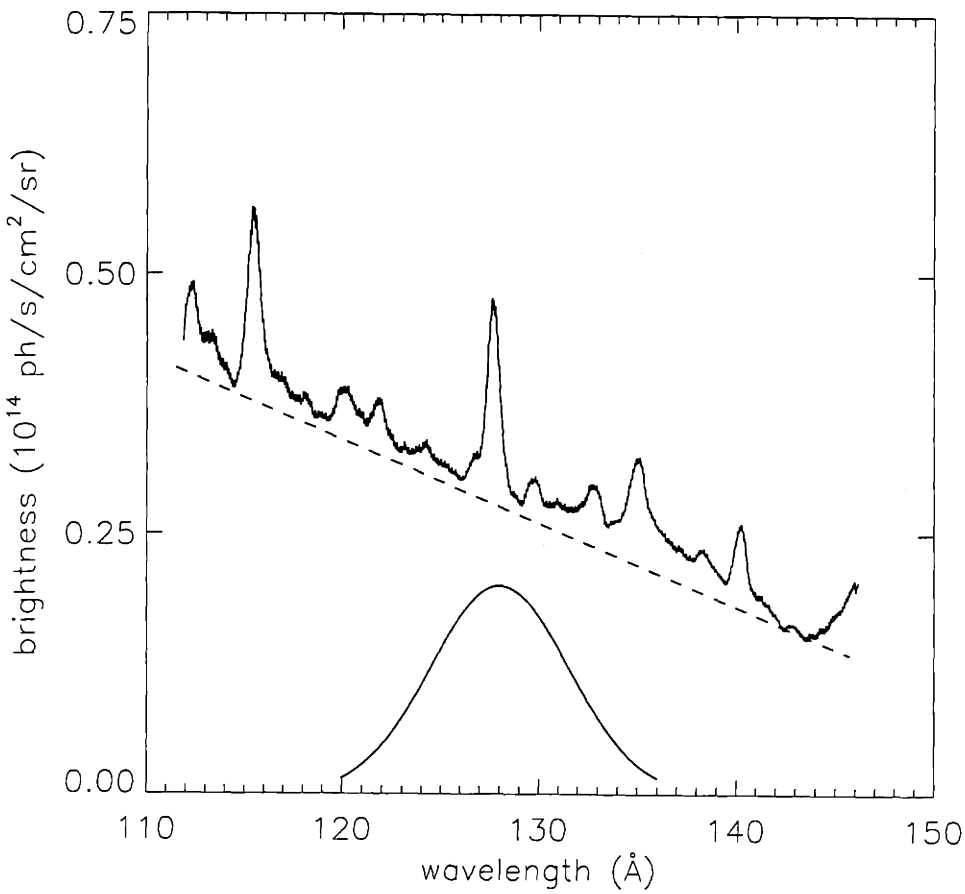

Figure 3-13: Spectrum taken with the VUV spectrometer showing the bandpass of the MLM polychromator channel around the $3s^2$-3s3p molybdenum line at 127.8 Å for a moderate density discharge. Also shown is the typical background level which is subtracted away from the VUV spectrum to give the true brightness of the molybdenum line.

Chapter 4

Atomic Physics Model

4.1 Introduction

A proper interpretation of observed impurity line emission depends on a reliable model for the atomic and transport processes occurring in the plasma. The brightness of any given impurity line is a strong function of the charge state distribution of that impurity, dictated by rate coefficients for the relevant ionization and recombination processes taking place and the local transport conditions in the plasma. These rate coefficients are generally functions of the electron temperature; the local transport is generally a function of various plasma parameters. To describe properly the total impurity picture in the plasma, the influence of all of these factors must be measured, calculated, or approximated in some way. This chapter will describe the techniques used to model the charge state distributions of different impurities in the plasma by taking into account atomic physics rate coefficients and plasma transport coefficients.

4.2 Charge State Balance

In a one-dimensional cylindrical geometry, it is possible to develop a relatively simple model which describes impurity transport. By solving a set of coupled differential equa-

tions, the evolution of all charge states of a given impurity can be followed in space and time. The evolution of the density, n_j, of an impurity with atomic number Z of charge $1 \leq j \leq Z$ is governed by [22]:

$$\frac{\partial n_j}{\partial t} = -\nabla \cdot \Gamma_j + n_e \cdot [n_{j-1} S_{j-1} + n_{j+1} \alpha_{j+1} - n_j (S_j + \alpha_j)] \tag{4.1}$$

where n_e is the electron density, S_j is the total ionization rate out of state j, α_j is the total recombination rate out of state j, and Γ_j is the local flux of impurity species j across a given radial surface. The functional form of the flux is generally found to be anomalous and is typically modelled as:

$$\Gamma_j = D \nabla n_j - V n \tag{4.2}$$

where D and V are the diffusion coefficient and convective velocity respectively (see Chapter 5 for details relating to how these coefficients are determined experimentally). Much has been written [23, 24] about various techniques to solve equation 4.1. For the purposes of the analysis conducted here, the MIST code [23] was chosen as the preferred tool to generate charge state balances. The MIST code solves equation 4.1 for a single impurity in a one-dimensional cylindrical geometry using atomic physics rate coefficients from a number of sources, depending on the impurity. Where well accepted experimental, theoretical, or semi-empirical coefficients exist for a given impurity, they are used directly. Examples of impurities which have well established databases of coefficients include carbon, oxygen, and other low Z elements which have been investigated at length in previous tokamak and other plasma physics experiments. For higher Z elements, where no such well established coefficients exist, generic formulas for the ionization and recombination rates are used [25]. These formulas are highly approximate and generally only reliable at predicting rate coefficients for low Z elements. For ionization rates, they include only contributions from electron impact ionization from the ground state. In higher Z elements it has been shown that other processes such as electron impact excitation followed by autoionization can be important [26]. For recombination rates, only a generic treatment of dielectronic recombination, which is generally the dominant recombination process for

the intermediate charge states of high Z elements, is included and is not able to address the complexity of electronic configurations of higher Z elements.

Where the coefficients used by the MIST code were deemed sufficiently accurate for application to C-Mod plasmas, they were used in their original form. In a number of instances, however, it became apparent that some of the rates used in the code were predicting results clearly contrary to observations. This was particularly true for molybdenum, an important intrinsic impurity in C-Mod. The experimental evidence which led to the conclusion that the molybdenum ionization, recombination, and excitation rate coefficients that were being used by the MIST code were inaccurate are presented in the sections that follow. The details of the improvements made to these rate coefficients are also given, along with the implications of those improvements on interpretations of the plasma molybdenum content.

A more general description of the ways in which line integrated spectroscopic measurements are interpreted in the context of impurity charge state and total density profiles is now presented. The importance of knowing accurately the background electron density and temperature profiles is also discussed along with a brief description of how these measurements are made on Alcator C-Mod.

4.3 Electron Density and Temperature Profiles

All of the modelling described in this thesis is dependent to some large extent on the electron density and temperature profiles used as inputs. The measurement of these profiles represents a significant effort by the C-Mod group and is of vital importance to a large number of performance related calculations and other diagnostics. A brief description of the techniques used to generate these profiles is therefore warranted.

Electron density is currently measured with a 10 channel interferometer system which operates at two separate wavelengths (10.6 μm and 643 nm). Each channel of the system provides a line-integrated measurement of electron density along a vertical chord through

the plasma [27]. The chords extend from a major radius of 0.66 m to a major radius of 0.85 m. The chordal measurements can be inverted using standard matrix inversion techniques to yield an electron density profile. One short-coming of this measurement scheme is that the radial coverage of the vertical chords is not sufficient to reach the edge of a typical plasma centered at R=0.69 m with a minor radius of 0.22 m. Thus, the value of the edge density determined by the inversion algorithm has a relatively high degree of uncertainty due to the lack of line-integrated measurements made at the edge. Attempts have been made to compensate for this by making use of an edge database of electron densities established on the basis of measurements made with a reciprocating Langmuir probe [28]. This database relates macroscopic plasma parameters such as plasma current and line-averaged electron density to corresponding values of edge density. The edge density values inferred from this database can then be used as inputs to the inversion algorithm for the electron density profile. This process can be repeated iteratively until convergence is reached. That is, the profile generated using the value of edge density from this database should in fact return that same value. The relationship that this database uses for edge density has been found to be [29]:

$$n_{e_{separatrix}} = 0.93\,(\overline{n_e} - 0.6) + 0.28 \tag{4.3}$$

where all of these densities are in units of $10^{20}m^{-3}$. Similarly, the e-folding width of the density in the scrape-off layer at the midplane (in mm) has been found to be described by:

$$\lambda_n = 7.0\left(\frac{\overline{n_e}}{I_p} - 1.0\right) + 4.9 \tag{4.4}$$

where the plasma current is given in MA. When used as input to the MIST code, or other atomic physics models used in this work, the inverted electron density profile is transferred to a mesh and joined together with the edge profile described by equations 4.3 and 4.4. A typical electron density profile assembled in this way is shown in Figure 4-1 on both linear and log scales.

The electron temperature profiles in Alcator C-Mod are measured with an electron cyclotron emission diagnostic [30]. This instrument measures the intensity of blackbody

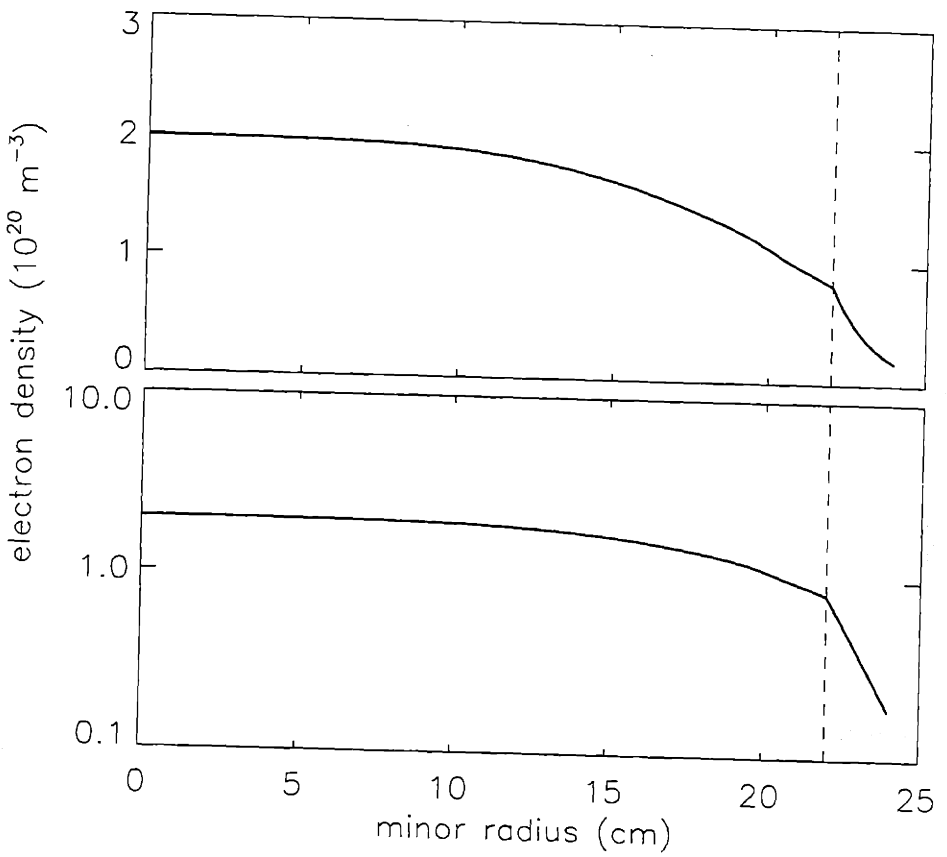

Figure 4-1: Typical electron density profile (including edge model) used for atomic physics modelling shown on a linear and a log plot.

emission at various frequencies and uses the known variation of toroidal magnetic field with major radius in the tokamak to localize the emission in the radial dimension. This diagnostic is able to measure electron temperatures down to about 200 eV before the optical depth of the plasma becomes too low for reliable interpretation of the emission spectra. Although the profiles generated in this way are independent of the edge temperature, an appropriate value of edge temperature is still necessary to provide a complete profile of the entire plasma since the 200 eV point typically occurs at least a couple of centimeters inside the separatrix. The edge database is again used to provide these temperature values at the separatrix and in the SOL. The electron temperature (in eV)

at the separatrix was found to be well-described by [29]:

$$T_{e_{separatrix}} = -10.7\left(\frac{\overline{n_e}}{I_p} - 1.0\right) + 28.5 \tag{4.5}$$

and the e-folding width in the scrape-off-layer at the midplane by:

$$\lambda_T = 10.9\left(\frac{\overline{n_e}}{I_p} - 1.0\right) + 2.3 \tag{4.6}$$

A typical electron temperature profile assembled in this way is shown in Figure 4-2 on both linear and log scales.

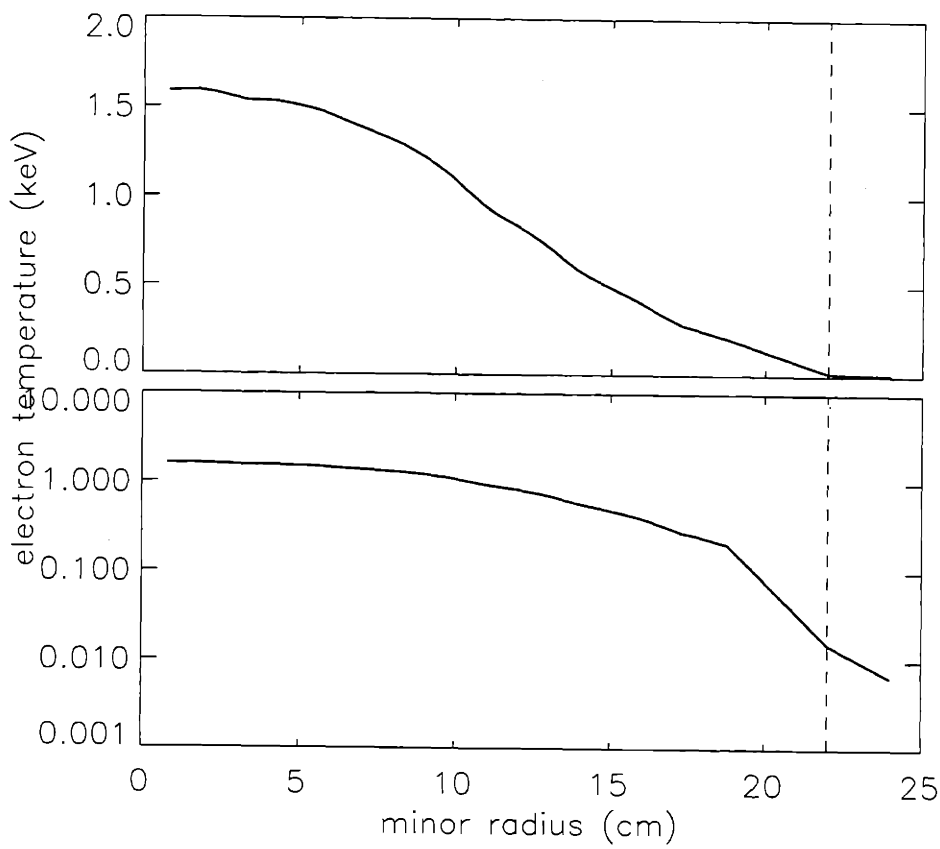

Figure 4-2: Typical electron temperature profile (including edge model) used for atomic physics modelling shown on both a linear and a log plot.

4.4 Interpretation of Chordal Brightness Measurements

All of the observations made with the various spectrometers described in this thesis are the result of chordal views through an emitting region of plasma. In order to relate these line-integrated measurements to specific local quantities, it is important to be able to interpret properly the effects of viewing through a region of varying emissivity. The procedure used to translate a one dimensional emissivity profile generated by the MIST code into a line integrated brightness measurement along a specific line of sight is outlined below.

In general, the viewing chord of a given instrument is known in absolute spatial coordinates (that is, with respect to the vacuum vessel). Details of how these views are determined for some instruments are given in Chapter 3. What needs to be defined is therefore the position of the plasma with respect to those same coordinates. This is done using the EFIT equilibrium reconstruction code. As outlined earlier, using as inputs magnetic measurements from B_p coils, flux loops, and Rogowski coils, this code calculates the magnetic geometry of the plasma as a function of time for each discharge. This geometry allows a visualization of surfaces of constant flux in the plasma as well as a clear identification of the separatrix or last closed flux surface. A typical reconstruction showing nested flux surfaces each is given in Figure 4-3. The separatrix for this diverted discharge is shown with a heavy line and the magnetic axis of the plasma is marked with a cross. Superimposed on this reconstruction is a typical line of sight view of the VUV spectrometer.

One assumption which is crucial in allowing a one-dimensional profile to be applied to this inherently two-dimensional geometry is that the properties of the one-dimensional quantity (eg. n_i, n_e, n_I, T_e, etc...) permit it to be considered a flux function. That is, the quantity must be such that it is essentially constant on a surface of constant magnetic flux. This assumption is good for charged particles which have a parallel

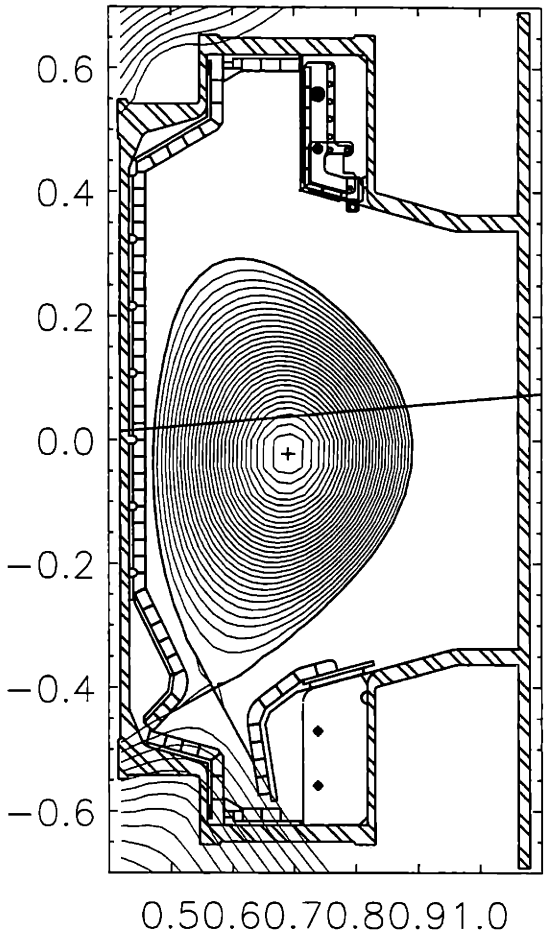

Figure 4-3: EFIT reconstruction of a typical diverted plasma showing surfaces of constant flux. Also shown is a typical line of sight view of the VUV spectrometer.

transport time which is much faster than their perpendicular transport time. Since parallel transport is restricted to a given flux surface, meeting this transport condition ensures that equilibration will occur in the poloidal plane on a given flux surface before cross-field transport is able to introduce a poloidal asymmetry in the profile. Parallel transport is generally dominated by the thermal velocity of the charged particles, which is large even for relatively heavy ions at temperatures of interest in fusion plasmas. The perpendicular transport, however, is dominated by cross-field diffusion, which is in general orders of magnitude smaller for both electrons and ions. For all of the analysis which is to follow, therefore, it is assumed that all charged particle densities as well as

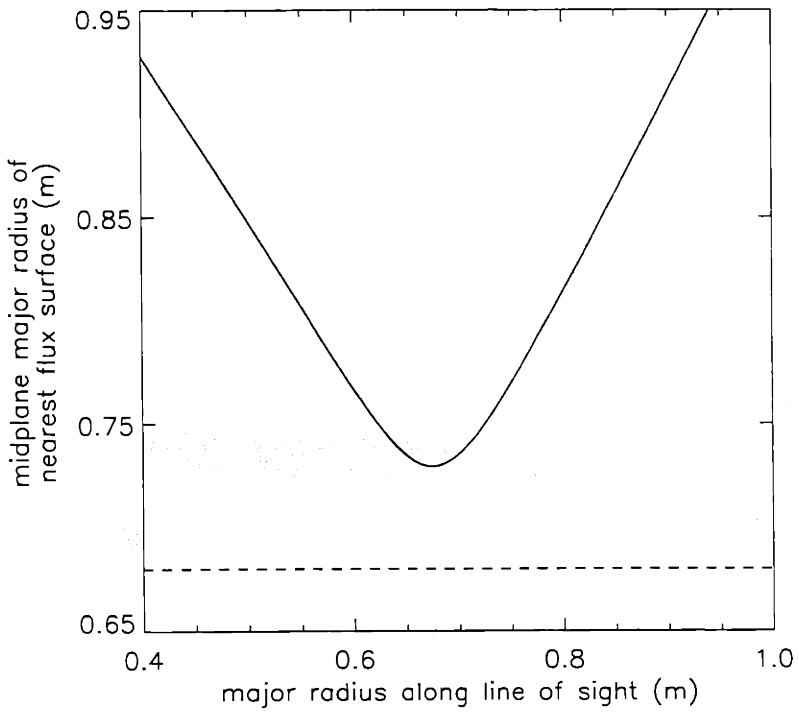

Figure 4-4: Transformation of the line of sight from Figure 4-3 into midplane coordinates of the flux surface of closest approach. The major radius of the plasma center is shown with the dotted line.

the electron temperature are flux functions. This implies that the radiation emissivity from impurities is also a flux function.

From Figure 4-3, it is possible to refer every point along the spectrometer line of sight to a flux surface coordinate which can be related to a major radius coordinate at the plasma magnetic axis. Performing this operation for the geometry and the line of sight shown in Figure 4-3, a relation between the major radius position of the line of sight and the minor radius position of the flux surface tangent to the line of sight at that radius can be obtained. This transformation is shown in Figure 4-4. Using the transformed line of sight of the spectrometer, a given one-dimensional emissivity profile can be integrated along that line of sight to yield a brightness measurement. For various arbitrary one-dimensional emissivity profiles, the profile actually sampled along the given line of sight is shown in Figures 4-5. Each of these emissivity profiles is representative

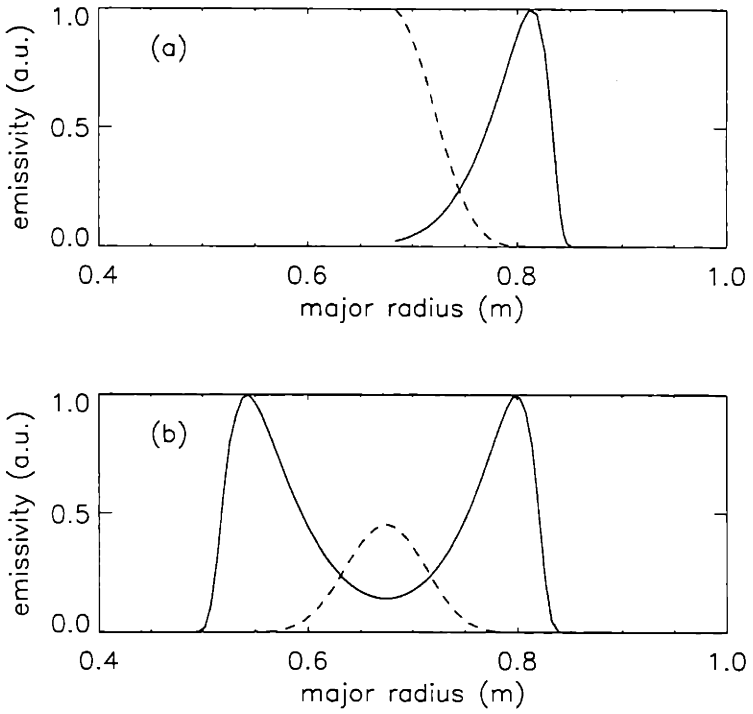

Figure 4-5: (a) Typical peaked and hollow one dimensional emissivity profiles of unit amplitude. (b) Profiles as sampled along the line of sight shown in Figure 4-3.

of typical centrally peaked and hollow profiles respectively. Following integration along a line of sight, the result is a single value of brightness observed by the spectrometer for the given assumed emissivity profile. This value can then be compared directly with an experimentally observed brightness.

4.5 Molybdenum Charge State Profiles

Observations of brightness profiles from a number of charge states of molybdenum have been made using x-ray and VUV spectroscopic diagnostics. These profiles have been used to compare predictions made by the MIST code for a number of ionization/recombination models. The profiles were determined by conducting a spatial scan of spectrometer chords during a number of reproducible discharges. To enhance the molybdenum signal during

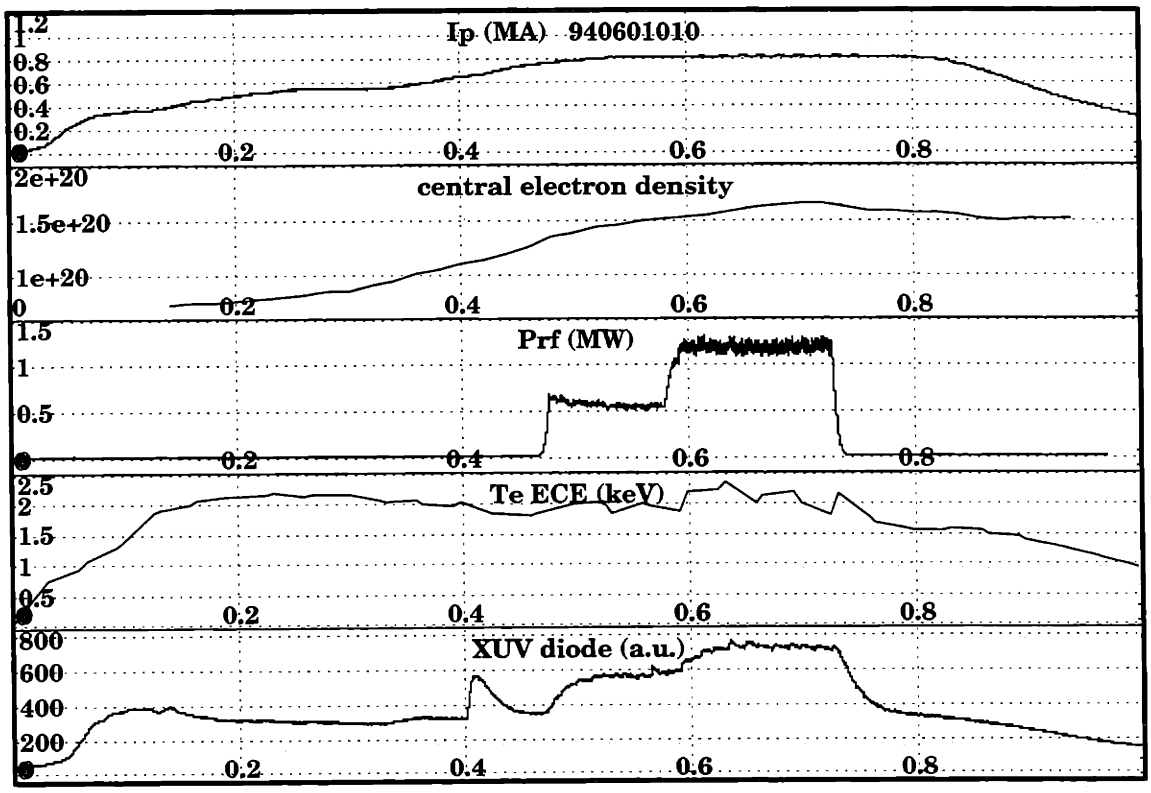

Figure 4-6: Plasma parameters during a series of discharges used to measure brightness profiles of a number of molybdenum lines from different charge states.

these discharges, laser blow-off injections of molybdenum were made early in the shot, and ICRF power was injected later in the shot in order to raise the temperature and the overall plasma impurity content. Typical plasma parameters during these reproducible discharges are shown in Figure 4-6. The McPherson VUV spectrometer with its single chordal view was scanned over a range of impact parameters from -18 cm to +17 cm. Lines from sodium (+31), magnesium (+30), and like molybdenum were observed at all of these impact parameters. The HIREX spectrometer array (described in Chapter 1) was also used over a similar range of impact parameters to observe x-ray lines from fluorine (+33), neon (+32), sodium (+31), and magnesium (+30) like molybdenum. The transitions observed are listed in Table 4.1. In order to ensure reproducibility from one shot to the next, the multi-layer mirror based molybdenum monitor with its view fixed through the center of the plasma was used to normalize the observed signals. Good pro-

charge state	transition	wavelength (Å)
29+	3p-3d	122.0
30+	3s-3p	116.0
31+	3s-3p	127.8
31+	2p-4d	3.789
32+	2p-4d	3.740
33+	2p-4d	3.605

Table 4.1: High and intermediate charge state molybdenum transitions used for profile comparisons.

files were obtained in the VUV region of the spectrum during the laser blow-off injection phase of the discharges. Problems with saturated signals during the RF phase of the discharges prevented profiles from being obtained in the VUV during those times. Good profiles were obtained in the x-ray during both the injection and the RF phases.

The simultaneous observation of many adjacent charge states provides a very strong constraint on the predictions of any model used to provide the charge state ionization balance. Consistency in the widths of the measured and predicted spatial profiles and intensities of emission from different transitions must be obtained in order for the model to be considered accurate in its predictive ability. Comparisons were first made with the original ionization/recombination model as it existed in the MIST code. The code was run using the anomalous transport coefficients measured with the technique outlined in Chapter 5 in order to obtain the radial charge state density profiles. For these discharges, those transport coefficients were D=0.5 m^2/s and S=0.5. For the injection phase of the discharges, a time-dependent MIST simulation was run. For the RF phase, a simple equilibrium MIST simulation was run. Once the predicted charge state density profiles were obtained, the emissivities of the various observed lines were calculated using modelled excitation rates. For all of the lines considered, the assumption was made that the upper levels of the transitions were populated by electron impact excitation from the ground state. This is, in general, a good assumption for lines which are well connected to the ground state. The relevant parameters which define this excitation rate are also given in Appendix A for the transitions presented here. The profiles of the predicted brightness of

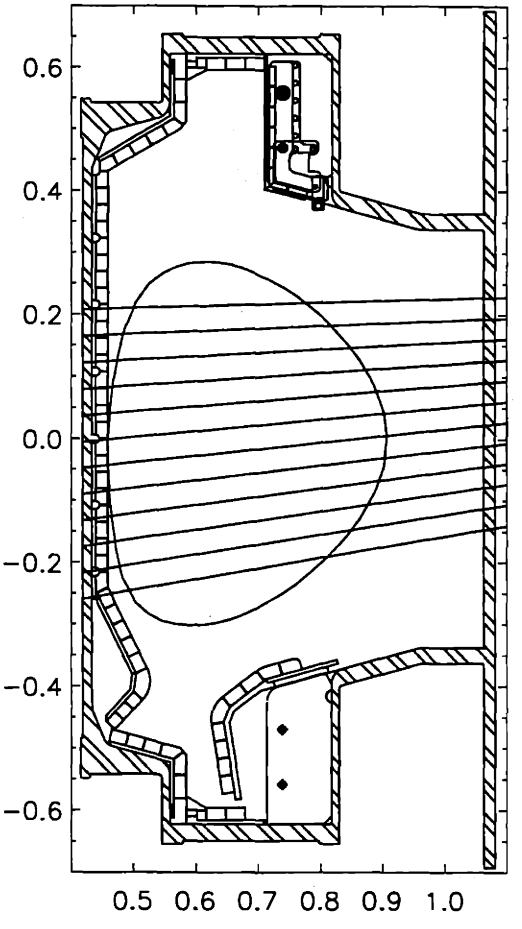

Figure 4-7: Line of sight views used when calculating predicted brightness profiles of the VUV lines.

these lines was generated by integrating the calculated emissivity profiles over a range of lines of sight as shown in Figures 4-7 and 4-8 for the VUV spectrometer and the HIREX spectrometer respectively.

Using the original semi-empirical atomic physics data (ie. ionization/recombination rates), poor agreement was seen when comparing profiles and absolute intensities from different charge states. This comparison is shown in Figures 4-9 and 4-10 for the lines in the VUV and the x-ray regions of the spectrum respectively. The VUV brightness profiles include the sodiumlike, magnesiumlike, and aluminumlike charge states. The modelled profiles shown have been normalized to the sodiumlike predictions. Clearly the agreement

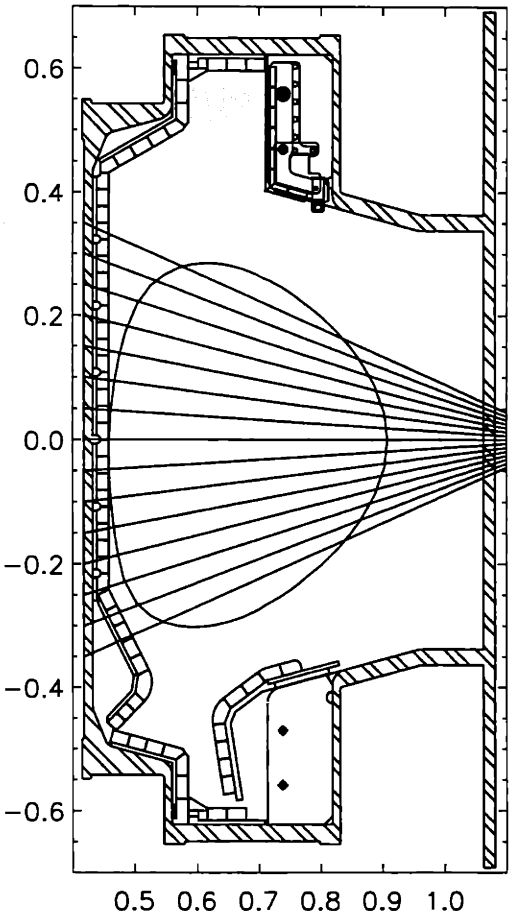

Figure 4-8: Line of sight views used when calculating predicted brightness profiles of the x-ray lines.

is poor. Discrepancies of more than a factor of five are seen in the aluminumlike profile. The x-ray brightness profiles include the fluorinelike, neonlike, and sodiumlike charge states. The modelled profiles have in this case also been normalized to the sodiumlike predictions. Again the agreement is seen to be poor. Discrepancies of up to a factor of five exist in the fluorinelike and neonlike profiles.

An examination of the discrepancies in these comparisons led to the conclusion that the original atomic physics data being used by the MIST code were underestimating the degree of ionization which was actually being observed. That is, not enough of the higher charge states were being predicted by the original model. This is clearly evidenced in

the much broader observed profiles of the neonlike and the fluorinelike charge states. An updated model for the ionization/recombination physics which was to be implemented therefore had to address these shortcomings.

Improved ionization and recombination rates were calculated by the Atomic Physics Group at Lawrence Livermore National Laboratory (LLNL) as part of an ongoing collaboration with the Alcator C-Mod group. A detailed description of these calculations can be found in [26, 31]. Briefly, though, these calculations undertake an *ab initio* treatment of an ion in a given charge state and include processes for electron impact ionization, excitation followed by autoionization, and radiative and dielectronic recombination which takes into account the full electronic configuration of each ion. The initial modifications to the model included updated rates for all charges states from potassiumlike (23+) through to fluorinelike (33+). These were introduced to the MIST code as parameterized fits to simple functions of electron temperature which approximated the calculated rates and replaced the existing rates for the charge states mentioned. Where new rates were not available, the original semi-empirical model rates were used. The functional form which provided a best fit to the new total ionization rates was:

$$S_{iz} = a_0 \exp\left(-\frac{a_1}{T_e}\right) \tag{4.7}$$

The best fit to the new radiative recombination rates was:

$$\alpha_{rr} = \frac{b_0}{T_e} \exp\left(-\frac{b_1}{T_e}\right) \tag{4.8}$$

The best fit to the new dielectronic rates was:

$$\alpha_{dr} = \frac{c_0}{T_e^{c_2}} \exp\left(-\frac{c_1}{T_e}\right) \tag{4.9}$$

where the coefficients a_i, b_i, and c_i are determined for each charge state. These coefficients for each charge state are listed in Appendix A.

The model with the new rates was then used to recalculate the predicted brightness profiles for each of the lines listed in Table 4.1. These new comparisons are shown in Figures 4-11 and 4-12. The agreement now is clearly much better. For the VUV lines,

the agreement is now within about 30% for the three profiles shown. This is a marked improvement over the nearly factor of five seen previously. The agreement for the x-ray lines is even better. Consistency to within about 20% is seen as compared with factors of five seen previously. The predicted profile widths now also agree much better with the observed profiles.

A clear demonstration of the influence of the improved ionization and recombination rates can be found by comparing the fractional abundance curves for molybdenum generated by each model. The fractional abundance of charge states 18+ to 40+ is shown in Figures 4-13 and 4-14 as a function of electron temperature from 500 eV to 5 keV. These abundances are clearly very different. In particular, notice that the peak of abundance of most charge states has been shifted to a lower electron temperature. This is why the higher charge states, which were being underpredicted by the original model, are now in close agreement with predictions. The major contributing factor to this change in the fractional abundances has been the inclusion of additional important processes in the determination of the total ionization rate and the more accurate modelling of the dielectronic recombination rate. It has been found that the effect of electron excitation followed by autoionization (EA) can be a dominant process in many of the charge states investigated. Where this process has been included, the total ionization rate has increased by almost 50% at the temperatures of interest in these plasmas. Improvements to the dielectronic recombination rates have also led to marked changes in those rates from the approximate calculations which existed previously. Again, refer to Appendix A for a graphical representation of the differences in these rates from the original model to the improved model.

4.6 Conclusions

This section has outlined the techniques used to determine impurity charge state and total impurity density profiles from spectroscopically observed line brightnesses. The mapping

from the line of sight of a particular spectroscopic instrument to a one-dimensional mid-plane grid consistent with the MIST code model has been described and typical results have been shown. The importance of electron density and temperature profiles has been highlighted, and the experimental and analytical techniques used to generate these profiles for use by the MIST code have been described. Evidence that the ionization and recombination rates used by the original version of the MIST code were unable to predict correctly the experimentally measured molybdenum charge state profiles has been shown. The improvements made to the ionization and recombination rates have been outlined and an excellent match between measured and predicted profiles has been demonstrated. The MIST code and the concomitant post-processing package developed as part of this thesis are now in a state where they may be used to fullest advantage for the analysis of a wide variety of impurities. The application of this analysis technique to a number of tokamak discharges is now presented in the chapters that follow.

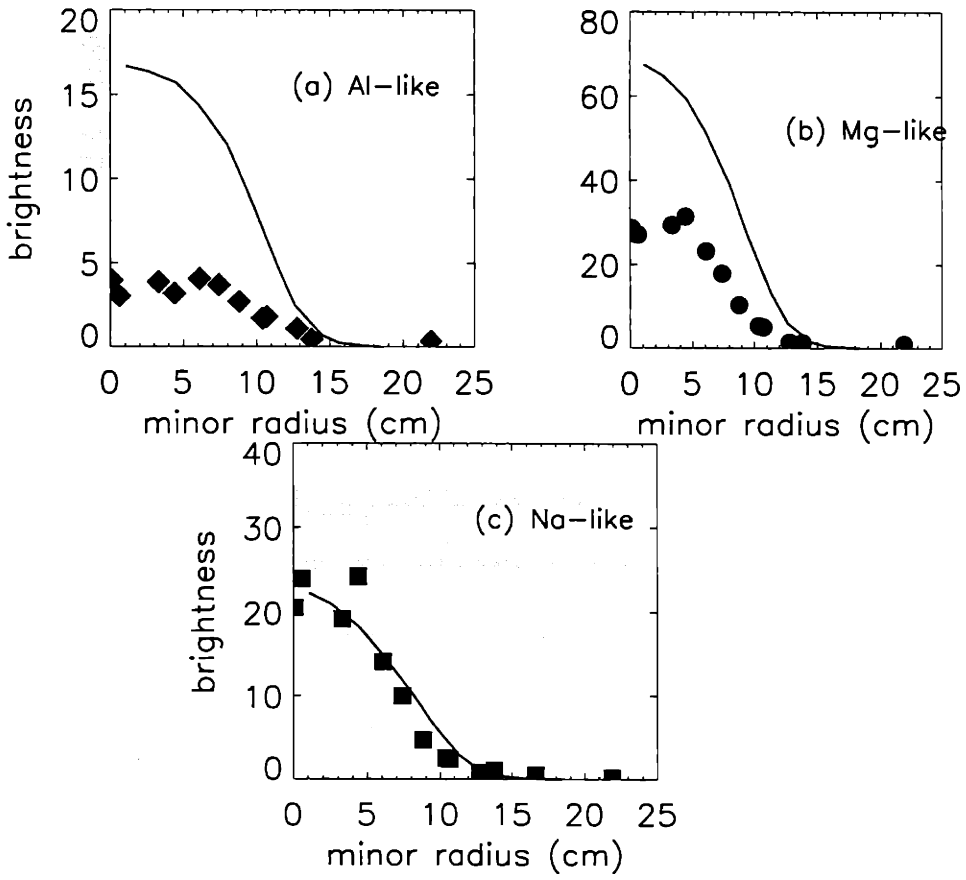

Figure 4-9: Comparison of predicted (solid curve) and measured (circles) profiles for various charge states of molybdenum based on observation of different VUV lines. The predicted profiles were generated using rates for ionization and recombination calculated with the approximate formulas found in the original MIST code and have all been normalized to the sodiumlike profile.

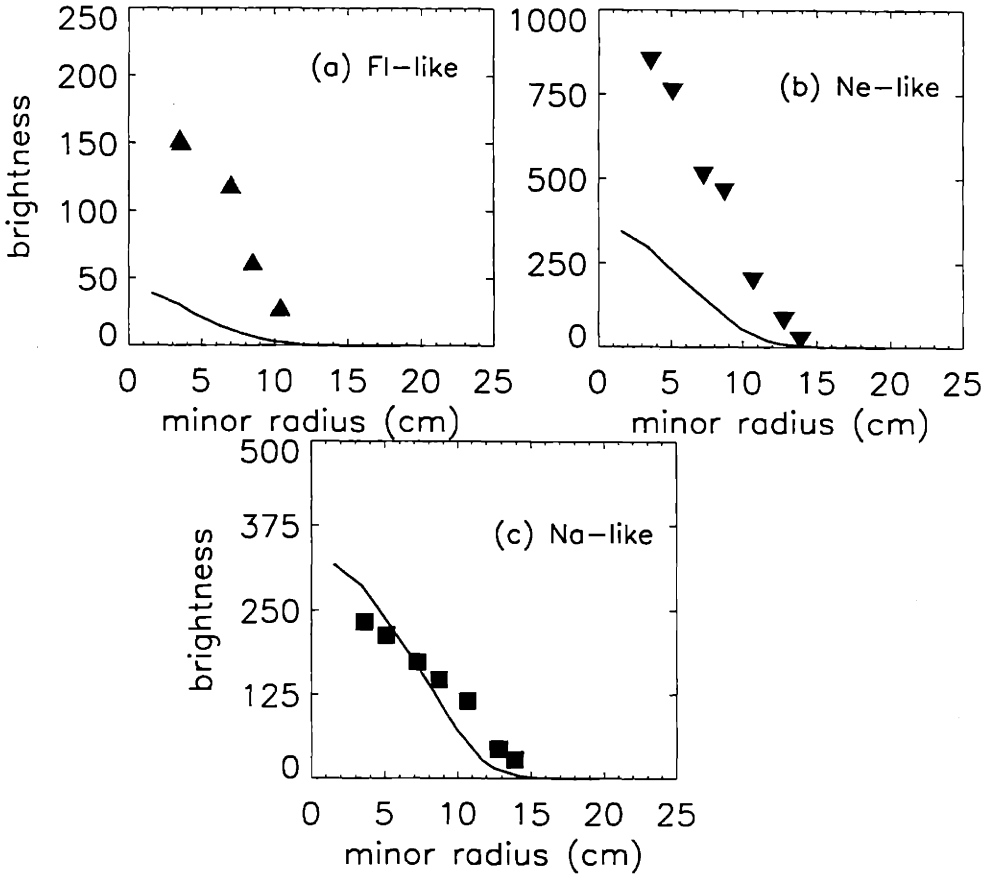

Figure 4-10: Comparison of predicted (solid curve) and measured (circles) profiles for various charge states of molybdenum based on observation of different x-ray lines. The predicted profiles were generated using rates for ionization and recombination calculated with the approximate formulas found in the original MIST code and have all been normalized to the sodiumlike profile.

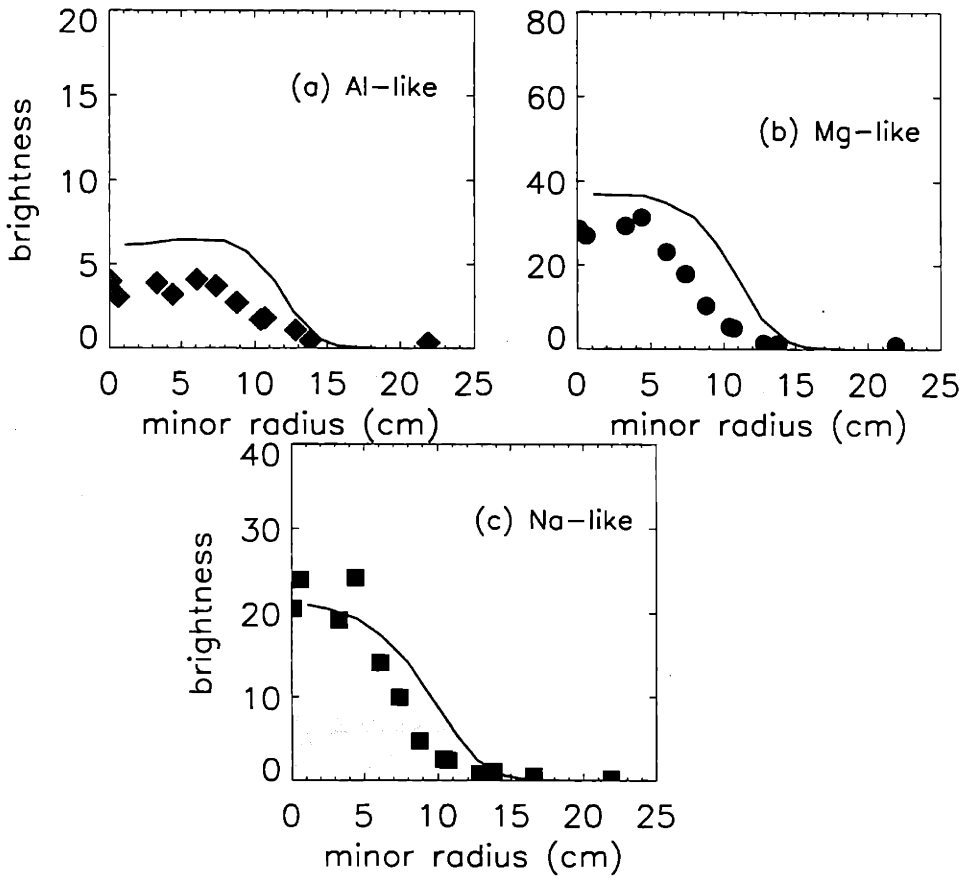

Figure 4-11: Comparison of predicted (solid curve) and measured (circles) profiles for various charge states of molybdenum based on observation of different VUV lines. The predicted profiles were generated using rates for ionization and recombination calculated with the improved formalism discussed in the text and have all been normalized to the sodiumlike profile.

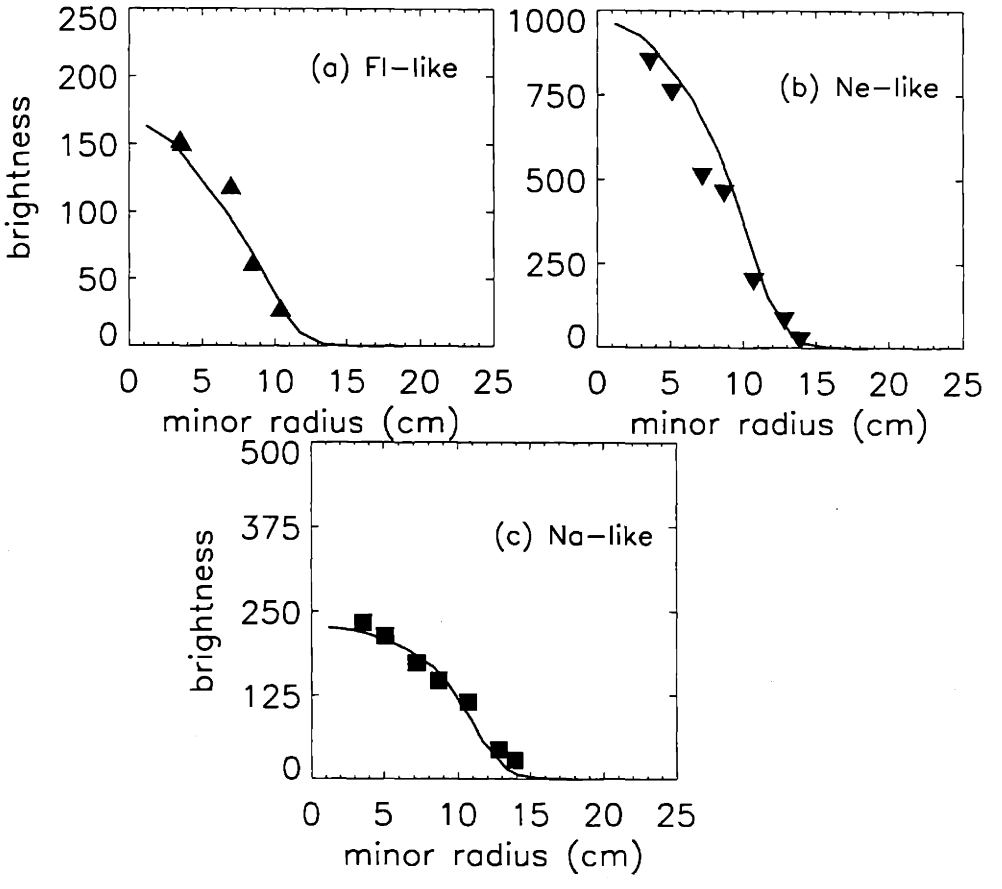

Figure 4-12: Comparison of predicted (solid curve) and measured (circles) profiles for various charge states of molybdenum based on observation of different x-ray lines. The predicted profiles were generated using rates for ionization and recombination calculated with the improved formalism discussed in the text and have all been normalized to the sodiumlike profile.

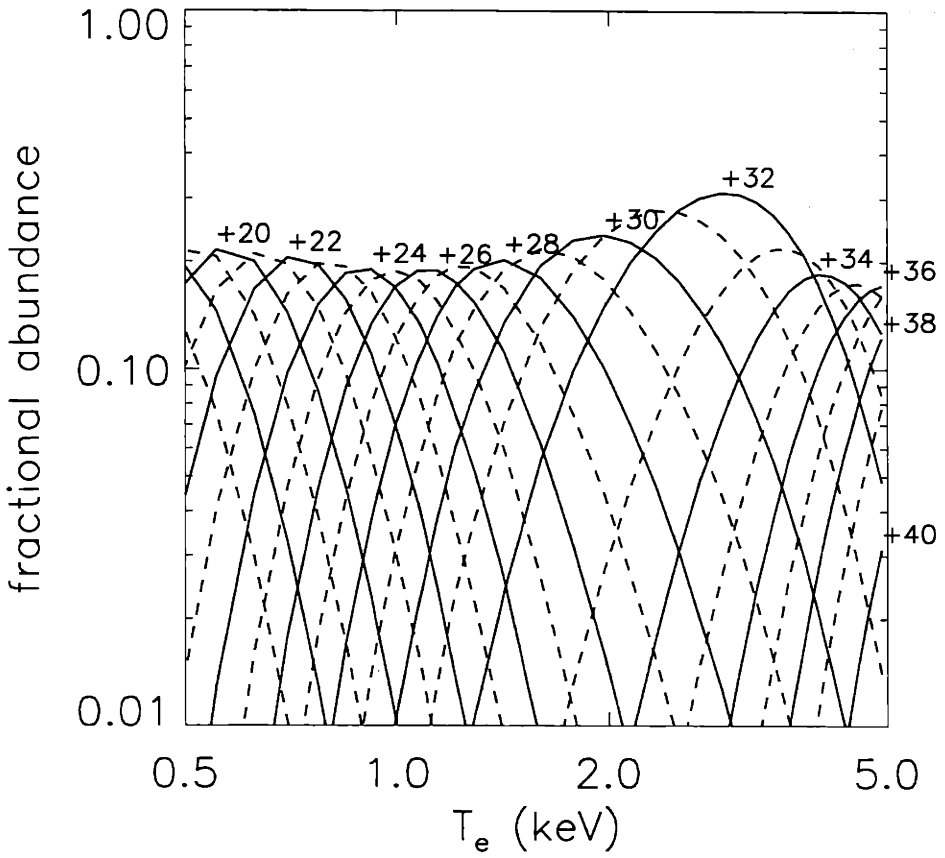

Figure 4-13: Fractional abundance of intermediate and high charge states of molybdenum calculated with the original MIST ionization/recombination rates.

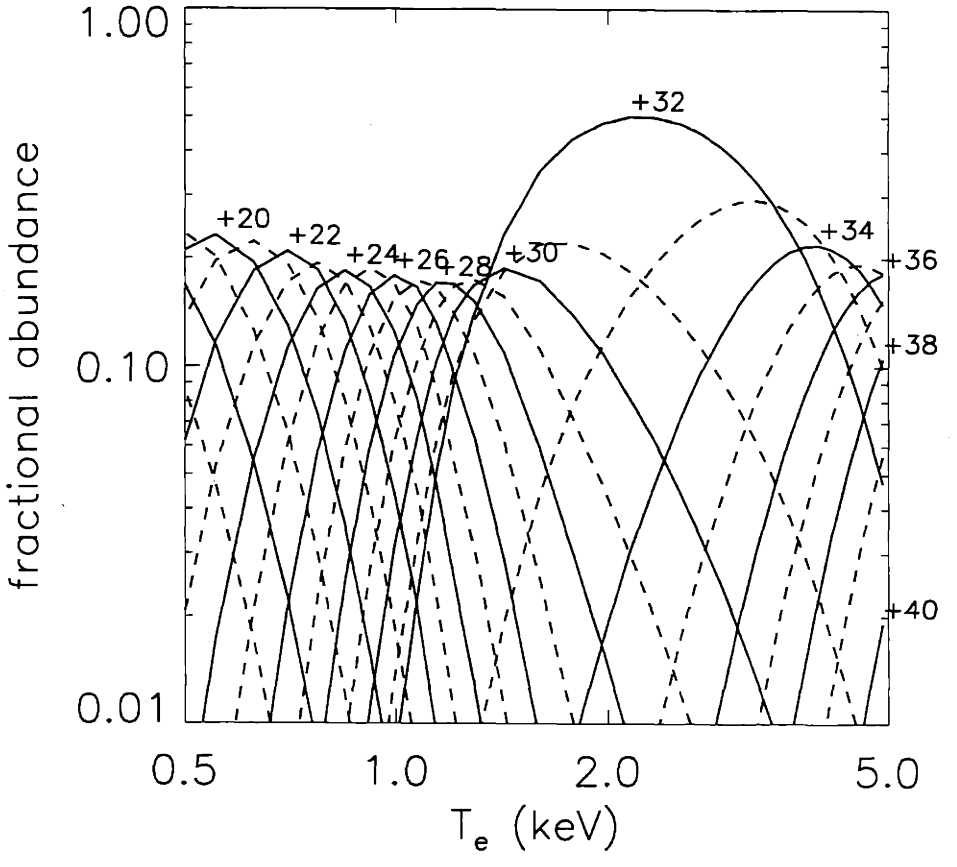

Figure 4-14: Fractional abundance of intermediate and high charge states of molybdenum calculated with the improved ionization/recombination rates.

Chapter 5

Impurity Confinement and Transport Measurements

5.1 Introduction

In order to understand better the role impurities play in tokamak plasmas, it is necessary to characterize the transport which governs their behaviour. A systematic study of the behaviour of these impurities in different operating regimes over a wide range of plasma parameters is therefore important. Many tokamaks have conducted such systematic studies with the hope of developing universal scaling relationships for quantities such as the impurity particle confinement time and the impurity transport coefficients [32]. While the predictive behaviour of these scaling relationships is generally good for the machine on which they were derived, fundamental quantitative and even qualitative differences from one machine to the next have been found.

Such differences are most easily highlighted by considering the scaling of impurity particle confinement time derived on different machines. Work carried out on the Alcator C tokamak [22] concluded that an impurity confinement time scaling was inversely proportional to the safety factor, q. Similar studies on the TEXT machine [33] concluded a that the dependence was inversely proportional to the plasma current I_p, which is ex-

actly opposite the Alcator C scaling since $q \propto \frac{1}{I_p}$. Other scalings, such as the mass of the background gas, m_{bg} dependence and the Z_{eff} dependence, on the other hand, proved to be similar in both cases. The major dependencies which can be compared directly for impurity particle confinement time found in each case are below:

$$\tau_{\text{Alcator C}} \propto \frac{Z_{eff} m_{bg}}{q} \propto Z_{eff} m_{bg} I_p \tag{5.1}$$

$$\tau_{\text{TEXT}} \propto \frac{Z_{eff} m_{bg} \overline{n_e}}{I_p} \tag{5.2}$$

Various explanations for this qualitative difference in scaling with plasma current have been proposed [33].

The sections that follow describe experiments conducted to develop an impurity particle confinement time scaling relationship for Alcator C-Mod and to reconcile the observations with scaling relationships derived elsewhere.

5.2 Experiment

5.2.1 Hardware

The laser ablation impurity injection system (see Chapter 2) was used to investigate impurity particle transport in Alcator C-Mod. A series of injections of various impurity species was made into plasmas with different background parameters in order to study the dependence of impurity particle confinement time on these parameters. Injections of a given impurity (scandium) were made into ohmic and ICRF heated limited and diverted discharges with varying plasma current in the range $0.4 \leq I_p \leq 1.0MA$ at roughly fixed electron density. Further injections of scandium were then made as the electron density was varied in the range $0.8 \leq \overline{n_{e20}} \leq 2.0m^{-3}$ at a fixed plasma current of 0.8 MA. Similar injections were also made into hydrogen and helium discharges to investigate any isotopic dependence which might be present. The injected species was also varied during a series of discharges at fixed plasma parameters over the range of Z=13 (aluminum) to Z=42 (molybdenum). The injections were typically made during the quiescent phase of the

discharge when neither the plasma density, temperature, current nor magnetic geometry were changing. The injections were kept sufficiently small that typically no perturbation to electron density or temperature was noticed. The time evolution of central charge states of the impurity was monitored and used to characterize the particle confinement time for the given impurity.

5.2.2 Analysis

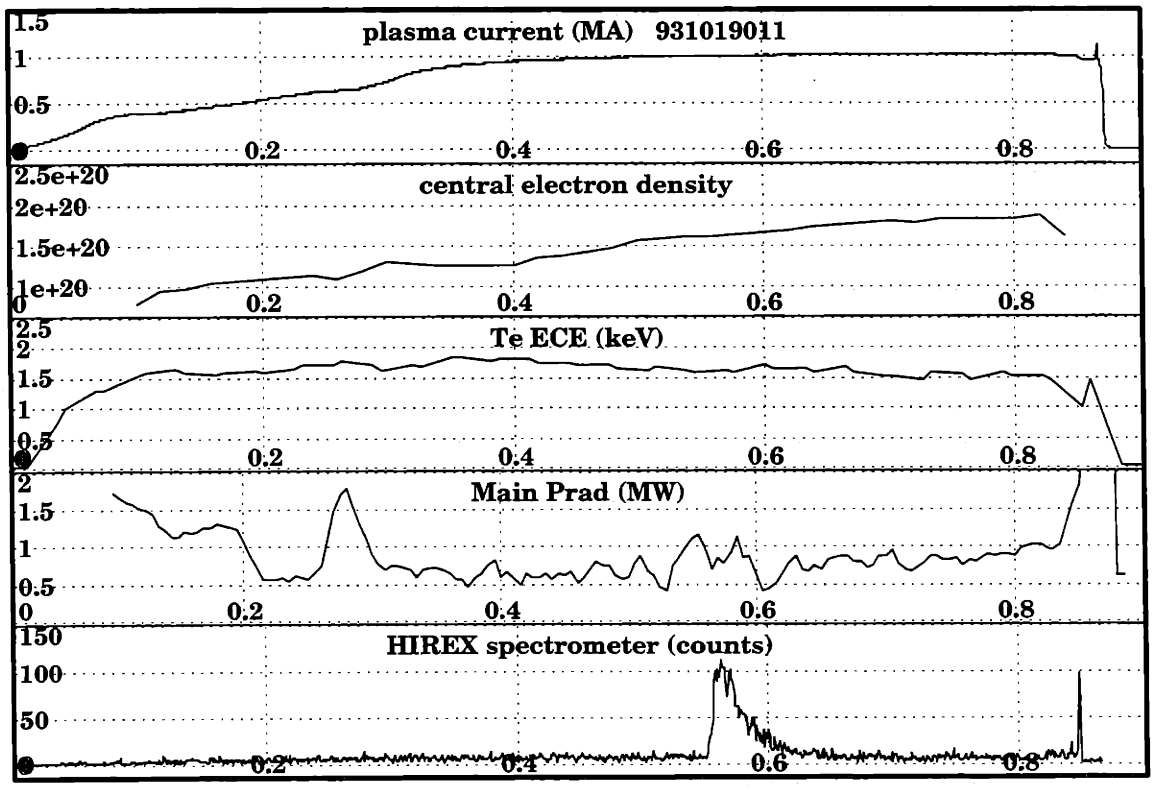

Figure 5-1: Typical time evolution of a high charge state of scandium viewed along a central chord. Also shown is the evolution of background plasma parameters during the injection.

A typical time evolution of a central charge state of injected scandium observed with the HIREX spectrometer viewing along a central chord is shown in Figure 5-1 along with the evolution of background plasma parameters. This evolution is typical of most laser blow-off injections. The brightness of the observed line is seen to peak rapidly (in a few milliseconds) following the injection as the impurity is transported radially

across field lines to the center of the plasma. There then follows an exponential decay of the brightness on a longer timescale (tens of milliseconds) as the impurity diffuses outward and is lost from the plasma. It is this exponential decay which is indicative of the impurity particle confinement time. This time is measured by fitting the decay of the observed time evolution of a single line brightness or multiple line brightnesses to a curve of the form $A_0 + A_1 \exp\left(-\frac{t}{\tau_{imp}}\right)$ where τ_{imp} is the impurity particle confinement time and A_0 is the background pre-injection signal level which is typically zero for non-intrinsic impurities on all except the broadband soft x-ray diode observations. This background level is subtracted away from the signal before the fitting routine is applied.

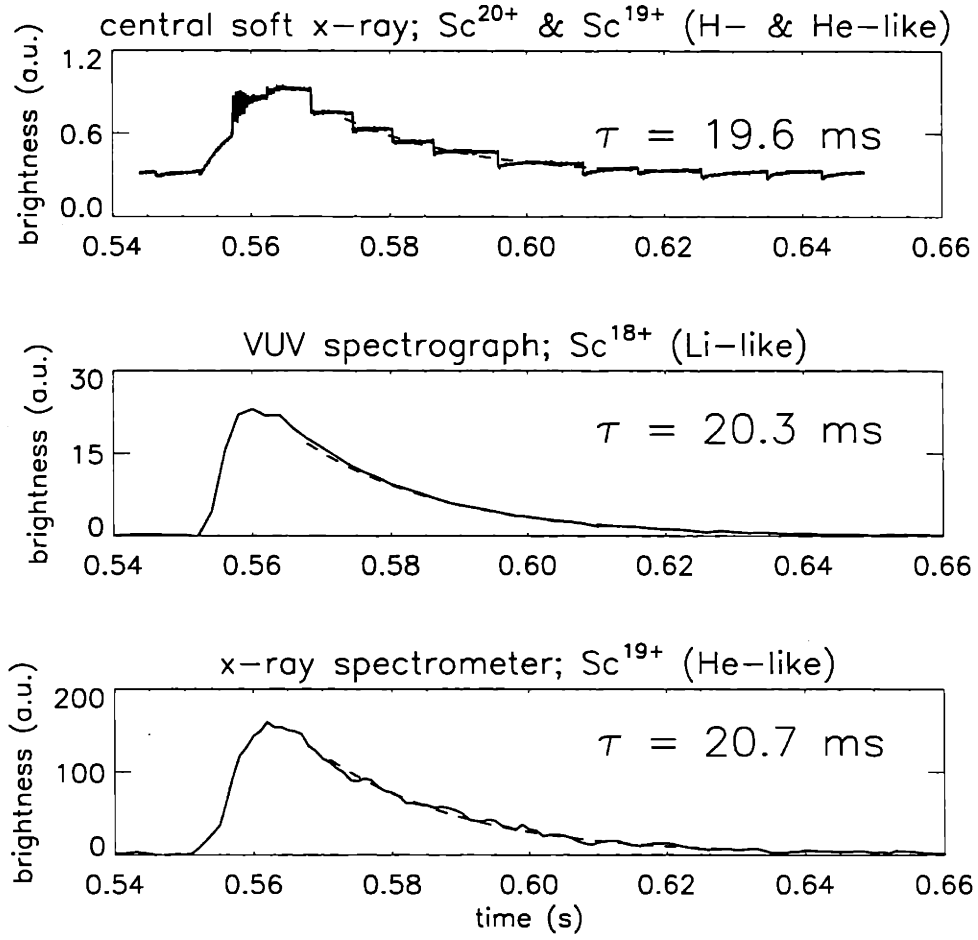

Figure 5-2: Comparison of impurity particle confinement time measured with different spectroscopic diagnostics for a laser ablation scandium injection at t=0.55 s.

instrument	charge state	transition	wavelength (Å)
HIREX x-ray spectrometer	19^+	$1s^2 - 1s2p$	3.0
soft x-ray diodes	$19^+, 20^+$	many	≤ 10
VUV spectrometer	18^+	$2s - 2p$	259.0

Table 5.1: Observed transitions for impurity confinement experiments using laser ablation scandium injections.

The evolution of a central or near-central state of an injected impurity is typically observed using a number of spectroscopic diagnostics, each of which may be measuring different atomic transitions. For the case of scandium injections, a number of central charge states are observed using the HIREX x-ray spectrometer array, the soft x-ray diode arrays, and the VUV spectrometer. A summary of the transitions observable by these instruments is given in Table 5.1. As a check on the robustness of the measurement of the impurity particle confinement time, the exponential decay observed by all of these diagnostics should be the same within the experimental error. For the injection shown in Figure 5-2, it is demonstrated that this is in fact the case. The inferred particle confinement time is found to be consistent to within about 5% using the three different diagnostics with similar chordal views through the center of the plasma.

5.3 Confinement Time Scaling

A database of 50 injections of a number of different species into various types of discharges has been established. It is useful to perform non-linear regression analyses on this database to identify the plasma parameters which have the greatest influence on the impurity particle confinement time. A study of impurity confinement times on Alcator C [22] discovered a scaling relation for τ_{imp} (in seconds) of the form:

$$\tau_{imp} = 0.75 a R^{0.75} \frac{Z_{eff}}{Z_{bg}} \frac{m_{bg}}{q} \tag{5.3}$$

where the minor radius, a, and the major radius, R, are given in meters, and the mass of the background gas, m_{bg} is given in amu. Z_{bg} refers to the atomic number of the

background gas. This relation successfully predicted the observed confinement times on Alcator C such that about 90% of the measurements fell within ±20% of the predicted values. To the extent possible, this scaling was compared with the Alcator C-Mod database. The results of this comparison are shown in Figure 5-3. In general the pre-

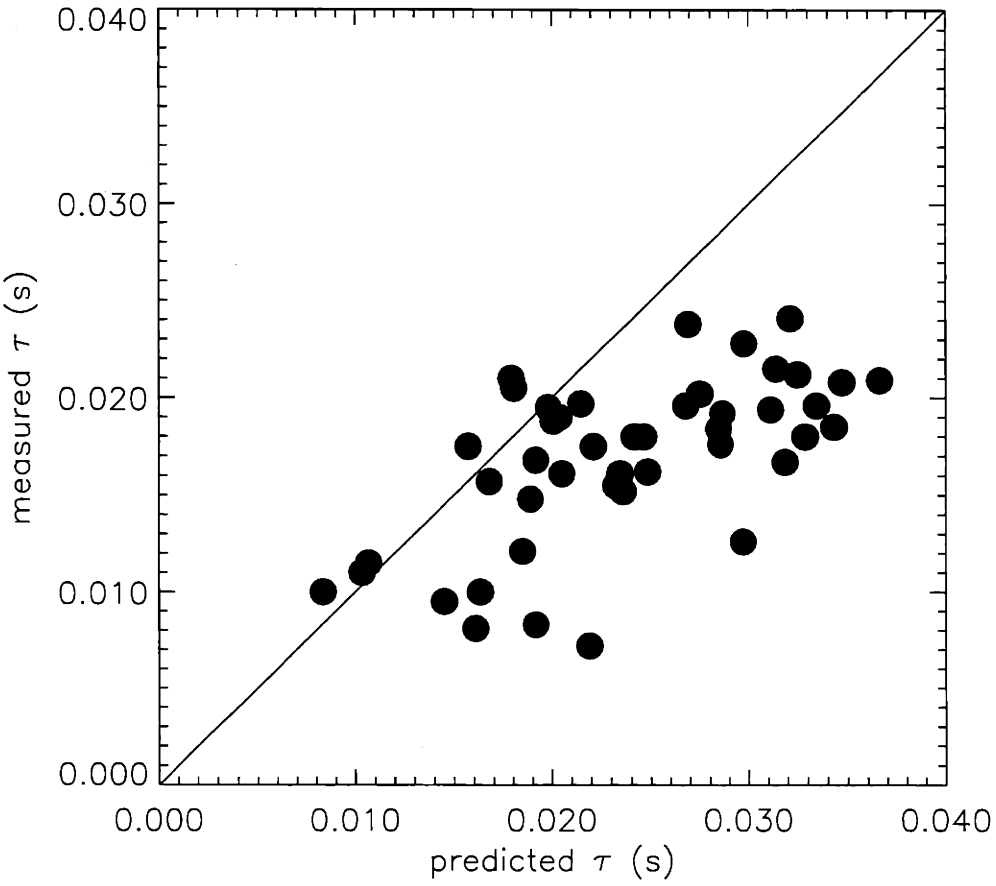

Figure 5-3: Alcator C impurity particle confinement time scaling (equation 5.3) compared with Alcator C-Mod measurements.

dictive ability of the Alcator C scaling is fairly good, although a systematic overestimate of the confinement time is noticed. This predictive ability has been pointed out in comparisons with data taken from other machines as well. Reference [22] has demonstrated that 5.3 is capable of fitting confinement time measurements from machines of greatly different size reasonably well.

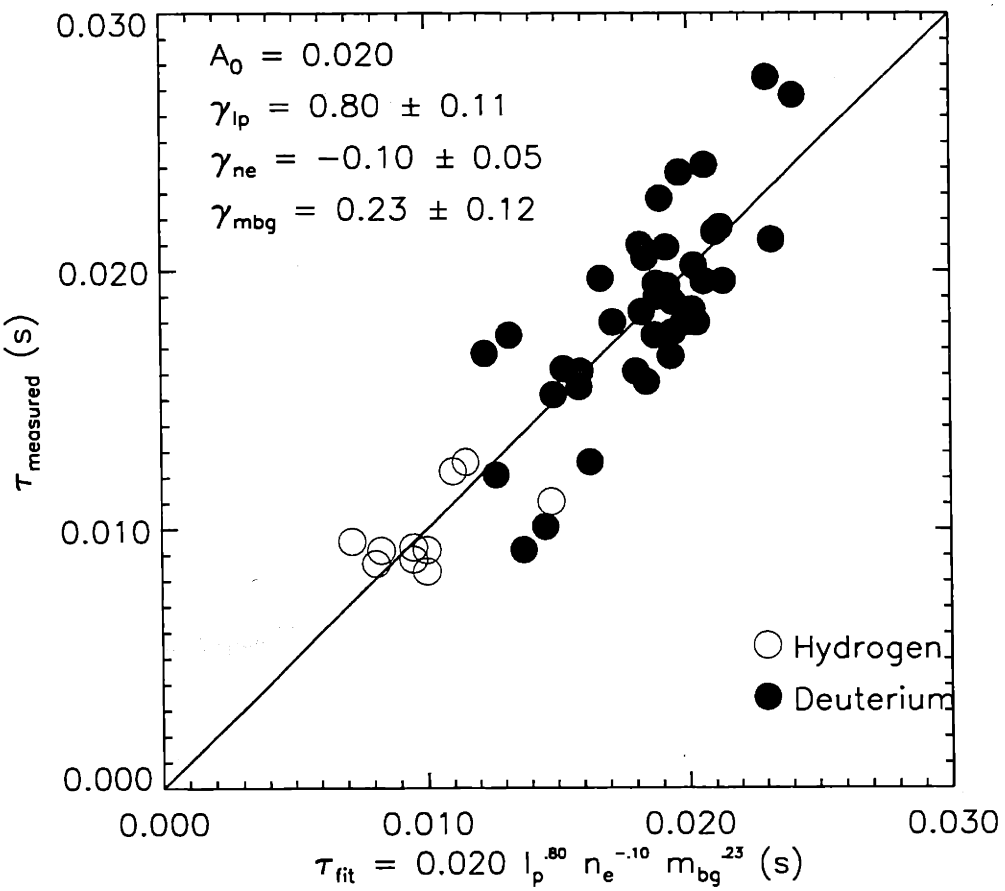

Figure 5-4: Linear logarithmic regression of the impurity particle confinement data showing dependences on plasma current, electron density, and mass of the background gas.

A number of linear logarithmic regressions was performed on the C-Mod injection database. The independent variables used in each regression were chosen from a group which included the plasma current, the mass of the background gas, the line-averaged electron density, Z_{eff}, and the total input power. When all of these variables are included at once, it is clear that colinearities in the data lead to confusion in interpreting the results. For example, since all of the discharges in the database were ohmically heated only, the input power and the plasma current are strongly correlated and lead to confusing results when included with a number of other variables. The results of a regression which includes plasma current, mass of the background gas, and electron density are shown in

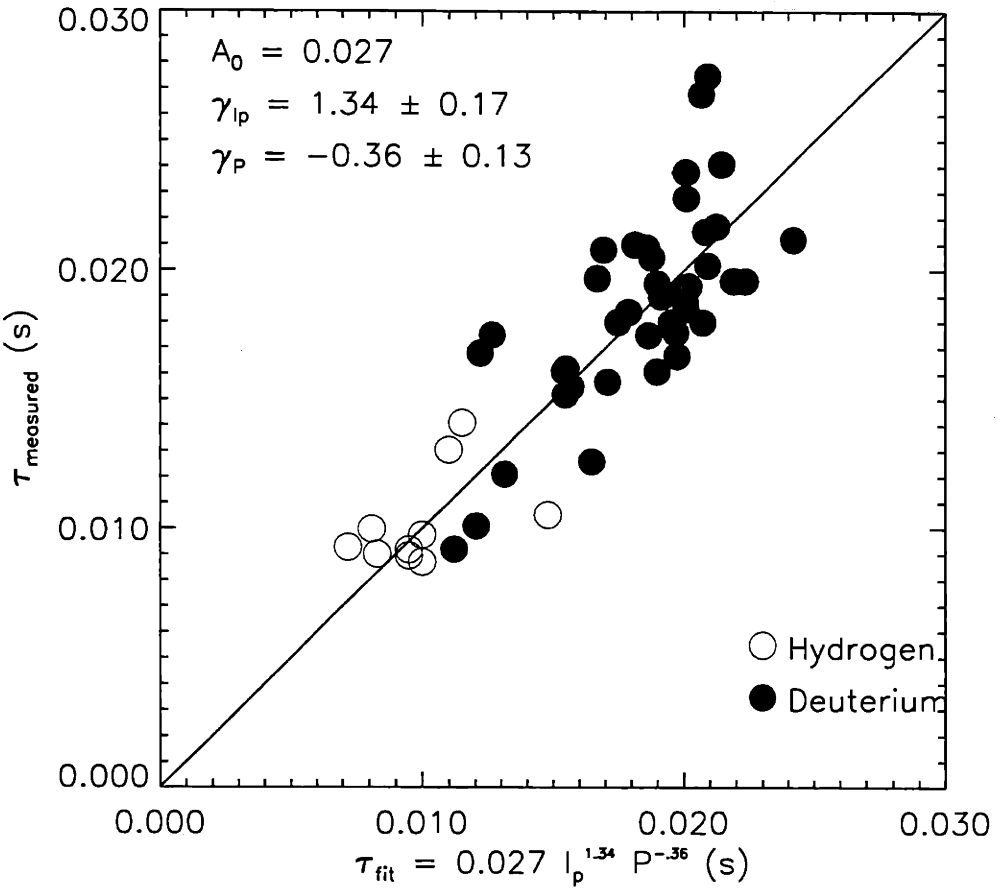

Figure 5-5: Linear logarithmic regression of the impurity particle confinement data showing dependences on plasma current and total input power.

Figure 5-4. The best fit equation determined in this way is:

$$\tau_{fit} = 0.020\overline{n_{e20}}^{-0.1\pm0.05} m_{bg}^{0.23\pm0.12} I_p^{0.80\pm0.11} \tag{5.4}$$

Clearly the most dominant plasma parameter affecting the confinement time in this case is the plasma current. It shows a dependence roughly similar to the linear dependence observed on Alcator C. The results of a regression which includes plasma current and total input power (P_{in}) only are shown in Figure 5-5. The best fit equation determined in this way is :

$$\tau_{fit} = 0.027 I_p^{1.34\pm0.17} P_{in}^{-0.36\pm0.13} \tag{5.5}$$

This result may be significant in that it bears a similarity to the conventionally accepted scaling for the *energy* confinement time known as the ITER-89P scaling [34].

$$\tau_E = 0.048 I_p^{0.85} R^{1.2} a^{0.3} \kappa^{0.5} n_e^{0.1} B^{0.2} m_{bg}^{0.5} P^{-0.5} \tag{5.6}$$

where the plasma current is given in MA, the electron density in units of $10^{20} m^{-3}$, the mass of the background gas in amu, and the total input power in MW. Note that this scaling also shows an almost linear dependence on plasma current and an inverse scaling with the total input power. Other features present in the ITER-89P scaling which have also been observed in the C-Mod impurity particle confinement time scaling are the roughly square root dependence on the mass of the background gas and the very weak dependence on the electron density. The energy confinement time scaling on Alcator C-Mod has also been observed to be in good agreement with the ITER-89P scaling [35].

5.3.1 ICRF Heated Discharges

It has been shown that the addition of auxiliary heating tends to degrade the energy confinement time of the plasma according to the ITER-89P scaling of equation 5.6. Clearly the addition of more power to the plasma has a detrimental effect on the energy confinement time according to this scaling. Using the laser ablation injector, an investigation was made into the effects of ICRF heating on the impurity particle confinement time in Alcator C-Mod. Injections of iron were made into a series of four discharges with identical background plasma parameters ($I_p = 0.8MA, \overline{n_{e20}} = 1.5, T_{e0} = 1.8keV$). Two of the discharges had 0.8 MW of ICRF power injected for a 0.2 second duration while the other two did not. The iron injections were made at the same time in each of the discharges (t=0.55 seconds). The time histories of some key plasma parameters are shown in Figure 5-6. Sufficient ICRF power was injected in these shots to increase the electron temperature by a few hundred eV. The ion temperature was also observed to increase during the ICRF heating. The VUV spectrometer was used to provide high time resolution measurements of the brightness of the 2s-2p line of lithiumlike iron (Fe^{23+}) along a central

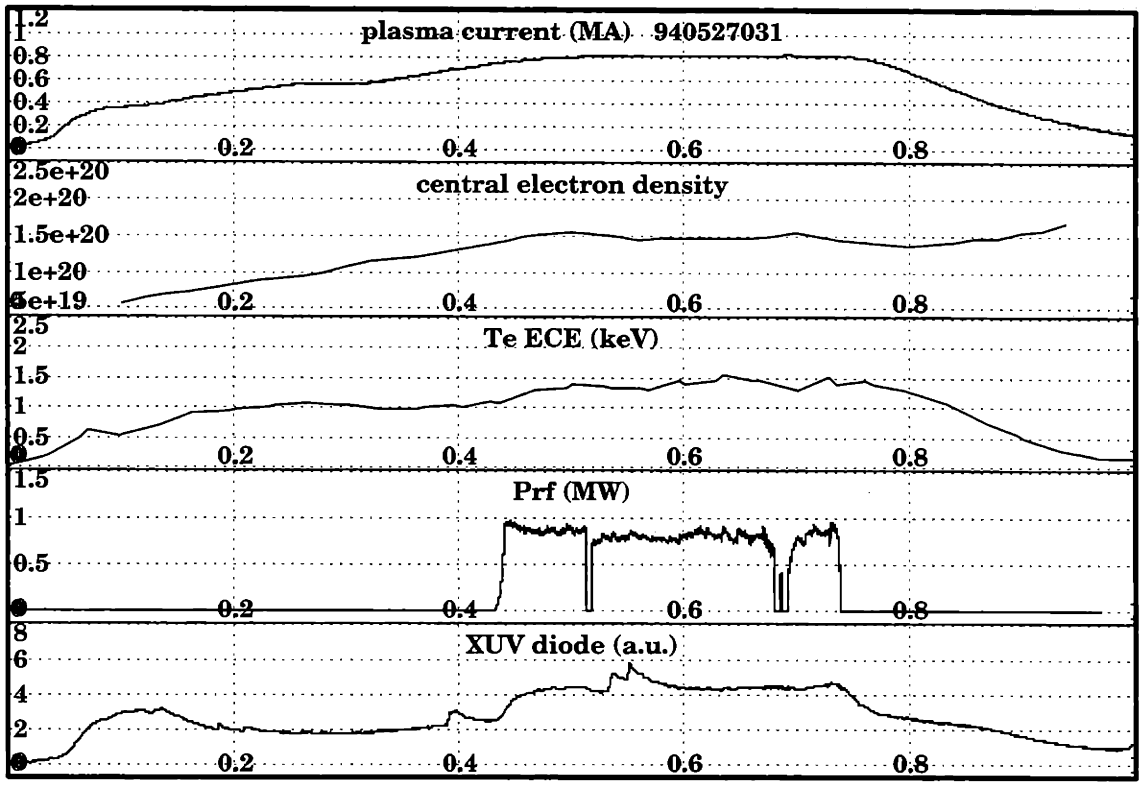

Figure 5-6: Key plasma parameters for the series of injections into RF heated and ohmic discharges. The injection time was 0.55 seconds.

chord during the injection. Both of the lines in the doublet (the j=$\frac{3}{2}$ at 192.0 Å and the j=$\frac{1}{2}$ at 256.0 Å) were observed on successive shots. The time evolution of these lines for all four discharges is shown in Figure 5-7 along with the inferred impurity particle confinement time. The observed confinement times are not demonstrably different during these ICRF discharges. On the basis of this series of injections, therefore, it can be noted that the addition of 0.8 MW of ICRF power which led to some electron and ion heating taking place did not significantly change the impurity particle confinement time in the plasma. The linear regression derived in equation 5.5 would have predicted an expected decrease in the impurity particle confinement time based on the change of total input power of about 15%. This change was not observed. The fact that no high power ICRF discharges are included in the injection database used to derive equation 5.5 may be an explanation for this.

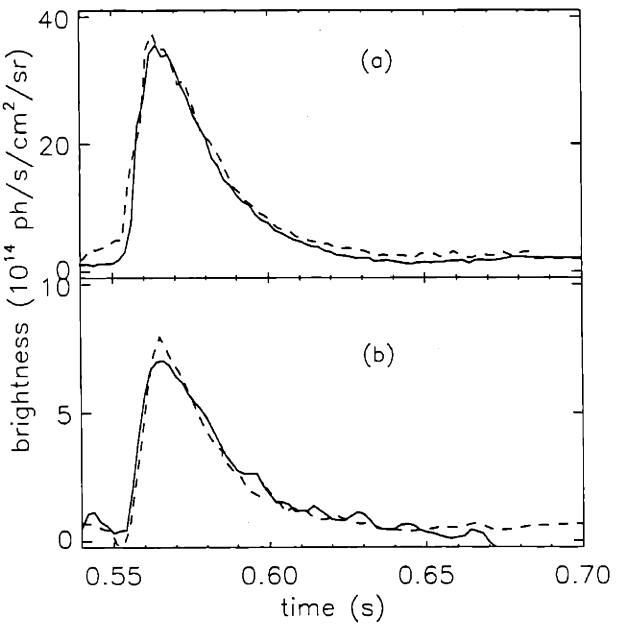

Figure 5-7: Time histories of the 192 Å line (a) and the 255 Å line (b) of lithiumlike iron for the 4 injections into similar RF (dashed line) and ohmic (solid line) discharges.

5.3.2 Divertor Detachment

Another operating regime routinely observed in Alcator C-Mod is divertor detachment [36]. This regime is characterized by a strong decrease in electron temperature at the divertor target plate and observations of loss of conservation of electron pressure along field lines leading to the target. Also observed during divertor detachment is an abrupt increase in central electron density. It is important to determine whether this increase is due to a change in core particle transport or merely a change in fuelling efficiency brought on by changing edge plasma conditions. A series of injections into similar detached and attached divertor discharges was made. The background plasma parameters for these injections were ($I_p = 0.8MA, \overline{n_{e20}} = 1.5, T_{e0} = 1.8keV$). The evolution of these background parameters is shown in Figure 5-8. The injection time is highlighted there as well. The injected impurity in this case was scandium, and the 2s-2p lithiumlike transition

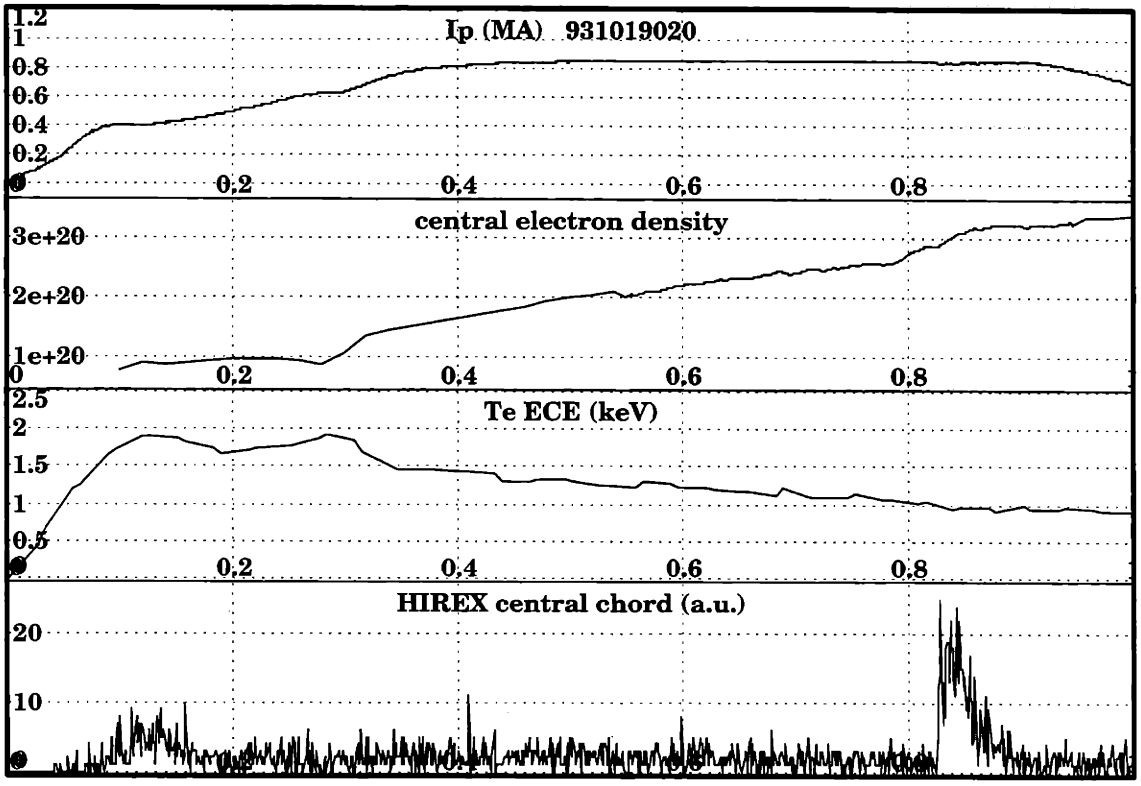

Figure 5-8: Background plasma parameters for scandium injections into detached divertor plasmas. The detachment occurs at time 0.78 seconds. The injection was made at 0.82 seconds.

at 259 Å (Sc^{18+}) was observed with the VUV spectrograph. The confinement time measured during these injections into detached divertor discharges was not significantly different from that measured during ordinary ohmic divertor operation. Furthermore, the x-ray emissivity profiles measured during the injection into the detached divertor discharges did not differ appreciably from those measured without detachment. Their similarity is indicative of the fact that not only did the macroscopic impurity particle confinement time not change, neither did the transport coefficients. These comparisons, therefore, lead one to conclude that there is no change in core impurity particle transport during detached divertor operation. A similar analysis of core electron transport [37] supports this conclusion. Despite the sharp rise in electron density following detachment, electron transport coefficients were not seen to change measurably during detachment. The explanation for the density increase must therefore lie in a change in fuelling efficiency

brought on by the detached condition.

5.4 Transport Coefficients

In addition to measuring impurity particle confinement times, laser ablation injections can also be used to infer impurity transport coefficients. To demonstrate this, consider first a simplified case of transport governed by a single, spatially constant diffusion coefficient without any convection velocity. Although somewhat idealized, this case is representative of anomalous transport with coefficients whose magnitudes are much larger than neoclassical predictions. In such a case, the impurity particle flux is described by:

$$\Gamma_I = -D\nabla n_I \tag{5.7}$$

and the transport equation governing the evolution of a total impurity density n_I is:

$$\frac{\partial n_I}{\partial t} + \nabla \cdot \Gamma_I = 0 \tag{5.8}$$

with the boundary condition that $n_I = 0$ at the edge of the plasma. In a 1-dimensional cylindrical geometry, the spatial solution to this equation is a zeroth order Bessel function and the temporal solution is a decaying exponential with time constant [22]:

$$\tau = \frac{a^2}{2.405^2}\frac{1}{D} \tag{5.9}$$

where 2.405 is identified as the first zero of the zeroth order Bessel function and a is the radius of the cylindrical system. Equation 5.9 relates a diffusion coefficient to a macroscopically observed exponential decay time. If the impurity flux is really as simple as equation 5.7, then this expression for the diffusion coefficient is sufficient and can be computed directly.

A more complete form of the impurity flux, however, includes the effects of a finite convection velocity term as well. This form of the flux can be written as:

$$\Gamma_I = -D\nabla n_I - V n_I \tag{5.10}$$

The simplest form of the convection velocity consistent with the boundary conditions in a cylindrical geometry is:

$$V = \frac{r}{a} V_0 \tag{5.11}$$

where V_0, the value at the edge, is positive for an inward pinch velocity. It then becomes convenient to define a dimensionless parameter which reflects the relative importance of the convective term to the diffusive term:

$$S = \frac{aV_0}{2D} \tag{5.12}$$

It has been shown [38] that, in such a formalism, the exponential decay of the total impurity density is described by an e-folding time of:

$$\tau = \frac{77 + S^2}{56 + S^2} \frac{e^S - S - 1}{4S^2} \frac{1}{D} \tag{5.13}$$

For a given fixed value of the confinement time, τ, increasing values of the dimensionless parameter, S, lead to total impurity density profiles which are more and more peaked. Examples of this are shown in Figure 5-9 where the total impurity density profile as calculated by the MIST code for a scandium injection is plotted for a number of different values of S, all with a fixed exponential decay time of 0.020 seconds. The variation in peakedness ranges from the zeroth order Bessel function (S=0) to highly peaked (S=5). In order to infer the actual peakedness factor observed on Alcator C-Mod during these injections, use was made of the emissivity profiles obtained by both the soft x-ray diode arrays and the bolometer arrays. In particular, the high resolution profiles measured using the soft x-ray diode arrays were particularly useful for this determination. Modelling which takes into account the dominant contributions to the soft x-ray signals was carried out and used to predict an observed profile on the basis of a calculated total impurity density profile obtained from the MIST code. Keeping the impurity particle confinement time fixed to the values measured in the experiment, the values of D and S were varied until a best fit to the observed x-ray emissivity profiles were obtained. The results of this

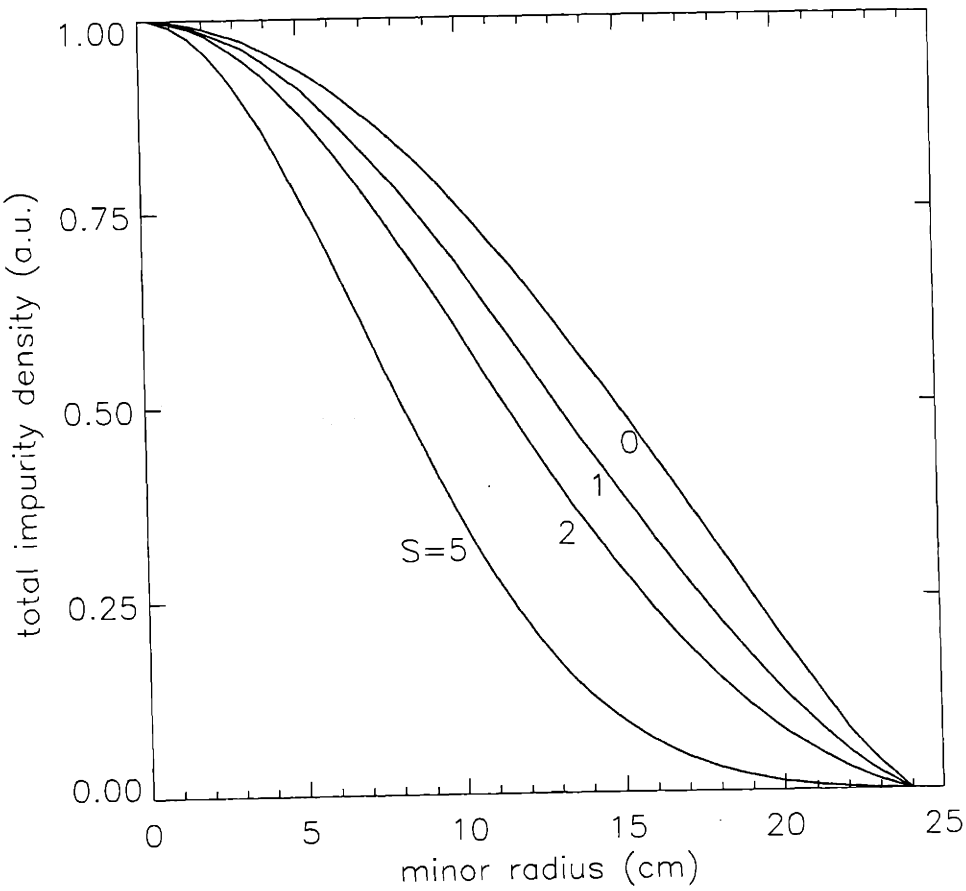

Figure 5-9: Calculated total impurity density profiles using the MIST code for a range of peaking factors, S. The profiles shown are for scandium with an assumed particle confinement time of 0.020 seconds.

iterative process indicate that a peaking factor of about 0.5 provides the best agreement with the observed data.

The modelling used to compare x-ray emissivity profiles was also used to compare directly the observations made with the high resolution x-ray crystal spectrometer array during controlled scandium injections. Shown in Figure 5-10 are the lines of sight of three chords of the HIREX array used for observing these injections. The evolution of a number of lines emitted by the heliumlike charge state of scandium was measured during each injection. A typical spectrum of these lines is shown in Figure 5-11. By modelling

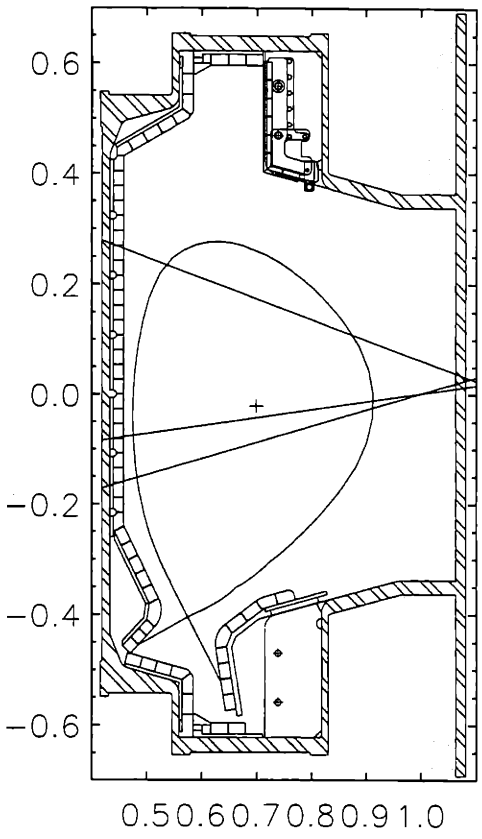

Figure 5-10: Viewing geometry of three chords of the HIREX spectrometer array used for viewing scandium injections.

the emissivity of each of the lines in that spectrum (see Appendix b for details) using time dependent charge state density profiles obtained with the MIST code, the time history of the observed spectrum was predicted. Shown in Figure 5-12 are the observed and predicted time histories of all lines contained in the spectrum shown in Figure 5-11 along the three lines of sight shown in Figure 5-10. For each chord, the code predictions agree well with the observations. Notice in particular the difference in the time for the signals to reach their peak in each case. The chord which has its view closest to the edge of the plasma (c) is actually observed to take the longest time to peak. While it is perhaps not intuitively obvious that this should be so, recall that emission into these lines of the

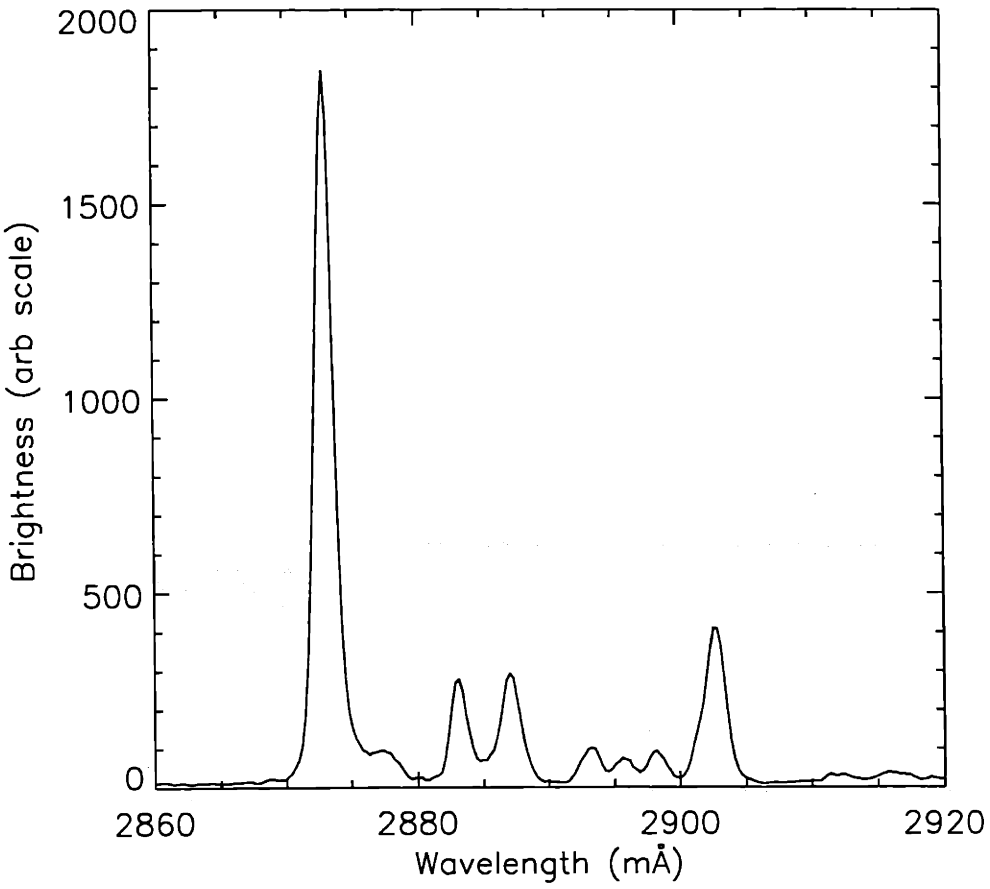

Figure 5-11: Typical heliumlike scandium spectrum obtained during the decay phase of a laser ablation scandium injection. The transitions observed are the same as those observed when viewing the heliumlike argon spectrum. Details of these transitions are found in Appendix B.

spectrum requires that the impurity be ionized to at least the heliumlike state (or the hydrogenlike state for those lines attributable to recombination). The outermost chord in these experiments was looking at a region of the plasma cold enough that impurities diffusing inwards would not yet have been ionized through to the heliumlike state. It is only as those impurities were diffusing from the hotter central region of the plasma that they were sufficiently ionized to produce significant emission in those heliumlike transitions. Since the recombination time of these impurities is long compared with the transport time, the peaking of the outermost chord is delayed relative to the more central

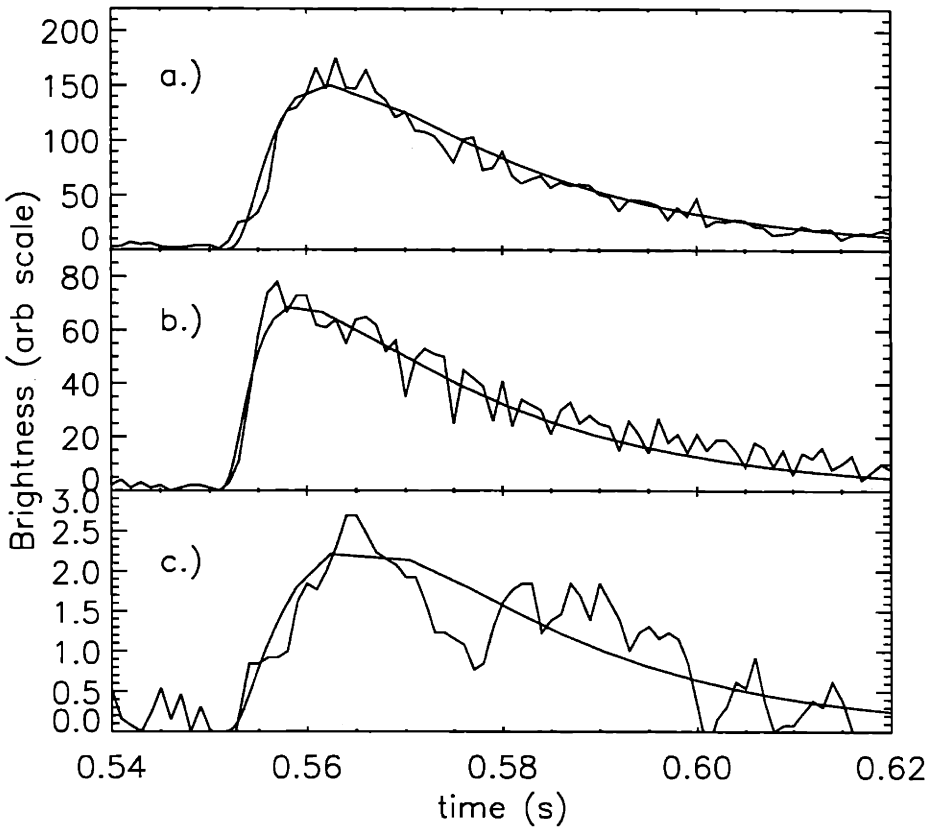

Figure 5-12: Observed time histories and code predictions of the entire spectrum of Figure 5-11 along the lines of sight shown in Figure 5-10. Notice the differences in time-to-peak for each chord.

ones. The significance of the good agreement seen between these observed results and the model predictions is that added confidence is given to the parameters used in the models. Such good agreement would not have been possible for modelled transport coefficients which were very different from the actual coefficients.

5.5 Conclusions

A variety of impurities has been injected into Alcator C-Mod for the purpose of characterizing impurity transport. The impurity particle confinement time has been determined over a wide range of operating parameters and has been found to have a nearly linear dependence on plasma current. An isotopic mass scaling was also observed as was an inverse dependence on total input power. Many of these features are similar, but not identical, to those observed on the Alcator C tokamak.

Investigations of core transport during detached divertor operation have shown that no changes in either confinement time or transport coefficients were observed, lending support to the claim that any macroscopic changes in plasma behaviour following divertor detachment are a result of edge phenomena only. Similar investigations conducted during ICRF heating experiments have shown that no discernable change in impurity particle confinement time was observed. With the addition of increased heating capacity, these investigations can now be extended to an even larger range of operating parameters.

Added confidence in the transport and atomic physics model used for this analysis was given by the good agreement which was found between modelled and observed time histories of laser ablation injections as viewed along a number of differnet spatial chords.

Chapter 6

Intrinsic Impurity Concentrations

6.1 Introduction

The intrinsic impurity level in the plasma is a quantity of great importance to tokamak operation. Intrinsic impurities can have deleterious effects on plasma performance as outlined in the introductory chapter of this thesis. A measurement of the concentration of various impurities and the effects they have on radiative losses from the plasma is therefore desirable. One important impurity in Alcator C-Mod is obviously molybdenum. C-Mod provides a unique opportunity to observe the behaviour of molybdenum as an intrinsic impurity. The typical concentration of molybdenum in the plasma during a variety of discharges was therefore investigated extensively. Another important intrinsic impurity is carbon. Even though there are no actual carbon plasma facing components in C-Mod, small amounts of carbon contamination on the molybdenum tiles from in-vessel activities can prove to be a significant source of plasma contamination. A third impurity which can have important effects on the plasma is argon. While not an intrinsic impurity, argon is routinely injected into the plasma in small amounts in order to allow for the measurement of ion temperatures from the doppler broadening of the heliumlike argon resonance line [39]. The amount of argon injected, while small, can still have noticeable effects on the plasma. Because of this, argon has also been selected a one of the intrinsic

impurities to be analyzed in this chapter.

Intrinsic impurity levels are generally determined by three important factors. One is the strength of the source of the particular impurity species. This source is understood to be the flux of neutral atoms leaving all of the plasma facing components surrounding the plasma. It is fully expected that this source term can change greatly during different types of tokamak discharges, dependent largely on the magnetic geometry, density, and temperature of the plasma in the immediate vicinity of the plasma facing components. A second important factor which determines intrinsic impurity concentrations is the penetration of these source impurities through the edge of the plasma and into the core. For a given source of impurities, it is possible that different plasma conditions will lead to different penetration characteristics. This question of penetration is more thoroughly discussed in Chapter 7. A third factor influencing the impurity concentration in the plasma is the transport in the plasma core. The impurity particle confinement time is the quantity which describes how long an impurity introduced into the plasma remains in the plasma core. As outlined in Chapter 5, this confinement time can vary as a function of various plasma parameters.

To construct an accurate description of intrinsic impurities, measurements from a number of spectroscopic diagnostic systems were used. Line emission was monitored using the VUV spectrometer, the HIREX spectrometer, and the MLM polychromator. Continuum emission attributable to bremsstrahlung was monitored using the multi-chord Z-meter array. The total radiated power emitted by the plasma was monitored with an array of bolometer detectors. The MIST code was used to interpret observed line brightnesses in terms of absolute number density of impurity atoms and their contribution to the total radiated power and the measured Z_{eff}. Consistency among these deduced quantities from all available diagnostics was checked whenever possible.

6.2 Radiated Power

In addition to measuring the concentration of a given impurity in the plasma, it is also important to know what contribution that impurity makes to the total radiated power losses from the plasma. Radiative losses from impurities arise mainly from line radiation, radiative recombination, and enhanced bremsstrahlung. Each of these mechanisms is described briefly below. A description of a key diagnostic used to measure the net effect of these contributions is also presented.

6.2.1 Sources of Radiated Power Losses

Line radiation, radiative recombination, and bremsstrahlung are the dominant mechanisms for radiation loss from tokamak plasmas.

Line radiation losses arise from the sum of contributions from a large number of discrete lines emitted by transitions from each charge state of a given impurity. Each charge state with density n_z can be thought of as radiating photons from electron transitions between levels j and i with power P_{ij} according to:

$$P_{ij} = n_e n_z S_j E_{ij} B_{ij} \tag{6.1}$$

where S_j is the rate coefficient for population of the upper level, j, and E_{ij} is the energy of the photon emitted as the excited electron decays back to its initial state, i. B_{ij} is a branching ratio which accounts for transitions which do not return to the intial state i directly. In tokamak plasmas, the dominant mechanism for populating the upper levels of these transitions is electron impact excitation. This is typically followed by direct and rapid radiative decay to a lower level. In such a case, an appropriate rate coefficient for this process would be used for S_{ij} in equation 6.1. Typical functional forms for electron impact excitation rate coefficients can be found in Appendix B. More elaborate processes for populating and de-populating upper levels may also be taken into account. Calculations which attempt to predict the total radiative losses from all charge states of

a given impurity generally do so by simplifying the complex atomic processes with some sort of an average ion model for the impurity under consideration [40].

While line emission emits photons of discrete energy, radiative recombination results in a continuum of emission. When a free electron is captured into a bound state of an impurity ion, a photon with energy equal to the initial kinetic energy of the electron plus the binding energy of its final state is emitted. The minimum energy available for such a photon is therefore equal to the ionization potential of the capture level of the given ion. The emission continuum can therefore be expected to contain discrete *recombination edges* in the spectrum as a result of this mechanism (see Chapter 8 for an experimentally observed recombination edge in the heliumlike argon spectrum). This contribution to radiated power has a functional dependence on the atomic structure of the particular impurity ion [25]. It is also known that the contribution to total radiated power from radiative recombination is most important at low electron temperatures (low, relative to the ionization potential of the impurity ion).

Bremsstrahlung radiation also results in a continuum of emission as free electrons are accelerated on impurity (and hydrogen) ions. The power spectrum radiated in this way as the result of an impurity of charge Z_I present with a density n_I has a dependence as [41]:

$$\frac{dP}{d\omega} \propto n_e n_I Z_I^2 e^{\left(\frac{-\hbar\omega}{T_e}\right)} T_e^{-\frac{1}{2}} \tag{6.2}$$

This contribution to total radiated power is also straightforward to incorporate into an average-ion model for a given impurity.

6.2.2 Measurement of Total Radiated Power

Total radiated power is measured in Alcator C-Mod using arrays of bolometer detectors. These bolometers are of the conventional gold foil type [42] and are sensitive to photons over a wide range of energies (infra-red to hard x-ray) as well as to particles which are incident on their collection area. These detectors in C-Mod have been arranged to view 24 chords through the plasma at the horizontal midplane. The field of view ranges from

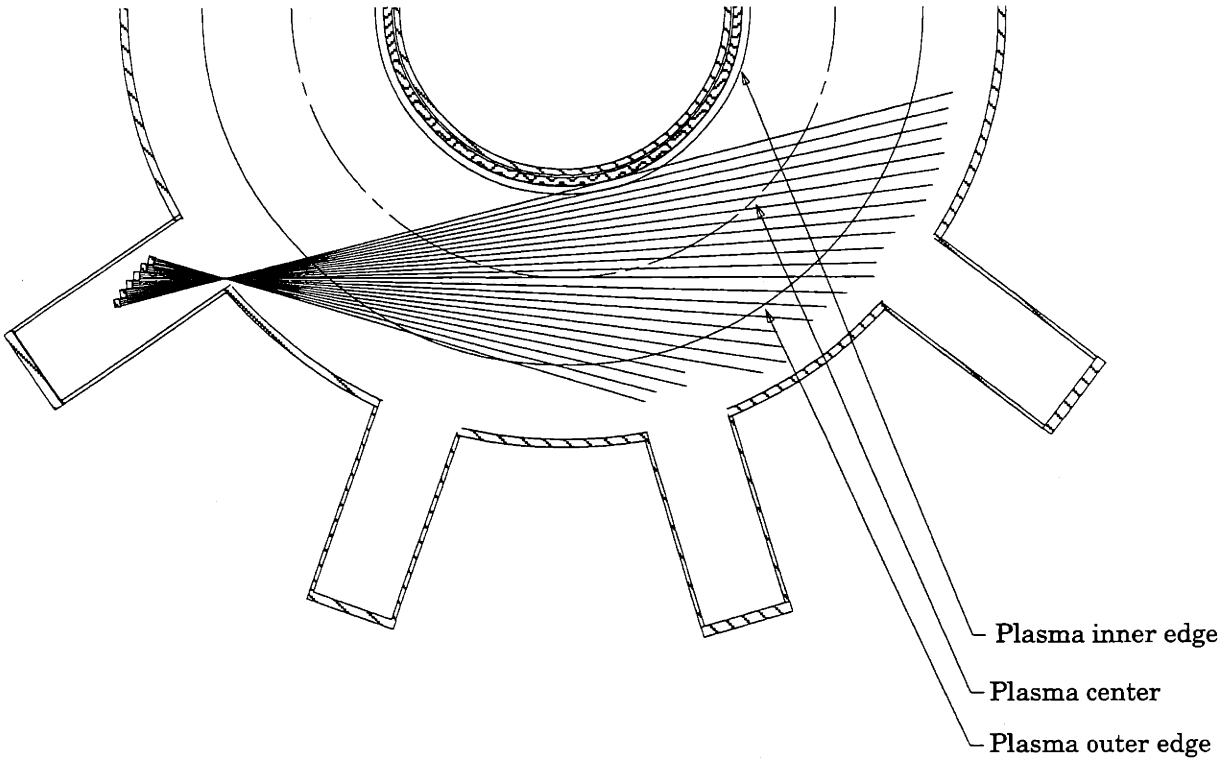

Figure 6-1: Viewing geometry of the 24 chord midplane bolometer array.

chords which are tangent to the inner wall to chords which are tangent to major radii well outside the separatrix of typical plasmas. This viewing geometry is shown in Figure 6-1. Each chord provides an absolutely calibrated line integrated brightness signal with a time resolution of about 10 ms. The calibration was performed by depositing known amounts of energy on the detectors with either a laser pulse or a resistive heating element and measuring the system response. The calibration is accurate to within about ± 15 %.

The brightness profile obtained with this array can be Abel inverted to yield an emissivity profile [43]. A typical brightness profile which includes chords passing through the outer midplane of the plasma and the resulting emissivity profile is shown in Figure 6-2.

There is a number of important features to note in this emissivity profile, which is typical of most obtained during normal plasma operation. The first is that there

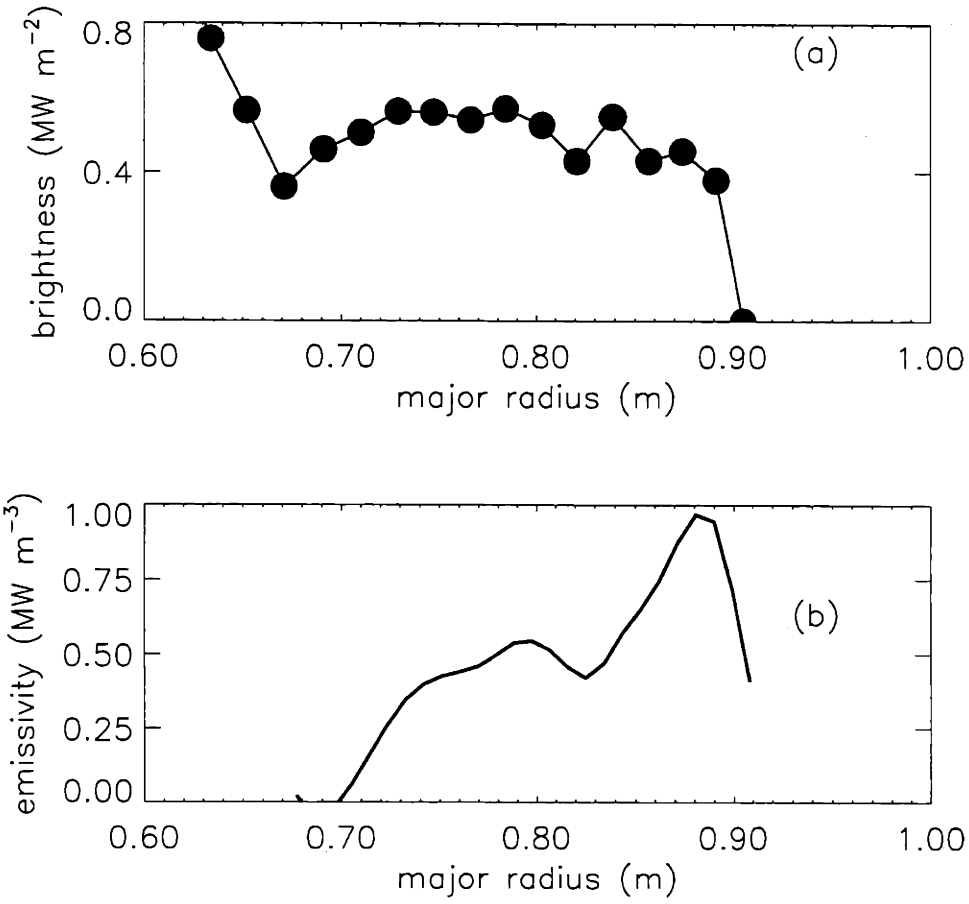

Figure 6-2: Typical brightness profile measured with the 24 chord bolometer array (a), and the emissivity profile obtained after inversion (b) for a plasma centered at 0.68 m with a minor radius of 0.22 m.

are two distinctive local maxima at major radii of around 0.79 m and 0.88 m. The second is that the emissivity profile is definitely not peaked at the magnetic axis. In the course of modelling the total radiated power from the plasma, a consistent explanation of these phenomena must be obtained. In the sections that follow, individual radiated power emissivity profiles modelled for different key intrinsic impurities will be presented and compared with these experimental profiles. Consistency in both the shape of the predicted profiles and their magnitude was investigated.

6.2.3 Modelled Emissivity Profiles

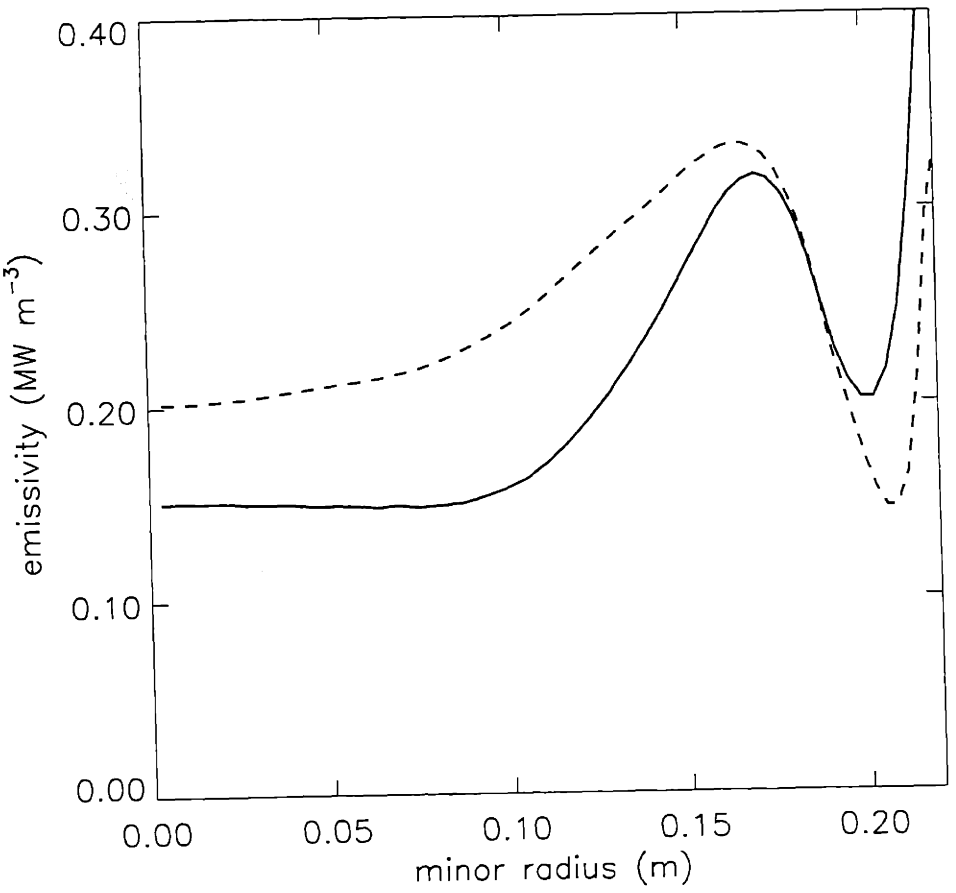

Figure 6-3: A comparison of the radiated power emissivity profiles for the original MIST average-ion model (dashed) and the improved rates model (solid) described in Chapter 4.

The radiated power emissivity profile for a given impurity can be modelled by including contributions from the dominant mechanisms mentioned in Section 6.2.1. This has been incorporated into various applications by Post & Jensen [40] and Hulse (MIST code) [23] on the basis of different assumptions for the impurity charge state distribution. The simplest form of these so-called 'cooling rates' are found in [40] and assume a coronal equilibrium distribution of charges state of the given impurity. The rate of power loss per impurity ion per electron is then available directly from standard curves as functions

of electron temperature. A local emissivity can therefore be produced from these curves with knowledge of the electron density, temperature, and the total local impurity density alone. A more sophisticated treatment of the problem has been incorporated into the MIST code. Rather than assume a coronal distribution of impurity charge states, the distribution is calculated explicitly including all of the effects of transport (see Chapter 5). The dominant radiative loss mechanisms are then calculated on a per-charge-state basis and summed to produce the total emissivity profile for that impurity. This approach is clearly superior in that it accounts for changes in the charge state distribution from coronal equilibrium which are brought about by local transport in the plasma. It has the added advantage of allowing for more flexibility in the atomic physics rates which are used in the calculation. This has already been demonstrated to be extremely important in the case of molybdenum. Shown in Figure 6-3 is a comparison of the modelled radiated power emissivity profile obtained for molybdenum using the Post & Jensen cooling rates and the best available MIST rates with the same total impurity density profile and the same background electron density and temperature profile. The differences are noticeable, particularly in the vicinity of the peak in the profile at a minor radius around 0.16 m. These differences are due largely to the differences in charge state balance used in the two models which result from the changes made to the MIST code as described in Chapter 4. This serves as yet another example of the importance of these modifications. Ongoing modifications to account for different mechanisms which influence the charge state balance in some cases (autoionization, for example) are still being made. Other (especially lower Z) impurities are considered to be well modelled at the present time by the Post & Jensen formalism.

The emissivity profiles measured with the bolometer array can also be used to make estimates of the total radiated power in the main plasma. If the assumption is made that the radiation emissivity in the main plasma is a flux function (i.e. constant on a flux surface), then it is possible to use the magnetic geometry calculated by EFIT to integrate the emissivity profile over the plasma volume. The value obtained by this integration

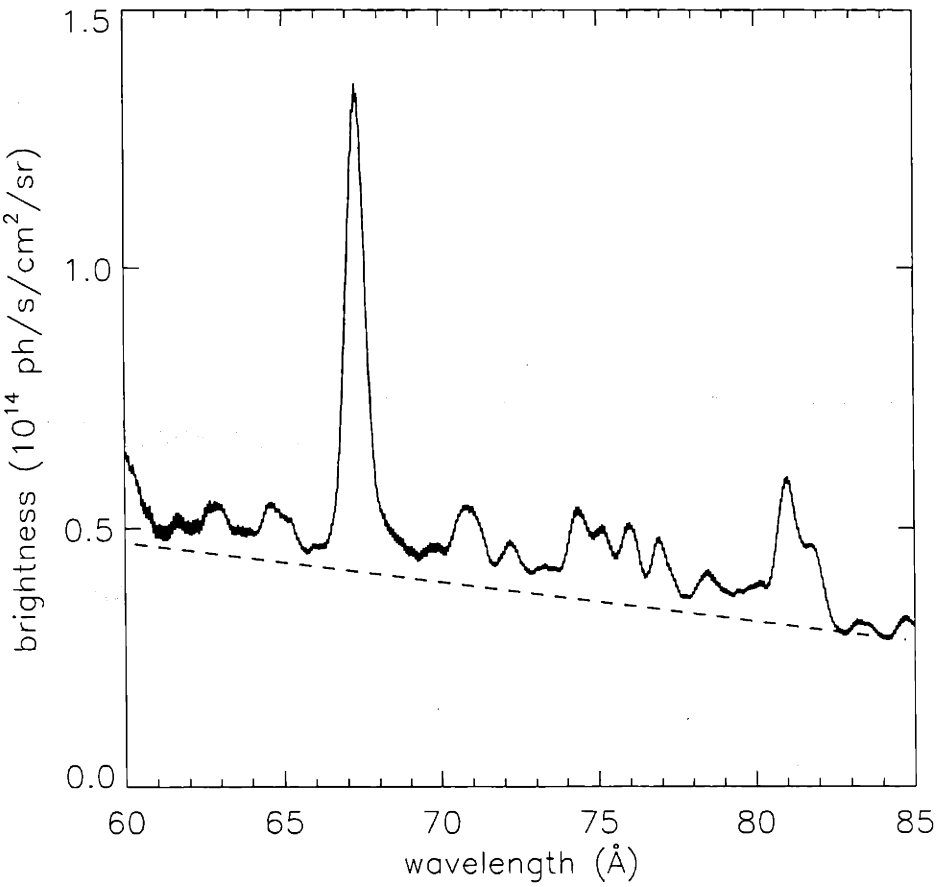

Figure 6-4: Spectrum taken with the VUV spectrometer showing the 1s-2p carbon line in second order at 67.4 Å. Also shown is the typical background level which is subtracted away to give the true brightness of the carbon line.

is the total radiative loss from the main plasma excluding the divertor region and the scape-off layer.

Modelling of the plasma impurities was carried out to try and reach consistent agreement with the measurements made using the bolometer array. Specifically, independent spectroscopic determination of the concentrations of various major plasma impurities was used to predict both the radiation emissivity profiles due to each impurity element as well as its individual contribution to the total radiated power. The impurities considered for this analysis were molybdenum, carbon, and argon.

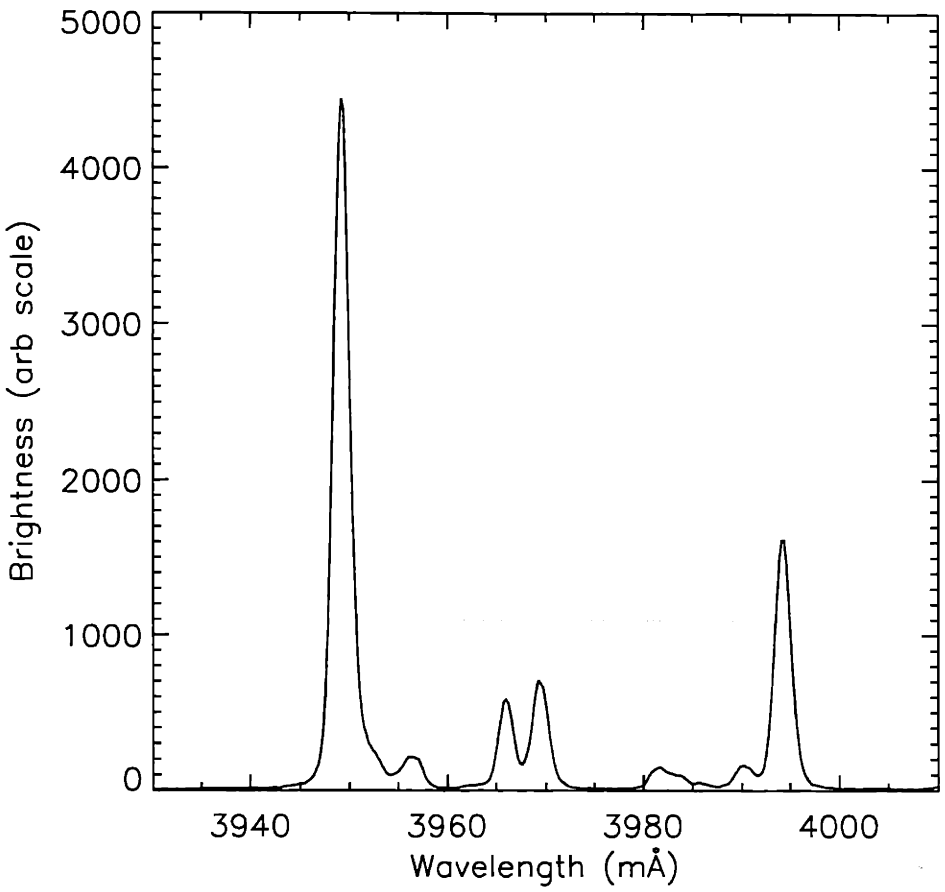

Figure 6-5: Spectrum taken with the HIREX spectrometer showing the $1s^2$-1s2p argon line at 3949.2 mÅ.

The first important quantity which was determined was the concentration of each of these impurities in the plasma. For each impurity, there exist certain lines which were considered most convenient for this determination, either because of their brightness, charge state, or because of the ease with which they could be viewed by a particular diagnostic. The lines which were selected are listed in Table 6.1 along with the instrument with which they were observed. Typical spectra which show the carbon and argon lines as well as the spectral region observed by the MLM polychromator during these experiments are depicted in Figures 3-13, 6-4, and 6-5. Also shown in these figures is the typical background continuum signal level which is subtracted away from each spectrum before

element	charge state	transition	wavelength (Å)	instrument
molybdenum	31+	$3s^2$-3s3p	127.8	MLM polychromator
carbon	5+	1s-2p	33.7	VUV spectrometer
argon	16+	$1s^2$-1s2p	3.949	HIREX spectrometer

Table 6.1: Transitions used for the determination of intrinsic impurity concentrations.

actual line brightnesses are calculated. In the case of the HIREX signals, this continuum is always essentially zero. For the VUV spectrometer, the background signal level varies as a function of wavelength (see Chapter 3).

The results of observations based on the lines specified here for different ohmic and ICRF heated discharges are presented in the following two sections.

6.3 Ohmic Discharges

During normal ohmic operation, spectra are routinely obtained with the VUV spectrometer which allow for the simultaneous measurement of many impurity lines. Regions of the spectrum important for the measurement of intrinsic impurities are the region around 115-130 Å in which are included many strong lines from central charge states of molybdenum (Mo29+ to Mo31+), and the region around 60-90 Å in which are included high charge state lines from carbon and oxygen along with a large number of intermediate charge state lines of molybdenum. Simultaneous measurement of both these regions is not possible with the VUV spectrometer alone, but shot-to-shot measurements are made routinely during repeatable discharge operation. In addition, the MLM polychromator is used to monitor the 128 Å region of the spectrum. The cross calibration discussed in Chapter 3 allows this instrument to be used with a high degree of confidence for absolute measurements of known lines at these wavelengths.

Discharges heated exclusively with ohmic power were the most common type of discharge run in Alcator C-Mod during its first two major operational campaigns. Data from a wide range of operational parameters are therefore available for this type of discharge. Plasma currents have been obtained in the range of 0.4-1.0 MA with line averaged

electron densities ranging from 0.5-2.5 $\times 10^{20}\, m^{-3}$ and central electron temperatures from 1.0-2.2 keV in both limited and diverted magnetic geometries. As an overview of findings made during ohmic operation, presented in this section are scalings of important impurity-related quantities such as total radiated power and Z_{eff} with plasma density for similar diverted plasmas. A comparison of these findings with observations made during limited discharge operation is presented in the following section.

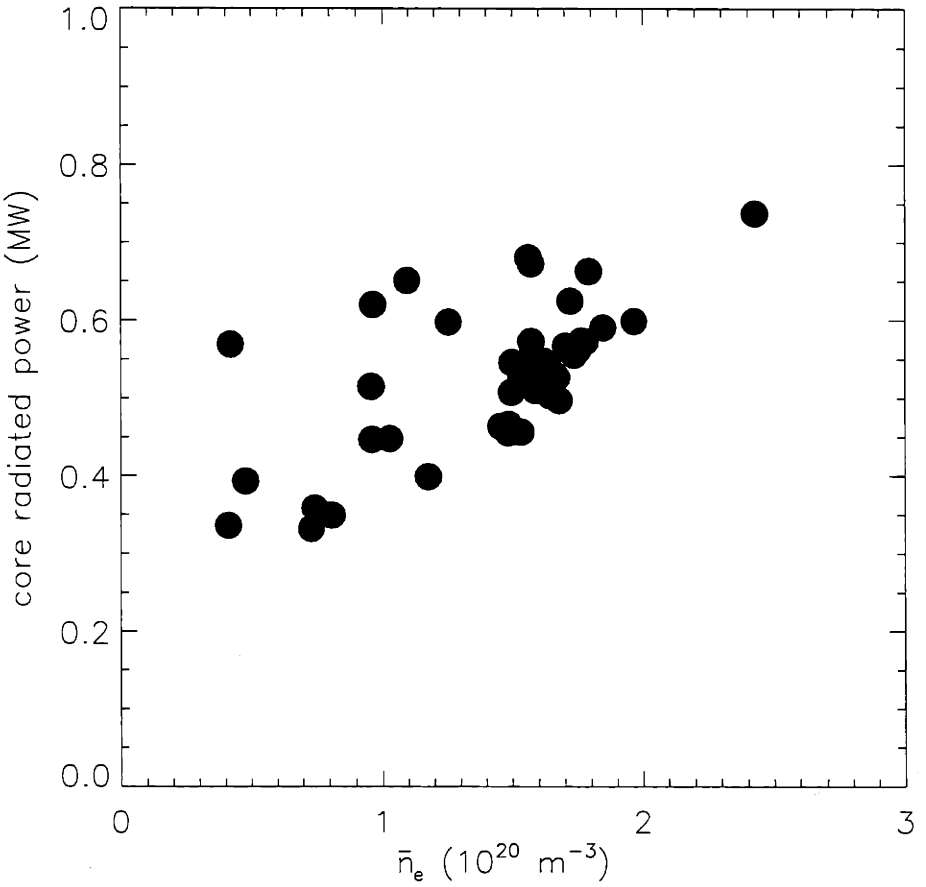

Figure 6-6: Total radiated power from the main plasma as measured by the midplane bolometer array over a range of electron densities showing a roughly linear dependence.

Shown in Figures 6-6 and 6-7 are the total radiated power and the Z_{eff} of typical diverted plasmas over a range of density. The trend displayed by each of these figures gives insight into the levels of contamination of the plasma by impurities over the density range

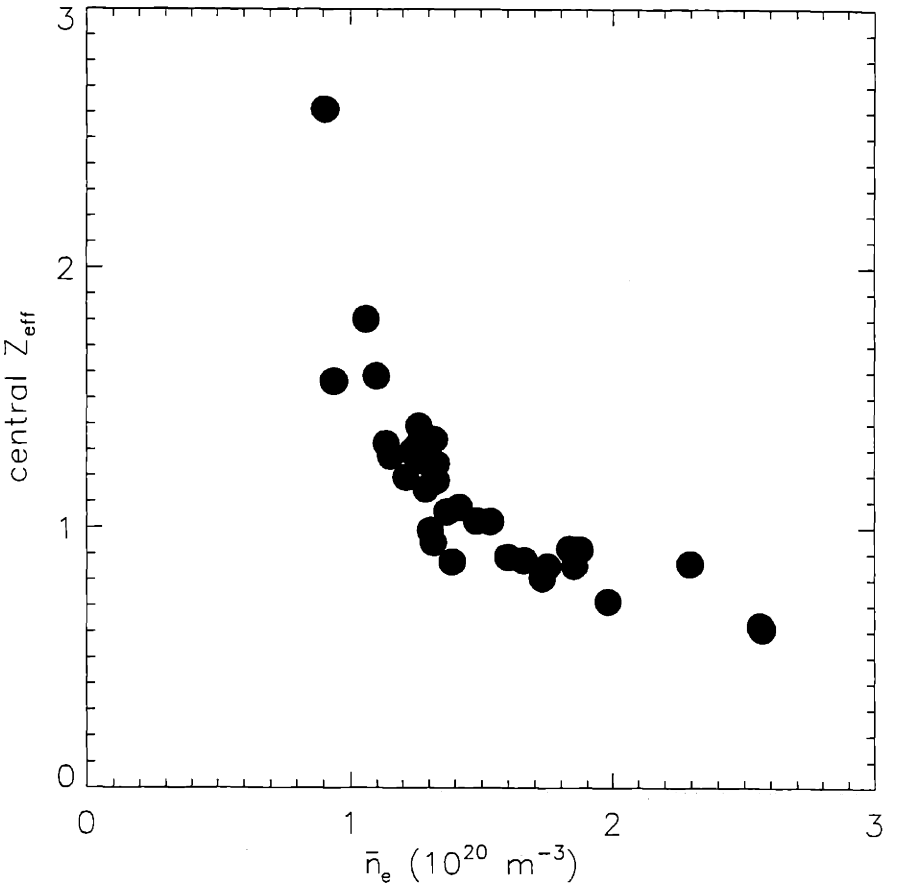

Figure 6-7: Z_{eff} at the center of the plasma as measured by the visible bremsstrahlung array over a range of electron densities showing a roughly inverse dependence. (See Chapter 1 for details on why Z_{eff} measured in this way sometimes falls below unity.)

available in these experiments. The total radiated power can be seen to have an almost linear dependence on the line-averaged density of the plasma. Recall that, in general, $P_{rad} \propto n_e n_I$. If the number of impurities in the plasma can be expressed as some fractional concentration of the electron density, $f_I = \frac{n_I}{n_e}$, then, for a fixed fractional concentration, the radiated power would be expected to depend on the electron density squared. In that this effect is not observed, it can be argued that the concentration of impurities is decreasing as the electron density is increased. This finding is also borne out by the trend in the measured Z_{eff} data. As (Z_{eff}-1)$\propto f_I(Z)(Z-1)$, for some average f_I and Z based

on all impurity species present, this provides rather direct evidence that this fractional concentration of impurities is dropping as the electron density is increased. In fact, the evidence from both measurements presented here shows that the dependence is roughly $f_I \propto \frac{1}{n_e}$. Insofar as the increase in electron density tends to decrease the edge electron temperature which is the dominant factor in defining the sputtering rate of impurities from the plasma facing components, this trend is understandable. In addition, since a higher edge electron density would tend to ionize a given source of impurities outside the last closed flux surface at a higher rate than would a lower density (see Chapter 7 for more details about this screening mechanism), the behaviours observed in the P_{rad} and Z_{eff} data are consistent. Over the density range included in this investigation, the implied reduction in the impurity concentration is more than a factor of ten. A more quantitative analysis which verifies this effect is presented in the next section.

The dominant impurities monitored during ohmic operation include molybdenum and carbon. They are thought to be the two largest contributors to the total radiated power in the main plasma. The direct contribution due to argon radiation is found to be small for the trace injections used for ion temperature measurements. The indirect effects of increased sputtering are accounted for through observations of the other intrinsic impurities. Using the analysis method discussed in Chapter 4, estimates of the fractional concentration of each dominant impurity can be made for any particular discharge. From this fractional concentration, estimates of the contribution each impurity makes to the total radiated power in the plasma can also be made. As a check on the validity of these estimates, comparisons between the predicted radiated power emissivity profiles and those measured with the bolometer array were made. Shown in Figure 6-8 is an experimentally measured emissivity profile from a moderate density ($\overline{n}_e = 1.3 \times 10^{20} m^{-3}$) based on the inversion of bolometer brightness measurements. Also shown are the profiles predicted by the MIST code for molybdenum and carbon. The magnitude of these predicted profiles has been adjusted to be consistent with fractional concentrations for each impurity calculated on the basis of spectroscopic measurements of the sodiumlike

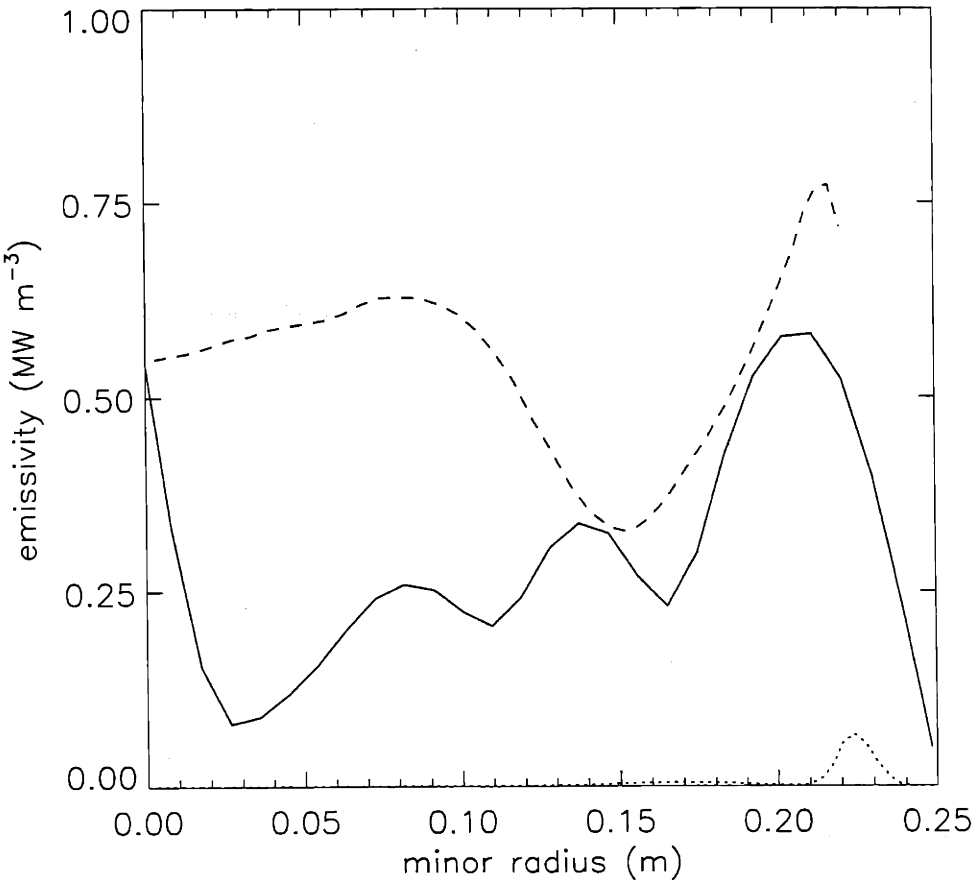

Figure 6-8: Measured radiated power emissivity profile for a moderate density diverted discharge (solid). Also shown are predicted profiles for molybdenum (dashed) and carbon (dotted).

molybdenum and the Lyman-α carbon lines respectively. Qualitatively, the predictions show local maxima at radii which agree well with the measured profile. Quantitatively, the predicted profile is able to determine a total radiated power which only overestimates by about 30% the power measured with the bolometers. This type of good agreement is typical for discharges with low to moderate densities. At higher electron densities (more specifically, at lower electron temperatures) the model for molybdenum is less effective at predicting the total radiated power. In most high density cases, the model greatly overpredicts the molybdenum contribution to total radiated power. This points

density regime	$\overline{n_e}(10^{20}m^{-3})$	T_{e0} (keV)
low	0.8	2.0
moderate	1.3	1.7
high	2.2	1.4

Table 6.2: Plasma parameters used for experiments to compare intrinsic impurity concentrations during limited and diverted operation. The plasma current for all discharges was 0.8 MA.

to inadequacies in the way this contribution to total radiated power is handled for the intermediate charge states of molybdenum in particular. Work is ongoing via the LLNL collaboration to improve this model.

6.3.1 Comparison of Diverted and Limited Operation

To answer one of the key questions regarding the efficacy of diverted operation, a series of experiments was performed to compare impurity levels in similar limited and diverted discharges. Plasmas carrying 0.8 MA of current were established in both limited and diverted configurations over a range of densities. The important plasma parameters for each of the discharges used in this experiment are listed in Table 6.2. A number of limited and diverted shots was run in each of the density regimes listed. The magnetic geometry for each configuration is shown in Figure 6-9. The important intrinsic impurities discussed above were monitored in each case along with the total radiated power and the Z_{eff} of the plasma. The results of these experiments are summarized and discussed below.

Figure 6-10 shows the Z_{eff} of the plasmas for all the discharges used in this experiment. As has already been noted, there is a typical inverse relationship between Z_{eff} and the plasma electron density. This trend is also well demonstrated in the data presented here. For both the limited and the diverted discharges, Z_{eff} is seen to fall strongly as the line-averaged density increases. A direct comparison, however, shows that at low and moderate densities, Z_{eff} is also clearly lower for the diverted discharges than it is for the limited discharges. This difference is more pronounced at lower density than it

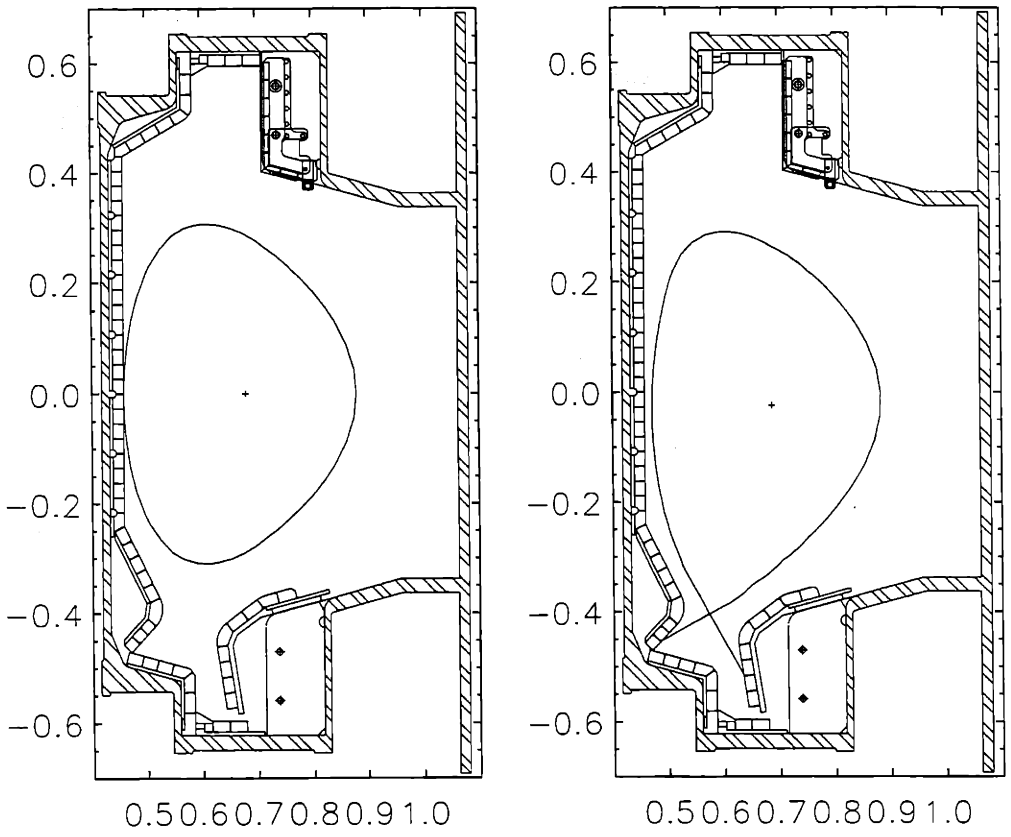

Figure 6-9: Magnetic geometry for the limited (a) and diverted (b) discharges used in these experiments.

is at higher density, but is nonetheless present there as well. In terms of the overall impurity content in these plasmas as is indicated by the quantity Z_{eff}-1, the low density limited plasmas are clearly highly contaminated with impurities. This is consistent with results obtained previously on limited machines with metal walls such as Alcator A and C [44]. It is encouraging, however, to see that this level of contamination for limited plasmas only exists at low to moderate density. At the highest densities investigated in these experiments, the Z_{eff} during limited operation was almost as low as that seen during diverted operation at those densities (recall the caveats to Z_{eff} falling below 1.0 discussed in Chapter 3).

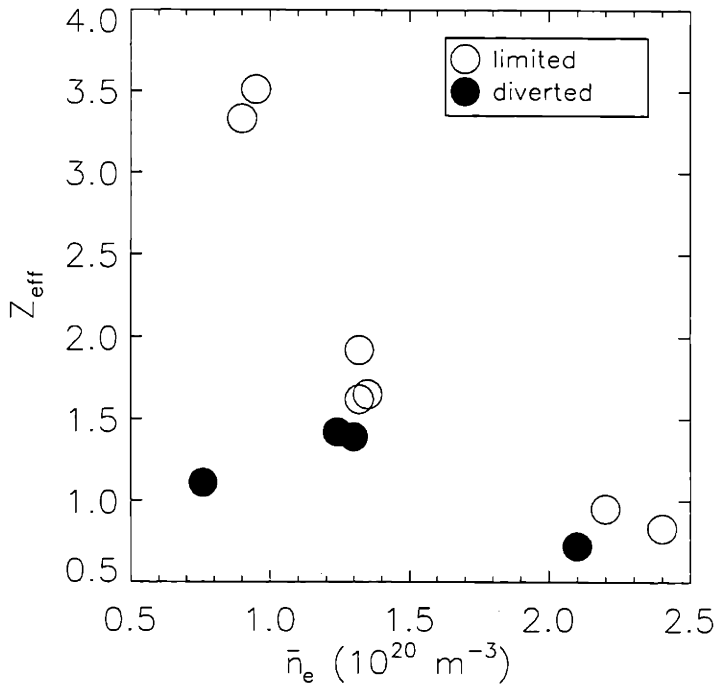

Figure 6-10: Comparison of measured Z_{eff} for limited and diverted discharges over a range of densities.

Additional evidence which demonstrates that the limited discharges are more highly contaminated with impurities can be found by examining the radiated power coming from the main plasma during these discharges. Shown in Figure 6-11 is the total radiated power from the main plasma as measured with the midplane bolometer array as a function of the line averaged electron density in the three regimes investigated for both the limited and the diverted discharges. Again the difference between the limited and the diverted shots is readily apparent, especially at low and moderate density, where the total radiated power is observed to be at least a factor of two higher for the limited shots. At high density, this difference is not as large, consistent with the convergence of Z_{eff} in that density regime as well. Note also that the total radiated power for the diverted discharges tends to rise steadily with increasing electron density. This, of course, is more evidence of the general trend of a linear dependence of radiated power on density that has been

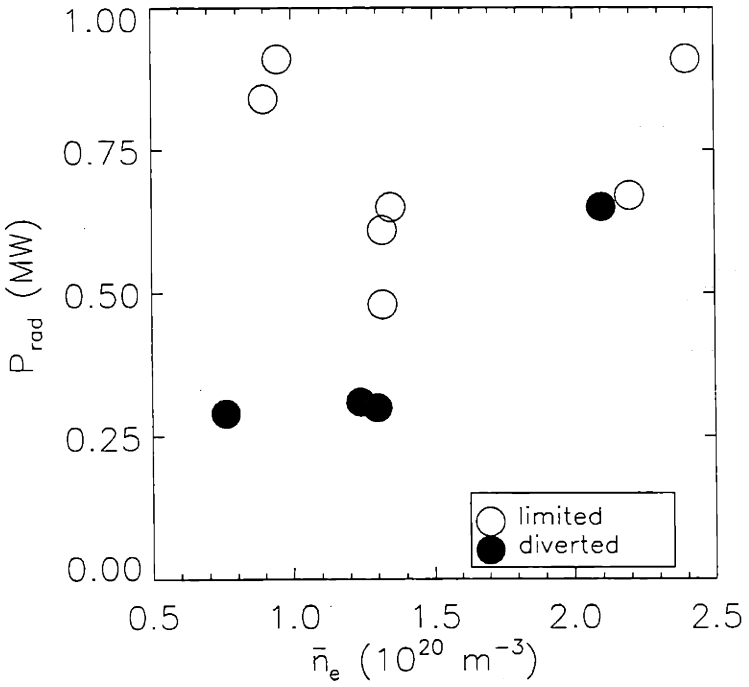

Figure 6-11: Comparison of measured total core radiated power for limited and diverted discharges over a range of densities.

observed in C-Mod during diverted discharge operation. It is indicative of an impurity concentration which varies inversely as the electron density.

More specific spectroscopic data also exist which serve to verify these findings. Shown in Figure 6-12 are the brightnesses of the sodiumlike molybdenum line observed by the MLM polychromator for the discharges in question. In Figure 6-13 are shown the brightnesses of the carbon Lyman-α line observed by the VUV spectrometer for those same discharges. Again the differences between the limited and the diverted discharges are readily apparent in all density regimes. For molybdenum, the difference in brightness between the limited low density and high density case is as large as a factor of ten. The change in the diverted shots over that density range in not nearly as dramatic, probably owing to the fact that the molybdenum concentration was very low to begin with. For the low and moderate density regimes, the difference in brightness between the limited

quantity	geometry	low	moderate	high
fractional concentration	lim	10	3.6	4.6
(10^{-4})	div	0.92	1.9	1.4
total number of atoms	lim	7.9	4.0	8.2
(10^{16})	div	0.55	1.9	2.3
contribution to P_{rad}	lim	1.3	1.0	4.6
(MW)	div	0.08	0.45	1.1
contribution to Z_{eff}	lim	1.0	0.35	0.45
	div	0.09	0.19	0.14

Table 6.3: Effects of molybdenum in limited and diverted shots over a range of densities as calculated by the model.

quantity	geometry	low	moderate	high
fractional concentration	lim	280	120	55
(10^{-4})	div	86	45	25
total number of atoms	lim	210	130	99
(10^{16})	div	52	44	41
contribution to P_{rad}	lim	0.13	0.09	0.10
(MW)	div	0.03	0.03	0.04
contribution to Z_{eff}	lim	0.84	0.35	0.17
	div	0.26	0.13	0.08

Table 6.4: Effects of carbon in limited and diverted shots over a range of densities as calculated by the model.

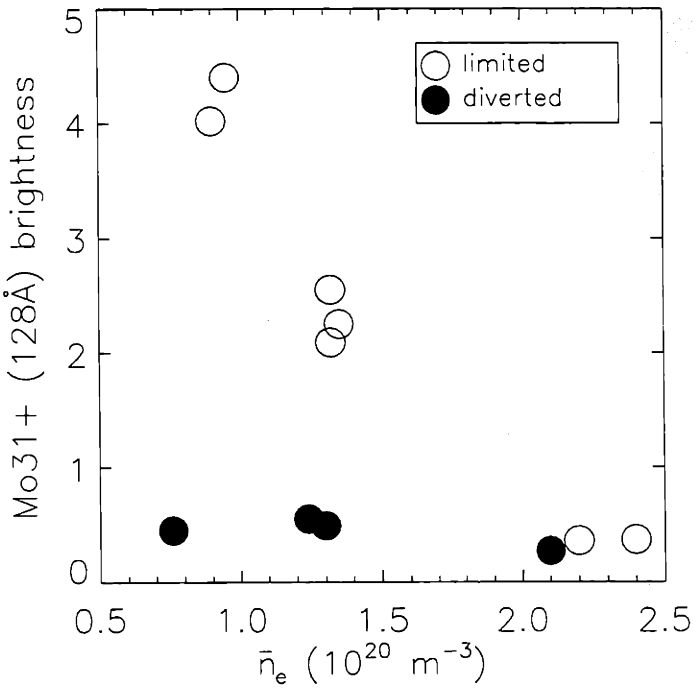

Figure 6-12: Comparison of observed Mo 31+ brightness along a central chord for limited and diverted discharges over a range of densities. Units are 10^{14} ph/s/cm^2/sr.

and diverted cases is at least a factor of five to ten. The difference at high density is not large, again consistent with the convergence of the Z_{eff} and the radiated power measurements. The carbon behaviour, on the other hand, is qualitatively very different. The diverted discharges show the carbon brightness rising steadily as a function of density. The limited discharges show an initial decrease on transition from the low to the moderate density regime, followed by an increase in the high density regime. This trend is also mimicked somewhat in the radiated power trend for the limited discharges. Rather than draw conclusions on the basis of these brightness measurements alone, analysis was performed to convert the brightnesses to actual impurity densities in the plasma according to the methods outlined in Chapter 4. An average of the results from discharges in each density regime was chosen for both the diverted and limited case. Calculated quantities included the fractional concentration of each impurity in the plasma, the total number of

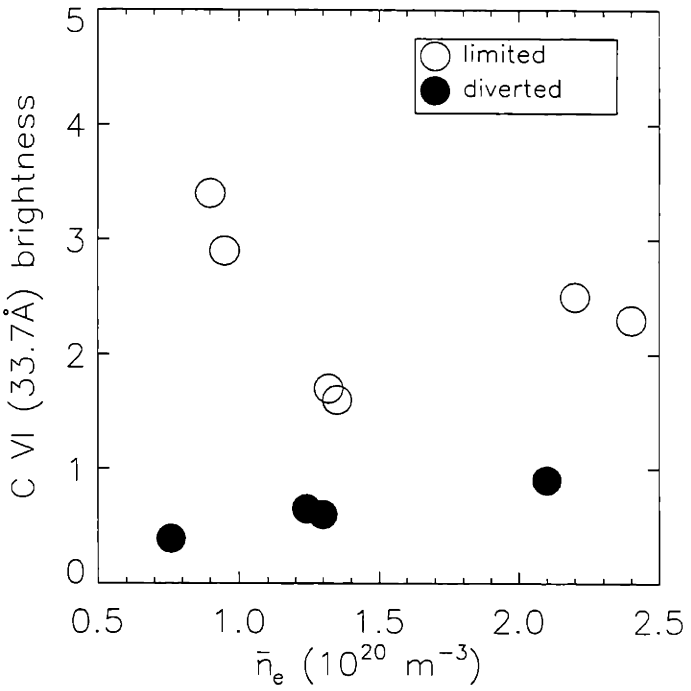

Figure 6-13: Comparison of observed C VI brightness along a central chord for limited and diverted discharges over a range of densities. Units are 10^{14} ph/s/cm^2/sr.

impurity atoms in the plasma, the contribution to the total core radiated power, and the contribution to Z_{eff}. These results are summarized in Tables 6.3 and 6.4. The quantities which can be compared with measured results (Z_{eff} and P_{rad}) agree well for most of the low and moderate density cases. The totals predicted by the carbon and molybdenum contributions are consistent with those observed. For the high density case, a strong discrepancy is noticed in the prediction of total molybdenum radiated power for the limited discharge case. This is related to inaccuracies in the model discussed earlier which become pronounced at lower electron temperatures. The effects of these inaccuracies are mitigated somewhat at higher electron temperatures due to the inclusion of higher charge states of molybdenum which are believed to be better modelled, thereby making the low and moderate density cases more reliable.

6.4 ICRF Heated Discharges

Alcator C-Mod has operated during the 1993, 1994, and 1995 campaigns with the capability of injecting up to 3.5 MW of ICRF heating power at 80 MHz using either a monopole or a dipole antenna configuration. The 1993 campaign saw one monopole antenna on a movable stage to allow it to be set at different major radii installed and operational. The 1994 and 1995 campaigns saw two fixed dipole antennas installed and operational. A discussion of the design and operational differences between these antennas can be found in [45]. Generally, though, the differences lie in the way the 80 MHz current is driven in the current straps of each antenna. In the case of the monopole, there exists only one current strap (hence this antenna is sometimes referred to as a 'single-strap'), whereas in the dipole case, there exist two current straps which can be driven with a variable relative phase shift. Operationally, these differences are thought to produce very different plasma sheaths on the surface of the antennas and in the vicinity of other plasma facing components. Differences such as this will be kept in mind when trying to account for observed differences in plasma behaviour using the two antenna. Another design difference between the monopole and dipole antennas is in the materials used to coat the Faraday shield in each case. The Faraday shield serves as an electrostatic screen which is responsible for shorting out the toroidal component of the electric field generated by the antenna. This is done to avoid exciting undesirable waves components in the plasma edge which could lead to greatly enhanced sputtering and impurity production from the antenna itself as has been demonstrated in the past [46]. The shield itself consists of a conducting cover over the current strap with slots running in the direction of the main toroidal field in order to allow the field induced by the current strap to penetrate through to the plasma. The single strap antenna was outfitted with a Faraday shield coated with titanium carbide (TiC). One of the two strap antenna shields was also coated with TiC while the second two strap shield was coated with boron carbide (B_4C). Typical ICRF heating pulses lasted up to several hundred milliseconds at powers ranging from 0.1-3.5 MW (0.1-1.0 MW for the single strap). This variation allowed for a thorough set of

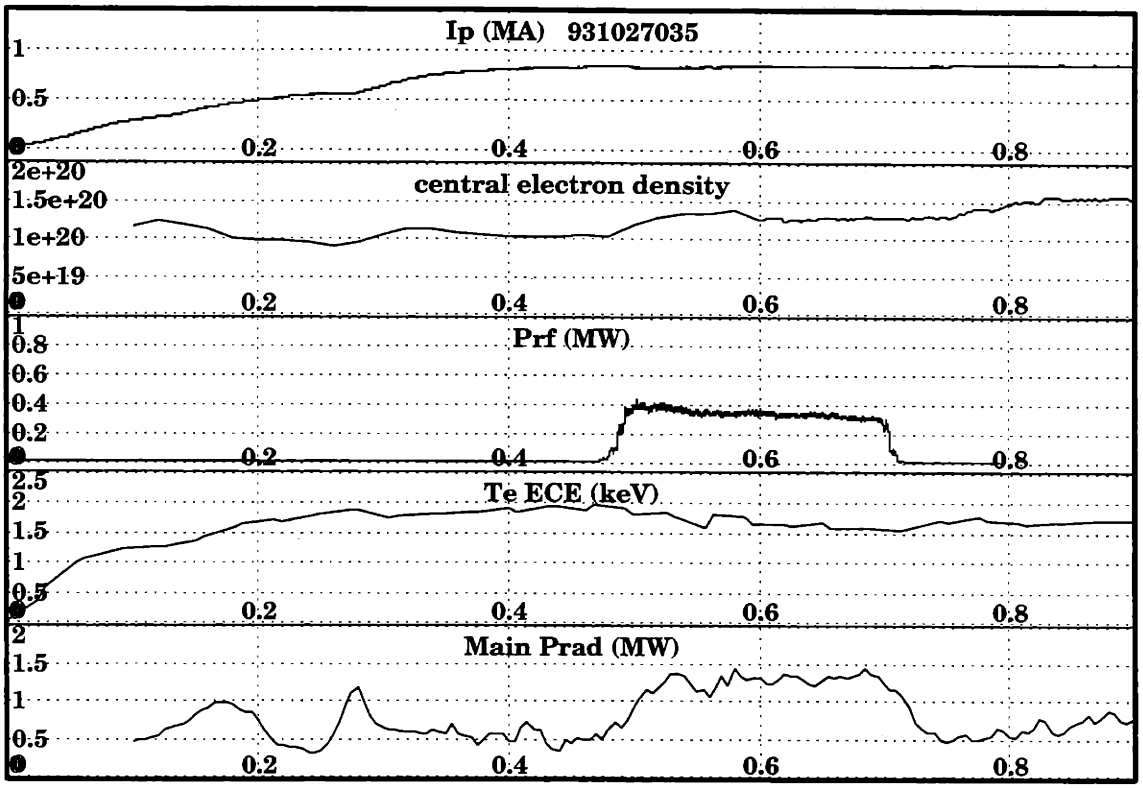

Figure 6-14: Plasma parameters during the application of 0.4 MW of ICRF power with the monopole antenna in 1993.

experiments comparing the effectiveness of each antenna as regards the impurity generation issue. Intrinsic impurity levels were measured during ICRF heating experiments in the same way that they were during ohmic operation. The same dominant intrinsic impurities (Mo, C) were again observed. The results of that comparison are presented below.

6.4.1 Comparison of Monopole and Dipole Antenna Configurations

Shown in Figures 6-14 and 6-15 are typical plasma parameters during the application of ICRF with the monopole and the dipole antennas respectively during similar high current, moderate density discharges. A few observations can be made immediately upon inspection of these parameters. One is that, in both cases, the application of the

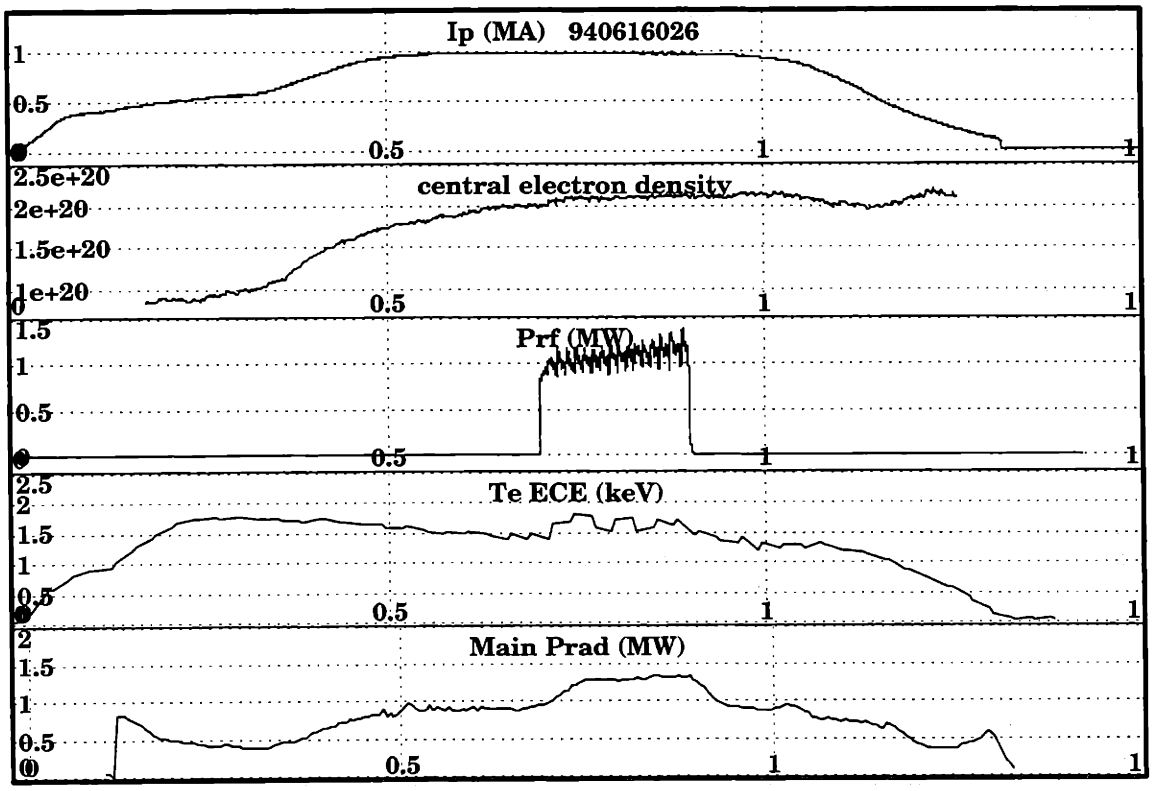

Figure 6-15: Plasma parameters during the application of 0.9 MW of ICRF power with the dipole antenna in 1994.

ICRF has dramatic effects on the density, temperature, and total radiated power in the discharges. These effects, however, are dramatically different for the different antennas. The electron temperature during the dipole application of ICRF was seen to rise by about 300 eV from its initial value of 1500 eV, a clear indication that heating was taking place. The radiated power was seen to rise by about 0.5 MW, an amount less than the net increase in input power to the plasma due to the ICRF source. During the monopole application of ICRF, however, the electron temperature was seen to drop by almost 300 eV and the radiated power was seen to rise by more than the ICRF input power. Clearly something fundamentally different was happening during these two discharges. A closer examination of the impurity behaviour during each shot provides some more insight into these differences.

Shown in Figure 6-16 are the brightness signals of the sodiumlike molybdenum line

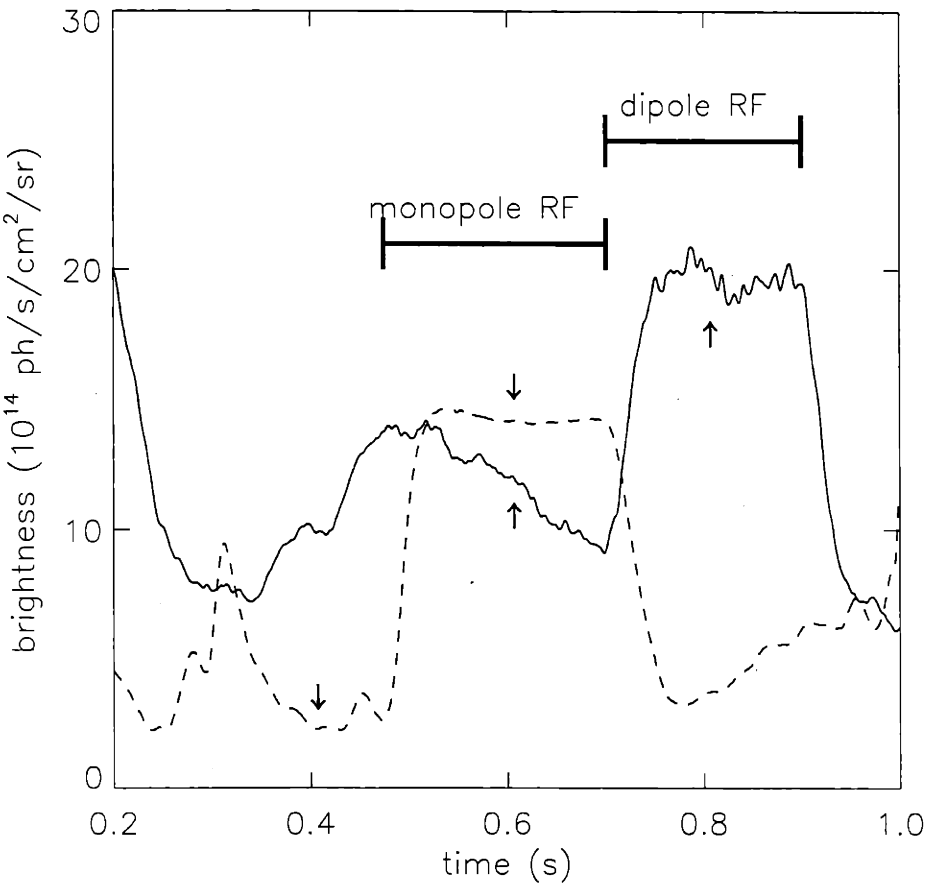

Figure 6-16: Brightness of the sodiumlike molybdenum line at 127.8 Å as observed with the MLM polychromator during a 0.4 MW monopole RF pulse from the 1993 campaign and a 0.9 MW dipole RF pulse during the 1994 campaign.

at 127.8 Å as observed with the MLM polychromator for the two discharges being considered. The time during which the RF is being applied is clearly marked in that figure. Notice that the increase in brightness of this molybdenum line during the monopole RF is at least a factor of 10, while it is closer to just a factor of three during the dipole RF. Of course, some of this increase may be due to changes in electron density and temperature during the application of the RF, as opposed to merely due to changes in molybdenum density. To sort out all of the possible influencing factors, the atomic physics model was applied to these discharges at two different times, just before, and then during the RF

	time (s)	f_{Mo} (10^{-4})	N_{Mo} (10^{16})	P_{rad} (MW)	Z_{eff}-1
monopole RF	0.4	0.78	0.56	0.09	0.08
	0.6	3.4	3.1	0.56	0.34
dipole RF	0.6	1.8	2.3	0.71	0.18
	0.8	2.2	3.1	1.0	0.22

Table 6.5: Results of molybdenum analysis at different times during monopole and dipole RF discharges.

pulse. These times are marked with arrows in the figure. The MIST code was used to generate molybdenum charge state density profiles based on consistent electron density and temperature profiles for the relevant times in each shot, and then the predicted emissivity profile for the sodiumlike resonance line was calculated and integrated along the line of sight of the MLM polychromator. The magnitude of the emissivity profile was adjusted until a best fit to the observed brightness was obtained. The required sodiumlike molybdenum density and hence the total molybdenum density necessary to produce that emissivity profile were then known quantities. From these numbers, the estimated radiated power contribution due to molybdenum for these shots could be obtained, along with the expected contribution to Z_{eff}-1. For the times indicated, these results are summarized in Table 6.5.

It is now clear, on the basis of the figures presented in Table 6.5 that the monopole RF pulse resulted in a much larger fractional and absolute increase in the amount of molybdenum in the plasma than did the dipole RF pulse. While the molybdenum level in the plasma started out much lower in the monopole case before the pulse was applied (a result which is highly dependent on the nature of the particular background discharge being run), it is seen to undergo an almost fivefold increase in fractional concentration, while the concentration in the dipole case is seen to increase by less than 30%. To illustrate further the differences in impurity behaviour between the monopole and the dipole antennas, Figure 6-17 shows the total core radiated power measured by the bolometer arrays as a function of the total input power (ohmic + RF) to the plasma over a range of input powers from 0.4 MW to almost 3 MW. The RF power ranged from 0.1-0.9 MW for

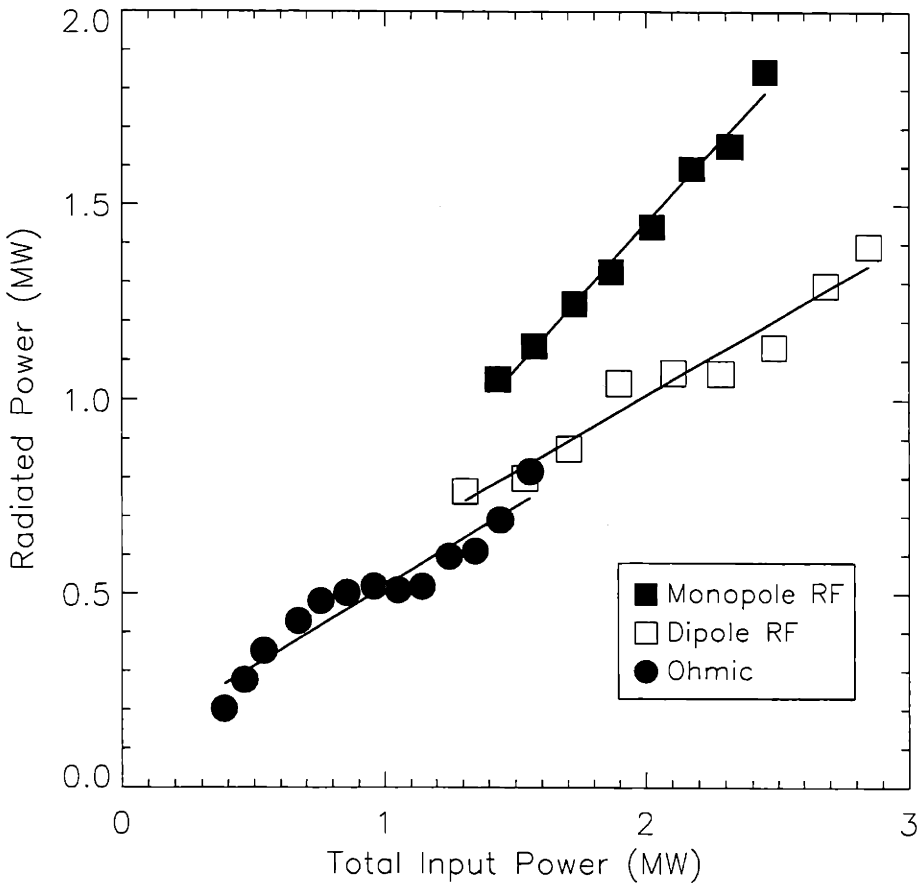

Figure 6-17: Total core radiated power as a function of total input power to the plasma showing the pure ohmic, ohmic + monopole antenna, and ohmic + dipole antenna cases.

the monopole antenna, and from 0.5-1.8 MW for the dipole antenna. The ohmic input power ranged from 0.4-1.6 MW for the discharges included in this database. The data points shown represent averaged values for a number of discharges with input powers in a given range. The standard deviation of values around the points shown is about 50% of the given radiated power. What is readily apparent from the data presented in this figure is that there does, in fact, exist a significant difference between the plasma performance achieved with the monopole antenna and that achieved with the dipole. Specifically, the fraction of total input power radiated away while using the dipole antenna is essentially the same as that radiated away during ohmic operation alone. This fraction is just under

50%, and is typical of most moderate density plasmas achieved in C-Mod. The fraction observed when using the monopole antenna, however, was significantly higher, reaching almost 70%. The ohmic only data which are shown were averaged over discharges taken from both the 1993 and the 1994 campaigns. Independent consideration of the ohmic data from each campaign shows that the ohmic behaviour during the 1993 (monopole) campaign does not appear to be significantly different from that observed during the 1994 (dipole) campaign. It therefore cannot be argued that the differences in RF performance between the two antennas are attributable to marked differences in machine conditions.

6.4.2 Conclusions

This chapter has reported on measurements made of the intrinsic impurity concentration in Alcator C-Mod during a variety of different operating scenarios. It has been shown that during normal ohmic operation in either the limited or the diverted magnetic configuration, the concentration of intrinsic impurities is a decreasing function of the electron density in the plasma. The diverted configuration has been shown to be clearly superior to the limited configuration from the point of view of minimizing the intrinsic impurity fraction in the plasma. This has been shown to be the case at all electron densities, although the differences are less pronounced at very high density. It is believed that at high density, the limited configuration is also able to operate in a regime where it is not overwhelmed by radiated power losses attributable to impurities. Extension of the database used for this investigation might include even higher input powers at still higher densities.

A comparison of impurity concentrations during a variety of RF heated discharges has shown that the dipole antenna configuration gave results superior to those obtained with the monopole antenna. Impurity concentrations in similar discharges were found to be at least a factor of five lower when the dipole antenna was used. Differences in sputtering rate caused by different accelerating potentials in the sheaths surrounding the plasma facing components has been cited as a probable explanation for the observations.

Confirmation of these results by operating the current dipole antennas in a monopole mode would prove to be a worthwhile experiment, as would extension of the database to higher RF powers.

Chapter 7

Impurity Screening Measurements

7.1 Introduction

The efficiency with which a plasma is able to screen impurities is an important quantity of interest in both present and future tokamaks. In addition to the obvious motivation of maintaining a plasma free from impurities, there exist scenarios which propose to dissipate plasma heat fluxes in a deliberately introduced highly radiating impurity layer. Such schemes are seen as possible solutions to the high heat flux problem foreseen for future reactors and are only feasible if the impurities can be localized well away from the core of the plasma. An accurate measure of the effectiveness with which a plasma SOL is able to shield the main plasma from an influx of impurities arising from a given source at the edge is therefore of great interest and has been studied at some length [47, 48].

To quantify such an investigation, it is convenient to define a penetration efficiency which relates the number of atoms of a given impurity present in the core plasma to the number actually introduced by the relevant source mechanism at the edge of the plasma. This quantity, $\eta_{penetrate}$, can be defined as

$$\eta_{penetrate} = \left(\frac{\text{total impurity atoms in core}}{\text{total impurity atoms injected}} \right) \tag{7.1}$$

Its complement, $\eta_{screen} = 1 - \eta_{penetrate}$, can be thought of as a plasma screening efficiency.

This chapter investigates the dependence of $\eta_{penetrate}$ on various plasma parameters by purposely injecting known quantities of different impurities into the plasma. In addition to varying the impurity species, the location of the source and its incident energy are varied using different injection techniques. The background plasma parameters, especially the density are varied to investigate any dependence of $\eta_{penetrate}$ on edge plasma conditions. Finally, the plasma magnetic geometry is varied from limited to diverted discharges in order to evaluate any benefit the divertor might be providing to the screening of impurities.

7.2 Experiments

Impurity injections for the purpose of measuring screening efficiencies were made with three separate systems, the laser ablation injection system, the divertor gas puff injection system, and the main gas fuelling system. Each was used to provide unique information about impurity screening for different non-intrinsic and intrinsic impurities at different locations around the plasma. The laser ablation impurity injection system was used to introduce energetic non-recycling impurities at the plasma midplane. The divertor gas injection system was used to inject room temperature recycling gases through capillary tubes in the divertor and at the inner wall. The main gas fuelling system was used to inject these same gases through fast piezoelectric valves at the plasma midplane. In each case, a calibrated amount of impurity was introduced at the edge of the plasma and measurements of the amount of the impurity observed in the core plasma (inside the separatrix) were made. Well-defined injections of about 3×10^{17} atoms of scandium were made with the laser ablation injection system. These atoms typically had a directed energy of a few eV when they were incident on the edge of the plasma. Gaseous injections with flow rates of up to 10^{19} atoms per second of argon, neon, nitrogen, methane, and helium were made with the divertor gas injection system and the main gas fuelling system. The initial energy of these atoms was low (room temperature), but their recycled energies

impurity	observed state	transition	instrument
scandium	18+	2s-2p (279 Å)	VUV spectrometer
	19+	1s-2p (2.9 Å)	HIREX
argon	15+	2s-2p (353 Å)	VUV spectrometer
	16+	1s-2p (3.9 Å)	HIREX
neon	7+	2s-2p (770 Å)	VUV spectrometer
nitrogen	6+	1s-2p (24.8 Å)	VUV spectrometer
	5+	1s-2p (29.1 Å)	VUV spectrometer
methane	5+	1s-2p (33.7 Å)	VUV spectrometer
(carbon)	4+	1s-2p (40.7 Å)	VUV spectrometer
helium	1+	1s-2p (304 Å)	VUV spectrometer

Table 7.1: Elements and compounds injected for impurity screening experiments along with the spectroscopically observed transitions used for the analysis.

tended to be higher (1-2 eV) [49].

7.3 Analysis Technique

Following the injection of these trace impurities, measurements of the total number of impurity atoms observed in the core plasma were made and used to define the impurity screening efficiency of the plasma. These measurements were based on spectroscopic observations of line emission from one or several impurity charge states. Appropriate charge state distribution modelling was necessary to arrive at a total impurity density in the plasma. Whenever more than one impurity line was observed, it was used as a check on the consistency of the measurements. The observable lines for the impurities investigated are listed in Table 7.1.

7.3.1 Laser Ablation Injection Analysis

The laser ablation injections represent an impurity source fundamentally different than that obtained with a gas puff injection. The ablation source is close to being a delta function in time. Its lifetime at the edge of the plasma, based on a consideration of the spreading of a beam of atoms with a Maxwellian distribution of a few ($\leq$ 10) eV,

is as short as a few hundred microseconds. Since this time is short compared with the characteristic perpendicular transport time in the plasma, and since the impurities injected in this way are chosen to be non-recycling, the transport of the impurities in the plasma must be treated in a fully time dependent way. This time dependent analysis was performed using the MIST transport code. In the code, a specified number of atoms were introduced at the wall of the simulation geometry. The ionization of these atoms was calculated and used to generate a poloidally symmetric profile of singly ionized ions whose progress through the plasma was followed according to the formalism described in Chapter 4. The time dependence of each charge state of the impurity was obtained in this way and used in subsequent analysis. An entirely different approach was used where the gaseous impurity injections were concerned.

7.3.2 Gas Puff Injection Analysis

While the laser ablation source could be considered instantaneous, the recycling gas injection source from both gas systems is extended in time. Since the divertor gas puff system which was used required the gas to travel through about 3 meters of capillary tubing before reaching the plasma edge, the time-dependent behaviour of the gas flowing in the tube needs to be treated correctly in order to have an accurate measure of the total number of atoms injected at any given time in the experiment. An explanation of the modelling of the flow through these capillaries can be found in [50]. The important result, however, is that most of the gas injected by a single pulse of the valve controlling a given capillary does not reach the vacuum chamber until well after the plasma discharge has ended. Up to 70% of the total gas flowing through the capillary may not leave the end of the tube until at least 3 seconds after the valve has been fired. This can prove to be extremely problematic from the point of view of the analysis if not treated correctly. Typical injections are shown in Figure 7-1 for the three gases studied along with the duration of a typical discharge.

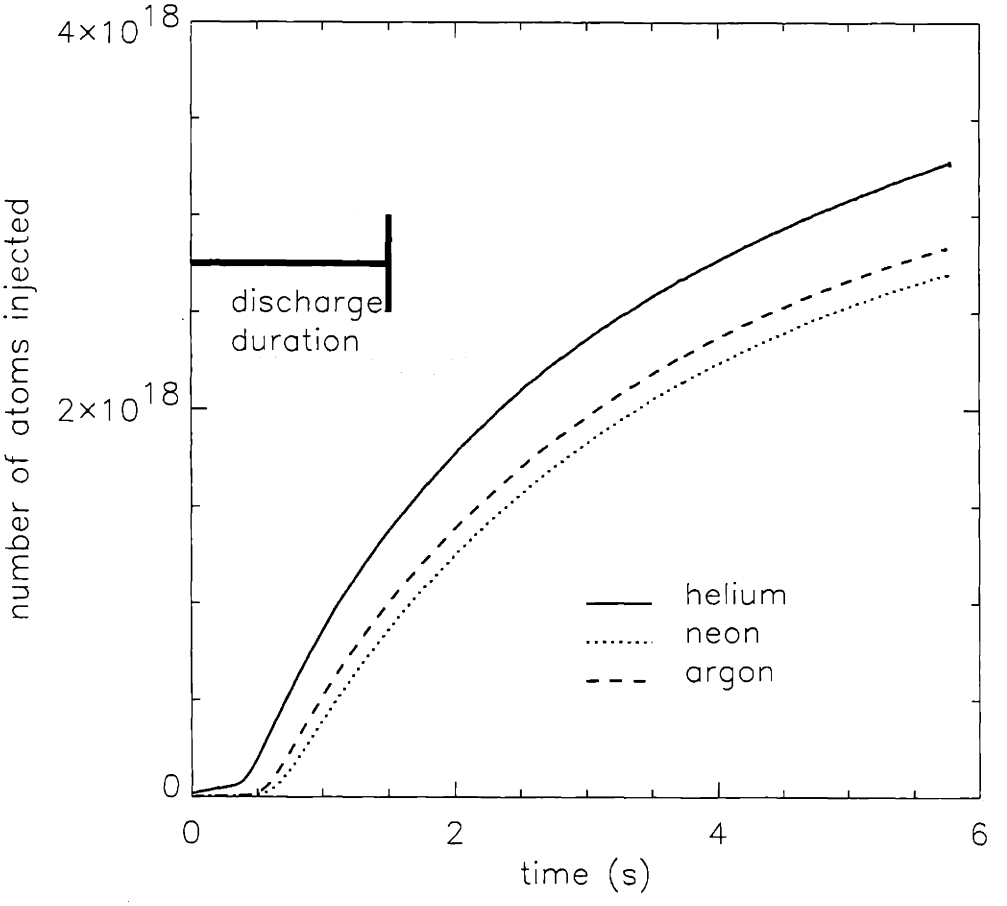

Figure 7-1: Number of atoms injected through the divertor gas puff system for different gases at roughly the same plenum pressure. The trigger time for the valve in each case was t=0 s. The typical duration of a discharge is also shown.

7.4 Results

7.4.1 Laser Ablation Injections

A number of reproducible injections of scandium was made into different background plasmas. The reproducibility of the injections was verified visually through an examination of the target slide spot and more quantitatively through an examination of the total laser pulse energy as measured with the laser power monitor (see Chapter 2). The variation in the injections was observed to be less than about 25% in this series of discharges.

The number of atoms incident on the edge of the plasma was calculated according to the technique outlined in Chapter 2 to be nominally 3×10^{17}. For each injection, a time dependent MIST simulation was used to generate the charge state density profile time evolution. The collisional-radiative model was then applied to compare the observed brightness of the appropriate line (Table 7.1) along a given line of sight to the model prediction. The modelled total number of atoms inside the plasma was then adjusted until good agreement was reached between predicted and observed brightness measurements. Shown in Figure 7-2 is the measured penetration efficiency as a function of line-averaged electron density.

Two important observations can be made from these results. The first is related to the absolute magnitude of the screening efficiency measured in this way. For all of the cases investigated, this efficiency is greater than about 85%, implying that the majority of source atoms at the edge of the plasma do not penetrate through to the core. The second is related to the dependence of this screening efficiency on electron density. An inverse dependence is readily apparent. This result can be understood qualitatively at least through a realization that the ionization rate due to electron impact of a neutral (or of any charged ion) is directly proportional to the local electron density. Given that there is typically a fixed proportional relationship between the line-averaged and the edge electron density (see Chapter 4), it is reasonable to expect that as the edge electron density increases, so does the ionization rate outside the separatrix. Any ion on an open field line outside the separatrix has a greatly increased likelihood of flowing to the walls of the chamber instead of diffusing into the plasma core. It is this mechanism of ionization outside the separatrix which is responsible for keeping impurities out of the core.

7.4.2 Gas Puff Injections

A series of injections of different gases into a variety of discharges was also performed. Injections of helium, methane, nitrogen, neon, and argon were made through capillaries in the private flux region discharges and through both capillaries and piezoelectric valves

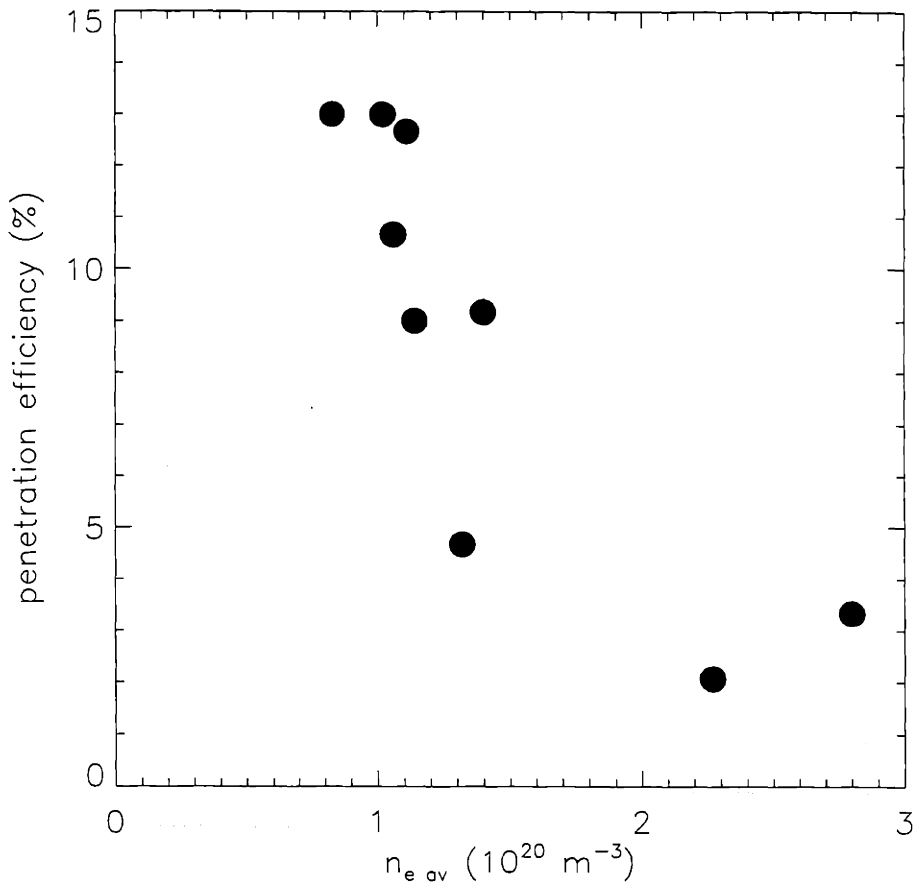

Figure 7-2: Penetration efficiency of laser blow-off injected scandium plotted versus line-averaged electron density for a series of diverted discharges.

at the midplane. The results obtained using these different gases are presented below.

Neon

Shown in Figure 7-3 is the spectrum used for analysis of the neon gas injections. The particular discharge from which this spectrum was taken had a neon injection through a divertor capillary with a flow rate similar to that shown in figure 7-1. The lithiumlike doublet lines at 770 Å and 780 Å are both readily observable in the bandwidth of the VUV spectrometer at these wavelengths. A spectrum obtained early in the discharge before any neon had been injected and one obtained late in the discharge are shown

in that figure. By fitting the spectrum to a number of known lines, the relevant neon lines can be isolated and their time behaviour considered. The observed brightness time history can be modelled using the MIST transport code and the appropriate collisional-radiative model for the neon lines in question. The standard lithiumlike model which includes five separate lines and the interactions between them was used for this analysis. The appropriate coefficients used are found in Appendix B. After converting the observed brightness to a total number of atoms present inside the separatrix, this number can be compared to the number of atoms injected at any given time. For this injection, the calculated number of atoms in the plasma was about 5% of the total number injected at the edge at any time. Injections of this type were repeated at a number of different poloidal locations around the machine. No clear differences in either the time histories or the absolute magnitudes of the penetration efficiencies were noticed as a function of the injection location.

It should be pointed out that the calibration for the VUV spectrometer in this region of the spectrum is only certain to within about a factor of two (see Chapter 3). The absolute magnitude of the penetration efficiencies determined using this technique for neon, at least, are therefore only accurate to within about that same factor. The next section will outline another technique, which relies on changes in the measured Z_{eff} of the plasma, which can at least place an upper bound on the impurity penetration.

In addition to the capillary injections of neon described above, a number of injections using the piezoelectric valves was also performed. These were interesting insofar as they provided a much different time history than did the capillary injections. Rather than a slow increase in the amount of neon introduced at the edge of the plasma, the piezoelectric valve, which was typically pulsed for about 50 ms, introduced the same number of atoms to the edge of the plasma in a much shorter time. The resulting time history of the brightness of the lithiumlike neon line is shown in Figure 7-5. The advantage of this technique of injection lies in the increased accuracy with which the total number of atoms injected can be determined. No longer is the injection time long compared with

the discharge time. Penetration results obtained using this injection technique were similar to those obtained with the capillary injections. Penetrations of about 5% were observed. The penetration was also found to be a decreasing function of average electron density

Argon

Analysis of the argon injections was performed using spectra taken with the HIREX spectrometer array. A typical spectrum is similar to that shown in Figure 6-5, where the resonance line, which is usually brightest for any chord viewing the center of the plasma, is chosen to be the preferred line for the analysis. Injections were made through both the midplane piezoelectric valve and the capillary tubes. In both cases, penetration efficiencies comparable to those measured during the neon injections were observed. A unique set of experiments which investigated the effect of magnetic geometry on the penetration was also performed using argon injected through a piezoelectric valve at the midplane. These experiments were conducted as part of the same series of experiments which compared intrinsic impurity levels during limited and diverted discharges. A description of the details of those discharges can be found in Chapter 6. The results are shown in Figure 7-6 where the penetration efficiency is plotted as a function of line-averaged electron density for both limited and diverted discharges. Two important observations can be made from this figure. One is that the penetration efficiency is higher by almost a factor of two for all of the limited discharges investigated. This is a significant result in that it demonstrates one of the key desirable features of a diverted plasma, that of increased impurity control. The second observation is that there does not appear to be any noticeable dependence of the penetration efficiency on the electron density. This is in qualitative disagreement with the results obtained from the laser ablation scandium injection experiments.

A further observation which can be made about the magnitude of the penetration efficiency measured using this technique is that it is significantly lower than that measured

on other diverted tokamaks. In particular, DIII-D has reported in the past penetration efficiencies of order 50% for argon as measured using a similar technique [47]. One possible explanation for this difference may lie in the fact that DIII-D operates with a much more open divertor configuration. The strong baffling effect which the mostly closed lower divertor on C-Mod provides is not in evidence on any other machines. This baffling may lead to better confinement of recycling impurities at locations remote from the separatrix and thereby enhance the screening efficiency of the plasma. This explanation, however, does not explain why, even in limited configurations, the C-Mod screening efficiency is still higher than that of DIII-D. Alternative explanations may be related to the higher edge electron densities present in C-Mod which would tend to ionize impurity neutrals more quickly before they reach the last closed flux surface. More detailed experiments with other gases and geometries are underway at DIII-D with the hope of shedding more light on these differences.

Nitrogen

A non-recycling, low Z gas used in these injection studies was nitrogen. Injections were made through both the midplane piezoelectric valve and the capillary tubes. Spectral lines from both the heliumlike and the hydrogenlike charge states were observed with the VUV spectrometer. A typical spectrum is shown in Figure 7-7. The lines observed are exactly analogous to those observed for the same charge states of carbon. A typical time history of the brightness of the Lyman-α line during an injection of duration 50 ms at 0.6 seconds is shown in Figure 7-8. The time histories of these lines should be compared with those obtained during the neon injections using the same midplane valve. While the neon brightnesses increased quickly and remained at or near their peak levels throughout the remainder of the discharge following the injection, the nitrogen brightnesses decay back to the pre-injection levels very soon after the injection ends. This is confirmation of the fact that nitrogen is primarily a non-recycling impurity. In fact, the characteristic decay time of the nitrogen brightness following the puff can be used as a gauge of just

how much of the nitrogen does recycle. The characteristic impurity confinement time for wholly non-recycling impurities was derived from the experiments described in Chapter 5. For the discharge shown in Figure 7-8, this time is predicted to be 23 milliseconds. The characteristic time observed for the decay of the nitrogen brightness signals is slightly longer (26 milliseconds). If the decay of a partially recycling impurity is taken to be proportional to $\exp(-t/(1-R)\tau_{NR})$ where τ_{NR} is the predicted decay time of a non-recycling impurity, then the recycling coefficient, R, can be given by:

$$R = 1 - \frac{\tau_{measured}}{\tau_{NR}} \tag{7.2}$$

For the discharge shown, the inferred recycling coefficient of the nitrogen is found to be about 0.1, consistent with the supposition that it is a mostly non-recycling gas. At the peak of the injection, a penetration efficiency of nitrogen of about 5% was observed for these discharges. This is similar to the results obtained with both the argon and the neon injections. It is also comparable to the values obtained with the wholly non-recycling scandium injections.

7.4.3 Comparison with Zeff

As a check on the consistency of the inferred number of atoms of each injected species in the plasma, changes in the measured Z_{eff} can be used. To zeroth order, the contribution to Z_{eff} from a given impurity can be approximated by:

$$\Delta Z_{eff} \sim \frac{n_I}{n_e}(Z)(Z-1) \tag{7.3}$$

where n_I is the total impurity density and Z is the charge of the most abundant state of that impurity present in the plasma. For most of the trace gas injections conducted as part of this investigation, Z_{eff} was observed to rise very little, if at all. The resolution with which changes in Z_{eff} can be determined has been estimated at about 0.05 [51]. It has been noticed that there is generally consistent agreement between the limits set by the Z_{eff} observations and the efficiencies measured by observation of line emission.

During some of the higher level gas injections which were intended to perturb the plasma and radiate preferentially from the edge, distinct changes in Z_{eff} were noticed. This was particularly true during the strong neon injection experiments which introduced neon through a midplane piezoelectric valve. In fact, despite the large amounts of neon introduced by these experiments, the measured change in Z_{eff} was still larger than could be accounted for by the neon alone. In these cases, it was observed that the amount of molybdenum in the plasma was also increasing as more neon was injected. Shown in Figure 7-9 are various signals associated with a large neon injection occurring at time 0.5 seconds. The signals include the brightness of the lithiumlike neon line at 770 Å as measured with the VUV spectrometer, the brightness of the sodiumlike molybdenum line at 128 Å as measured with the MLM polychromator, the central Z_{eff} of the plasma, and the total radiated power from the plasma as measured with the bolometer arrays. While the brightness of the injected impurity line is seen to increase many-fold, the molybdenum signal is also observed to increase by about a factor of two. This is indicative of a substantial increase in the amount of molybdenum in the plasma, presumably due to increased sputtering of molybdenum by the large quantities of the newly introduced impurity species. Such a finding is consistent with results obtained by observing low charge states of molybdenum during trace impurity injection experiments [52].

7.5 Conclusions

This chapter has reviewed a number of experiments which dealt with the penetration of impurities from the edge of the plasma into the core. For this investigation, recycling and non-recycling impurities were introduced using the the laser ablation, capillary, and piezoelectric valve injection systems. It was demonstrated that the fraction of impurities injected at the edge of the plasma which were later observed in the core was never larger than about 15%. This fraction was also seen to decrease with increasing electron density at the edge and was attributed to an increase of local ionization there. No clear differences

were observed between injections made at different poloidal or toroidal locations around the machine. Large changes in Z_{eff} and in total radiated power during large impurity puffing experiments have been attributed to an enhanced influx of sputtered molybdenum in addition to the injected impurities themselves.

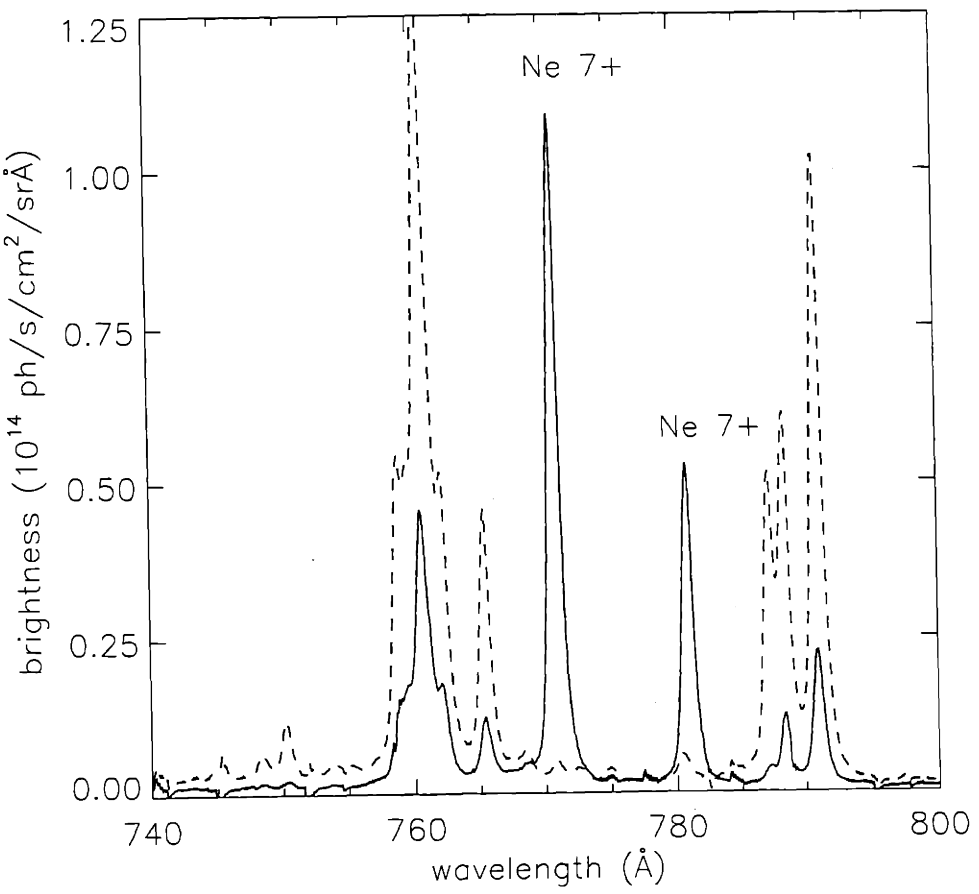

Figure 7-3: Spectrum used for analysis of neon injections showing the lithiumlike doublet at 770 Åand 780 Å. The dashed line is a spectrum obtained before any neon had been injected. The solid line is a spectrum obtained near the end of the discharge, when the amount of neon in the discharge is at a maximum.

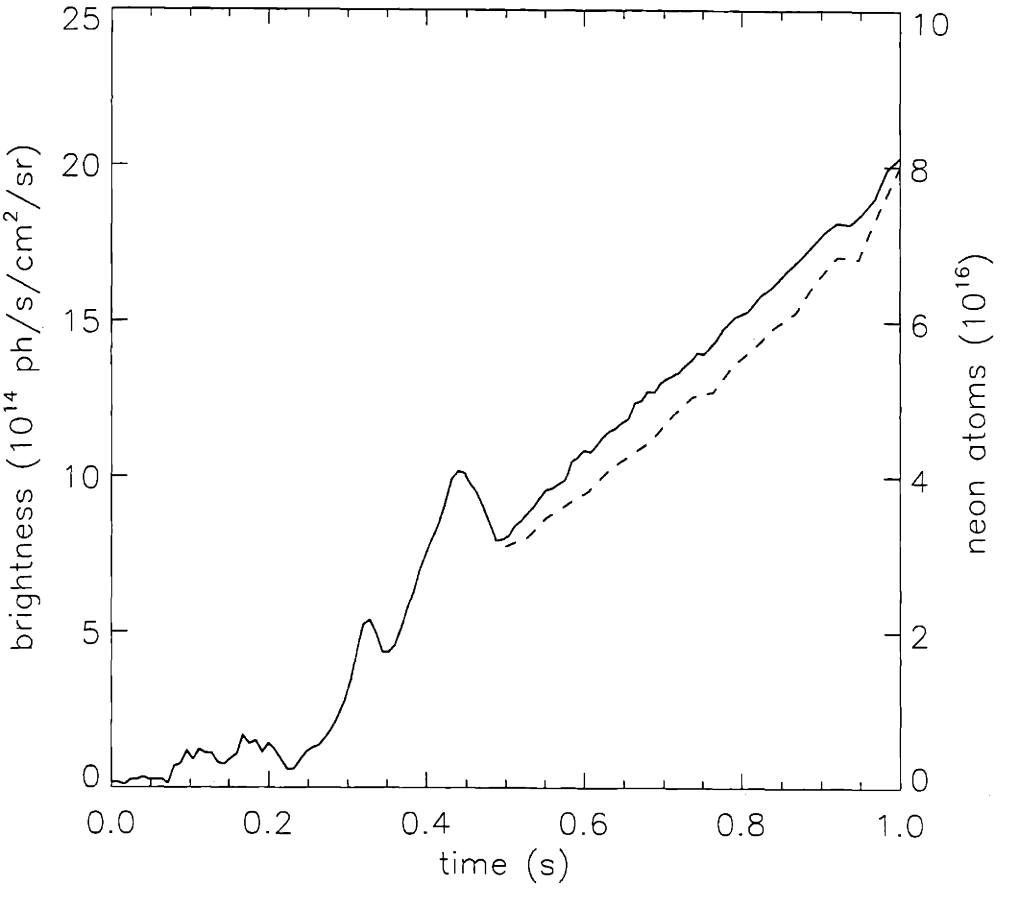

Figure 7-4: Time history of the brightness of the lithiumlike doublet lines (solid line) of neon. Also shown is the calculated number of atoms of neon in the core plasma as a function of time.

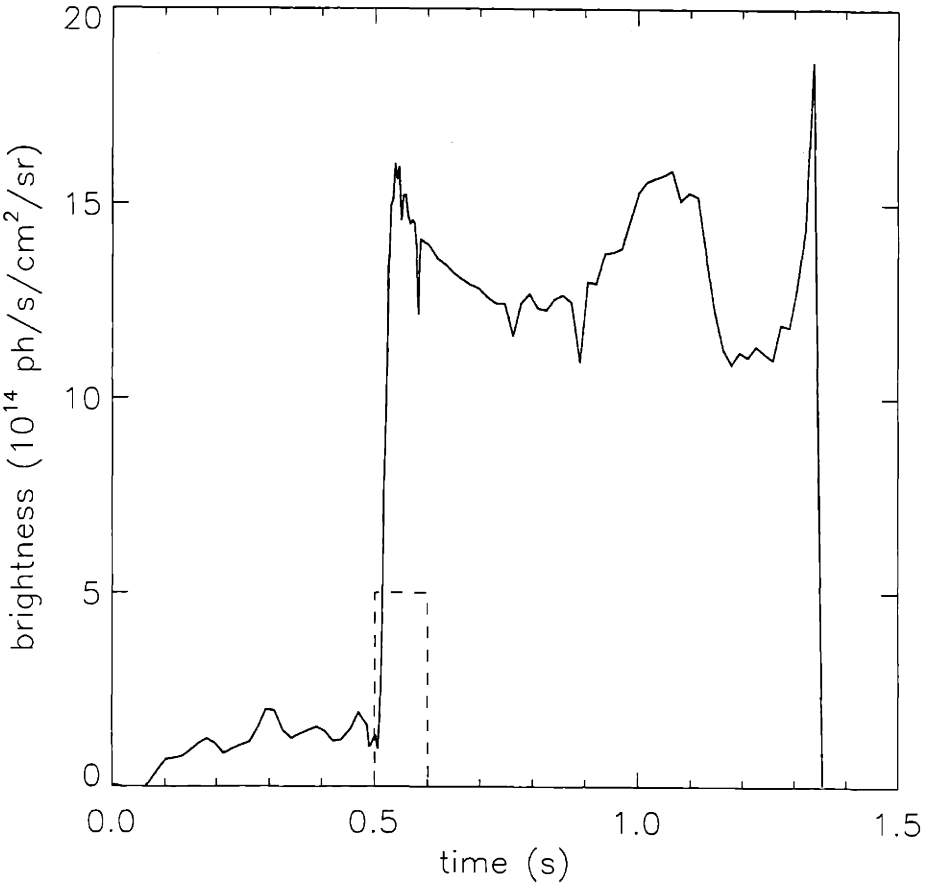

Figure 7-5: Time history of the brightness of the lithiumlike neon line at 770 Å during a discharge with a 50 ms injection of neon through a midplane piezoelectric valve (dashed line).

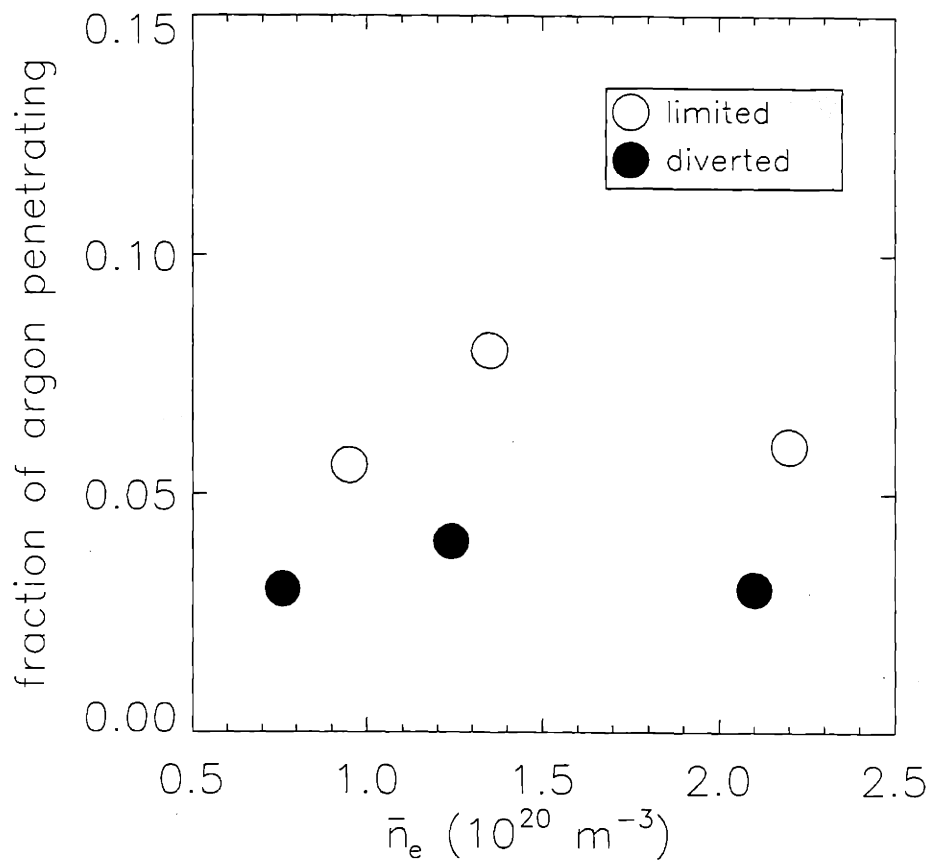

Figure 7-6: Comparison of measured argon penetration efficiency for limited and diverted discharges over a range of densities.

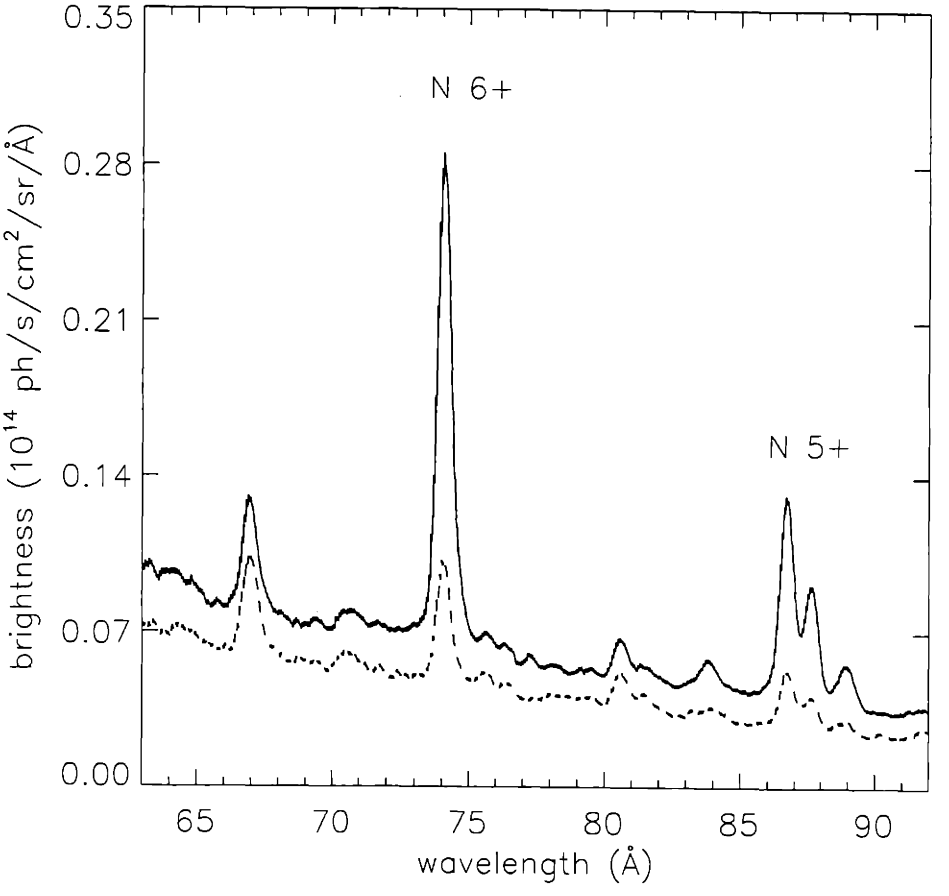

Figure 7-7: Spectrum used for analysis of nitrogen injections showing the Lyman-α line in third order at 74 Å and the heliumlike resonance and intercombination lines in third order at 86.5 and 87.5 Å. The dashed line is a spectrum taken before the injection. The solid line is a spectrum taken during the peak of the injection. Also seen are the analogous lines in the carbon spectrum in second order.

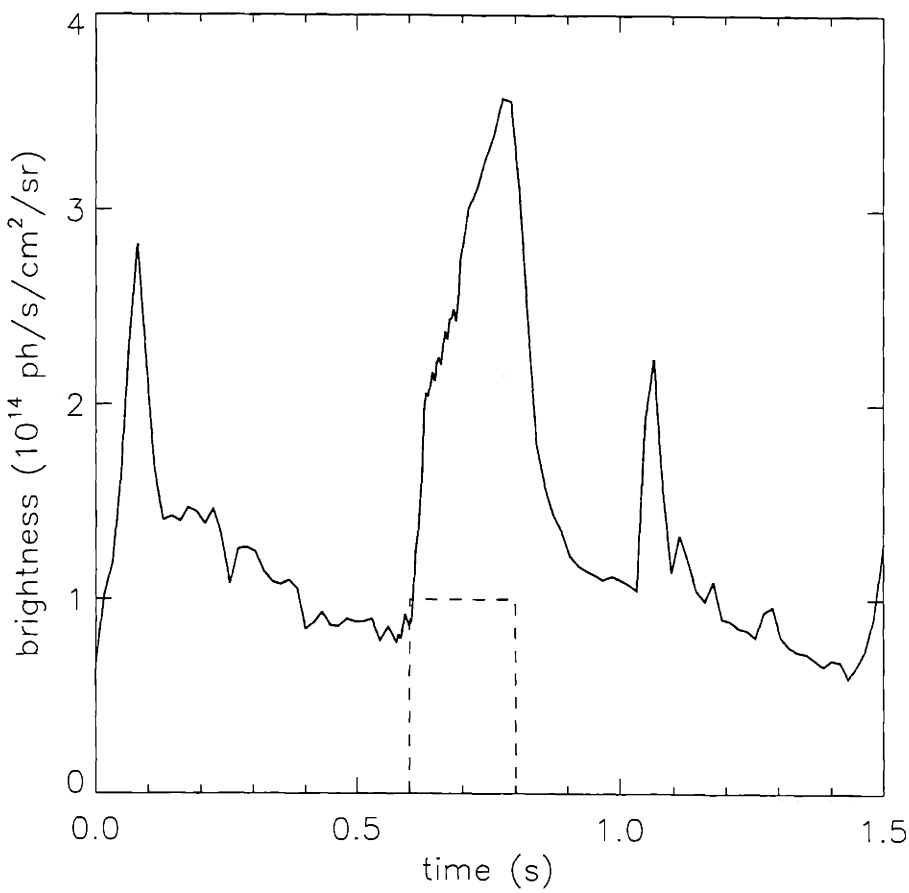

Figure 7-8: Time history of the brightness of the Lyman-α nitrogen line at 74 Å during a discharge with a 50 ms injection of nitrogen through a midplane piezoelectric valve (dashed line).

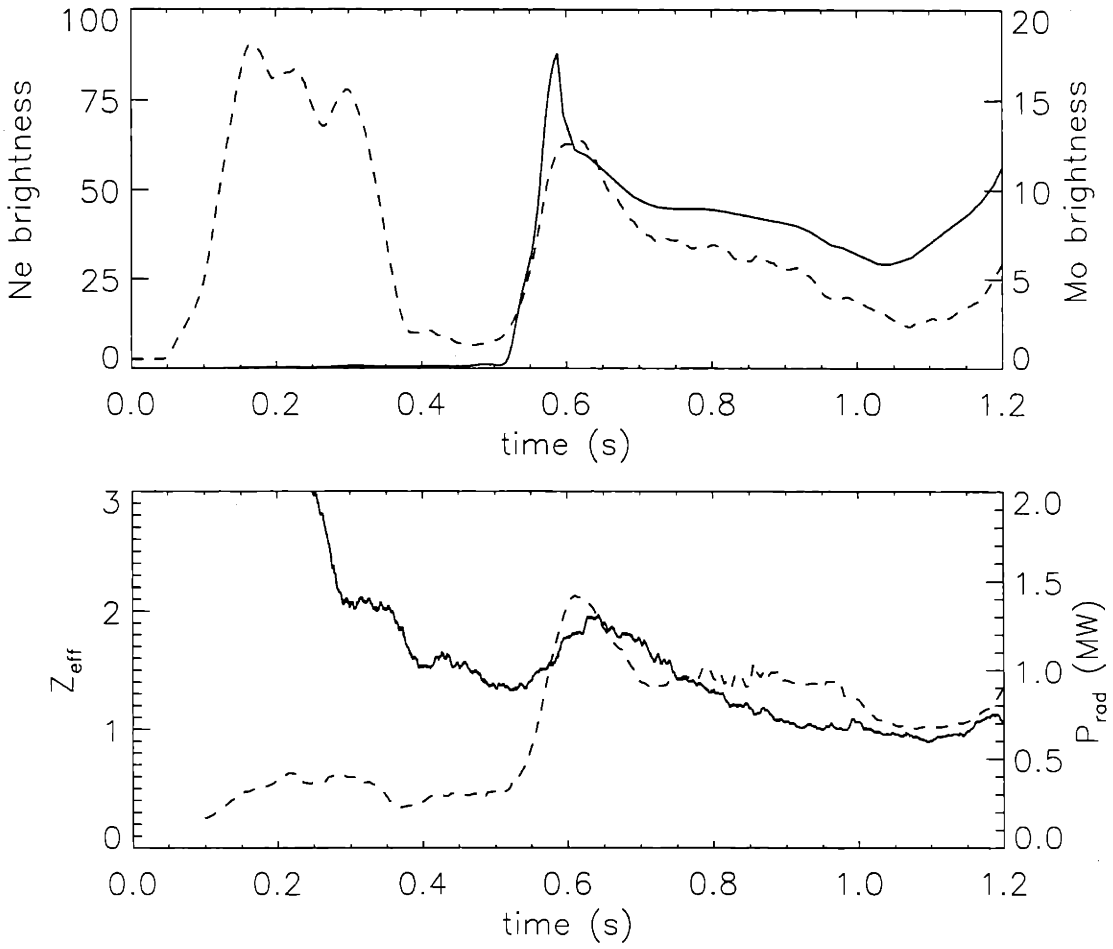

Figure 7-9: The time history of the brightness of the lithiumlike neon and the sodiumlike molybdenum lines during a large injection of neon from the midplane piezoelectric valve. Also shown are the Z_{eff} of the plasma along with the total radiated power as functions of time.

Chapter 8

Measurement of Neutral Density Profiles

8.1 Introduction

There is a number of techniques available for measuring the neutral particle density profile in Alcator C-Mod. These include using observations of H_α emission, energetic neutral particle flux, and charge exchange recombination reactions with impurity ions. Each of these methods, however, has its own limitations. It is only through a consideration of all three that a complete picture of the neutral density profile can be understood.

H_α emission is typically considered to be the most direct method of measuring a local neutral particle density. When using H_α emission to determine the local neutral particle density, both the local electron temperature and electron density must be known. This H_α emission alone, however, is capable of providing only an edge measurement of neutral density, since the density of neutral hydrogen (and hence the level of total H_α emission) falls off strongly in regions of the tokamak where the temperature is much higher than about 10 eV. While this is an important measurement, it can provide no information about the profile of neutral particles in the core plasma. A neutral particle analyzer, on the other hand, measures the flux of energetic neutrals leaving the plasma and does

provide information about the distribution of neutrals in the core. In a high density tokamak such as Alcator C-Mod operating at moderate electron temperatures, however, the centre of the plasma is 'thick' to neutrals born there [53]. This diagnostic is therefore also limited to observing neutrals from non-central regions of the plasma A technique which does offer the possibility of observing central as well as edge neutral densities involves the consideration of the effects of charge exchange recombination reactions of neutrals with impurity ions. It is known that charge exchange recombination with an impurity ion preferentially populates certain excited states of the given ion. By observing line emission from these preferentially excited states along various chordal views through the plasma, it is possible to infer a neutral density profile. The extent of the inferred profile depends on the spatial extent of the recombining impurity charge state and on the ability to extract local quantities from line-integrated measurements.

In diverted Alcator C-Mod plasmas, it is possible that a large gradient of neutral density will exist from the midplane to the divertor region. One of the goals of this diagnostic technique is therefore to try to quantify this gradient both at the edge of the plasma and in the core. A determination of the neutral density profile will also allow for calculation of the energetic neutral flux which is incident on the plasma facing components and for some estimate of the impurity generation rate due to that flux. These calculations can be compared with direct measurements made by the neutral particle analyzer. Similar observations of charge exchange with argon were made in a purely circular geometry on the Alcator C tokamak [54]. Comparisons with those observations for limited, near circular discharges on C-Mod can also now be made.

8.2 Charge Exchange Model

The charge exchange reaction of interest for the purpose of deducing neutral particle density is of the form:

$$A^{+q} + H^0 \rightarrow A^{+q-1^*} + H^+ \tag{8.1}$$

where A^{+q} refers to the impurity A of charge +q and H^0 refers to neutral hydrogen or deuterium in the ground state. (In the context of these experiments, hydrogen and deuterium are considered to be equivalent.) There is also the possibility of charge exchange from neutral hydrogen in an excited state. It is line emission from transitions out of the state A^{+q-1^*} which will be used to determine the neutral density. The actual charge exchange mechanism can be thought of as a two-step process in a simplistic model. First, the actual transfer of the charge exchange electron from the neutral to the ion tends to occur preferentially into levels of the ion, n_c, whose binding energy is similar to the ionization potential of the initial neutral atom. For ground state neutral hydrogen this energy is 13.6 eV and the level, n_c is equal to the Z of the receiving ion. Following the electron transfer, the next step in this idealized process is a re-arrangement of the newly formed ion which seeks to balance the gain in potential energy experienced by the now bare hydrogen nucleus. Before re-arrangement, this potential energy is

$$P.E. = \frac{(Z-1)e^2}{r_n} \tag{8.2}$$

for the case of charge exchange with ground state hydrogen, where Z refers to the initial charge of the ion and r_n is approximately the radius of the ion at the level into which the electron was initially transferred. For hydrogenlike ions this radius can be written:

$$r_n = \frac{n_c^2}{Z} a_0 \tag{8.3}$$

in terms of the Bohr radius a_0. The change in potential energy which comes about as a result of this re-arrangement is just the difference in ionization potential between the initial capture level n_c and the ultimate level, n_0. This difference is:

$$\frac{e^2}{2a_0}\left(\frac{Z^2}{n_0^2} - 1\right) \tag{8.4}$$

where $\frac{e^2}{2a_0}$ is recognized as the Rydberg energy. The difference in equation 8.4 must be set equal to the potential energy in equation 8.3.

Of course, since in general no single level will exactly accommodate these requirements, there will be some distribution of final states around the most probable state into

which the charge exchange electron will fall. For hydrogenlike ions, n_0 can be solved for to yield [54]:

$$n_0^2 \simeq \frac{Z^3}{(3Z-2)} \tag{8.5}$$

For specific impurities, fits to a particular distribution have been made and are presented in the form of an analytic rate coefficient in the next section.

8.3 Experimental Procedure

The impurity selected for use in these experiments was argon. This choice was made on the basis of ease of injection and the availability of spatially resolving spectroscopic diagnostics which were capable of viewing line emission from the appropriate atomic transitions. Non-perturbing amounts of argon, as mentioned earlier, are routinely injected into the tokamak for the purposes of measuring ion temperature profiles. Similar amounts of argon were used for the measurement of neutral density profiles. In order that the line emission due to charge exchange from heliumlike Ar^{16+} was of a sufficient intensity that meaningful results could be obtained, it was necessary to have a significant amount of hydrogenlike Ar^{17+} in the plasma. The fractional abundance of various charge states of argon in coronal equilibrium is shown in Figure 8-1. From this figure, it can be seen that only at electron temperatures above about 1.5 keV do the amounts of hydrogenlike argon begin to be significant. This is true even if transport effects are taken into account. It was therefore desirable to operate the tokamak at temperatures in this range. At the time these experiments were carried out, these represented among the hottest temperatures ever achieved in C-Mod during Ohmic operation.

The particular charge exchange reactions of interest for argon are:

$$Ar^{17+} + H^0 \rightarrow Ar^{16+^*}_{n\sim 9} + H^+ \tag{8.6}$$

$$Ar^{17+} + H^{0^*} \rightarrow Ar^{16+^*}_{n\sim 18} + H^+ \tag{8.7}$$

where the final excited state of Ar^{16+} after charge exchange with neutral ground state hydrogen will be $n \simeq 9$. (The expression in equation 8.5 actually gives a number closer

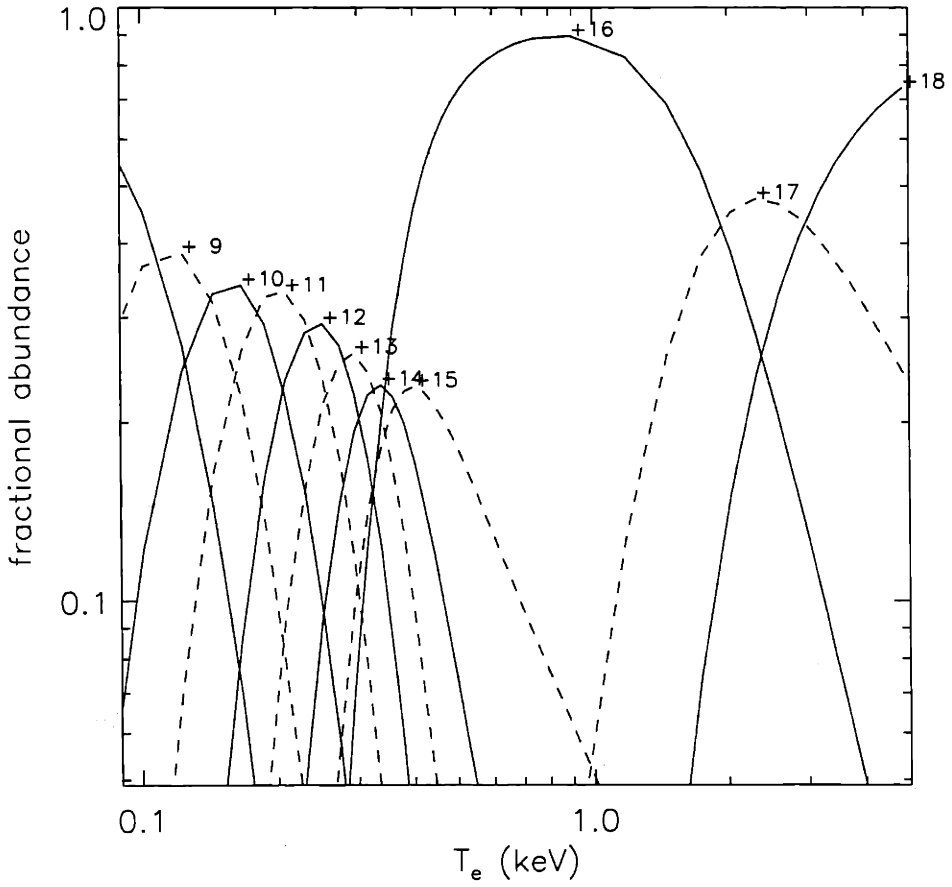

Figure 8-1: Fractional abundance of some high charge states of argon in coronal equilibrium as calculated by the MIST code.

to 10, but it will be shown that $n \simeq 9$ gives results more consistent with observations and other models.) For charge exchange with neutral hydrogen in the first excited state, the final excited state in Ar^{16+} will be about 18. Transitions of interest will therefore be those around 1s-9p and 1s-18p in the heliumlike argon system. In order to separate the contribution to the brightness of these lines due to charge exchange from the contribution due to other population mechanisms, it was useful to observe many transitions of the type 1s-np. In fact, using the HIREX spectrometer array, it was possible to observe simultaneously such transitions for $6 \leq n < \infty$. These all occur in the wavelength range 3009 mÅ $< \lambda <$ 3100 mÅ. Note that 3009 mÅ is approximately the wavelength

corresponding to the ionization potential of the ground state of the heliumlike ion.

To interpret properly the brightness of these lines, consideration must be given to all of the dominant mechanisms which populate the upper levels of the transitions. The model used here includes contributions due to electron impact excitation, radiative recombination, and charge exchange recombination. The rate coefficient for electron impact excitation of the 1s-np transitions has been modelled as [55]:

$$S_{ex_n} = c_{ex} \cdot f_n \cdot \frac{1}{\Delta E_n \sqrt{T_e}} \exp\left(-\frac{\Delta E_n}{T_e}\right) \tag{8.8}$$

The rate coefficient for radiative recombination to the np upper level has been modelled as [56]:

$$\alpha_{rr_n} = c_{rr} \cdot \frac{1}{n^3} \cdot \frac{\chi_n}{T_e^{\frac{3}{2}}} \cdot \exp\left(\frac{\chi_n}{T_e}\right) \cdot E_1\left(\frac{\chi_n}{T_e}\right) \tag{8.9}$$

The rate coefficient for charge exchange recombination to the np upper level has been modelled to include the charge exchange with ground state hydrogen only as [57]:

$$\alpha_{cx_n} = c_{cx}\left[\exp\left(-\frac{\mid n - 9.1 \mid^2}{T_e^{.388}}\right)\right] \tag{8.10}$$

where c_{ex}, c_{rr}, and c_{cx} are different dimensional coefficients specific to the model used for each process, f_n is the oscillator strength and ΔE_n is the energy of the 1s-np transition, χ_n is the ionization potential of the upper level, and E_1 is the exponential integral function. The local emissivity of the 1s-np line can then be written as:

$$\varepsilon_n = n_e\left[n_{Ar16+} \cdot S_{ex_n} + n_{Ar17+} \cdot \alpha_{rr_n}\right] + n_{H^0}\left[n_{Ar17+} \cdot \alpha_{cx_n}\right] \tag{8.11}$$

From the functional form of the rate coefficients for each of the relevant processes it readily can be seen that a significant contribution from the charge exchange source will clearly be distinguishable from any other source. The rates for both electron impact excitation and radiative recombination vary approximately as $\frac{1}{n^3}$. That dependence appears explicitly in the expression for radiative recombination, and can be seen for electron impact excitation in Figure 8-2. where the dependence of f_n on n is shown [58].

The clearest demonstration of the charge exchange source was obtained by viewing emission along a chord passing through a known (or suspected) region of high neutral

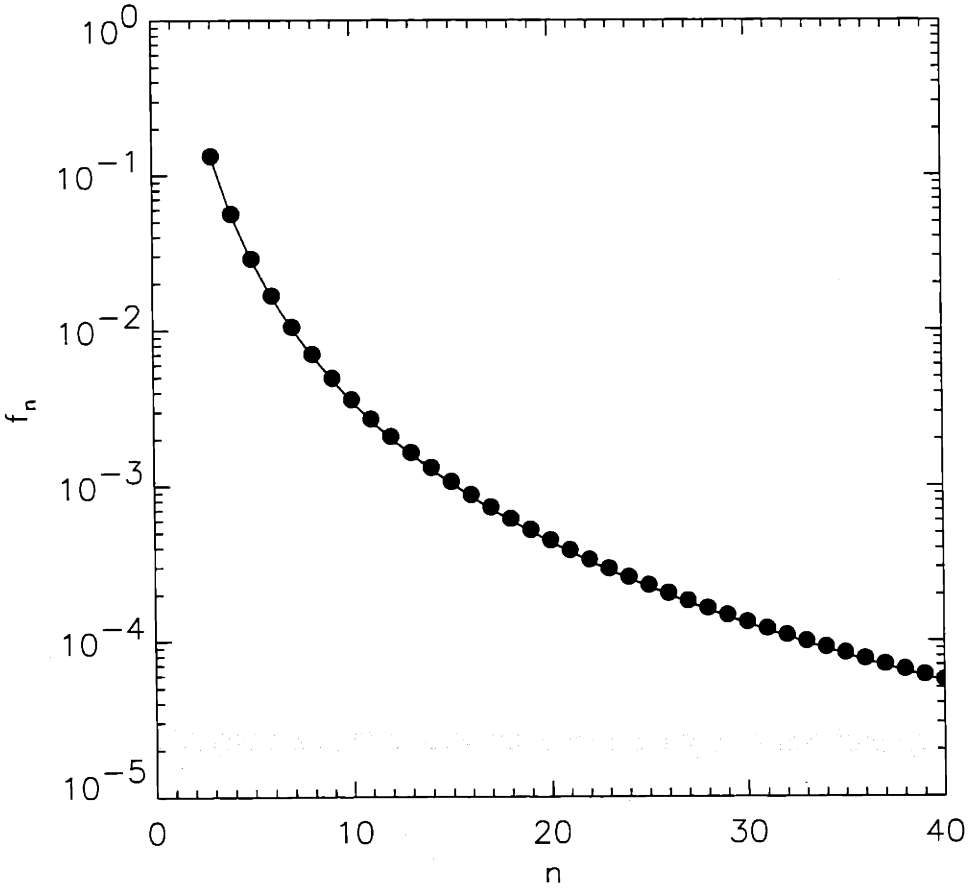

Figure 8-2: Oscillator strengths for electron impact excitation of 1s-np transitions.

density in the plasma. Such a region exists near the lower divertor x-point in typical diverted C-Mod discharges. The plasma midplane, on the other hand, is believed to be a region of substantially lower neutral density. A comparison of chords passing through each of these regions clearly demonstrates this distinction. Shown in Figure 8-3 is a typical diverted equilibrium with a well defined lower x-point. The plasma parameters for this discharge were $\overline{n_{e20}} \simeq 0.8$, $T_{e0} \simeq 2$ keV, $I_p \simeq 0.8$ MA. Also shown in that figure are the lines of sight of three chords from the HIREX spectrometer array, one of which looks through the center of the discharge, one which views the lower divertor region, and one which looks toward the upper region of the plasma. The time histories of the plasma current and the central heliumlike argon resonance line brightness measured with

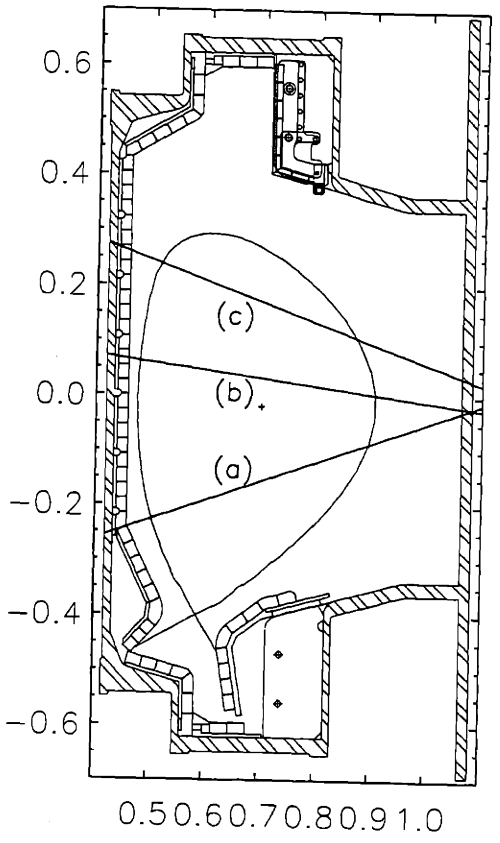

Figure 8-3: Plasma equilibrium and x-ray spectrometer lines of sight (a), (b), (c) for a diverted discharge.

the chord through the center of the plasma are shown in Figure 8-4. Shown in Figure 8-5 are the observed spectra of the 1s-np transitions of heliumlike argon as viewed along each chord, normalized in each case to the brightness of the $n = 6$ line. These spectra have been integrated in time over the entire shot. Most of the contribution, however, comes from times later than about 0.4 seconds when the amount of argon in the plasma was at its peak. The equilibrium during this integration time did not change appreciably. Clearly for chord (b) through the center there is very little, if any, observable brightness in the lines around $n = 9$ which appears above the $\frac{1}{n^3}$ trend determined by electron impact excitation and radiative recombination. The transitions around $n = 18$

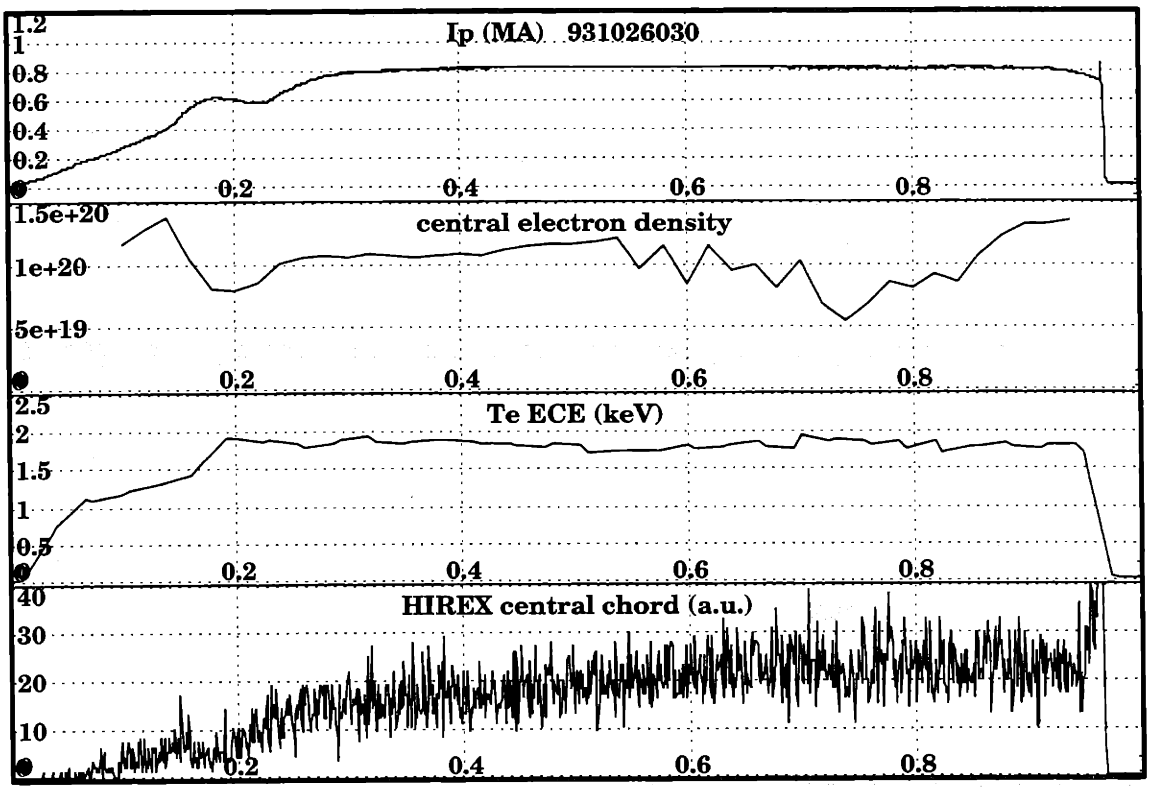

Figure 8-4: Plasma parameters for the diverted discharges used to measure neutral particle density profiles.

are not uniquely resolved, but nonetheless show nothing resembling a peak attributable to charge exchange recombination. Chord (a) through the lower divertor region, on the other hand, shows clear enhancement of both the $n \sim 9$ and $n \sim 18$ transitions due to charge exchange.

To quantify further the contributions to these observed brightnesses due to charge exchange, modelling using the MIST code was carried out. Using electron density and temperature profiles as measured by the TCI and ECE diagnostics respectively, the spatial density distribution of the various charge states of argon was first determined ignoring any effects of charge exchange (i.e. the neutral density was assumed to be zero everywhere). This modelling was done in the standard 1-dimensional geometry discussed earlier and did include transport coefficients appropriate to the background plasma conditions. From the charge state and neutral density profiles, the emissivity

of the 1s-np transitions can now be determined using the rate coefficients defined in Equations 8.8-8.10. The effect of the neutrals is significant both near the plasma edge and in the center for the lines near the resonant capture levels. It is this effect which allows this technique to be used for the determination of central neutral densities.

The FRANTIC neutral transport code was used to provide a self-consistent 1-dimensional neutral density profile for the specific plasma conditions under consideration. The code takes as input the background electron density and temperature profiles as well as the edge neutral particle flux. This flux is assumed to be symmetric in the cylindrical model geometry. The code then uses the input profiles to calculate local electron and ion impact ionization, volume recombination, and charge exchange rate coefficients for both first generation and multi-generation neutrals which are used to determine the overall neutral particle balance. The background electron density and temperature profiles measured for the discharges considered here are shown in Figure 8-6 along with the calculated neutral density profiles for different values of edge neutral density. In each case the energy of the first generation neutrals at the edge was chosen to be 2 eV. This value is an approximation of the Franck-Condon energy given to neutrals born of a dissociation of molecular hydrogen. The neutral density profiles calculated by the code are not highly sensitive to this value of edge neutral energy.

There is an obvious difficulty in using a one-dimensional code to model an inherently two-dimensional quantity. A single radial profile will never be sufficient to model the entire plasma. Some assumptions must therefore be made in order to render this problem into a tractable form. As discussed earlier, it is reasonable to assume that the electron density and temperature are flux functions inside the separatrix and can therefore be adequately modelled in one dimension only. The relevant gradients of density and temperature are really gradients in flux space, not physical space. A further reasonable assumption is that the density of a given impurity charge state is also a flux function. This is true so long as parallel transport is fast enough to equilibrate density on a flux surface despite the presence of toroidally or poloidally localized impurity sources. Since

the parallel velocity is fast even for impurities, the time scale for this equilibration is on the order of microseconds which is much faster than the relevant diffusive time scale. Of all the quantities of interest, therefore, it is only the neutral density itself which cannot reasonably be described by a one-dimensional function.

One way around this difficulty is to simply compare what the expected brightnesses of various lines influenced by charge exchange would be along different lines of sight for a given 1-D neutral density profile. If there is consistency among the predicted and observed brightnesses along those lines of sight, then the given profile would be deemed sufficient to describe the neutrals in all regions of the plasma. If, however, inconsistencies exist between predicted and observed brightnesses, then it is clear that the same profile cannot describe the neutral in all regions of the plasma.

The procedure for analyzing these data was therefore to begin by modelling one of the three chords with 1-dimensional profiles and then comparing model predictions for the same profiles as viewed along the other instrumental lines of sight. To this end, a value of edge neutral density was chosen as input the the FRANTIC code such that the resulting neutral density profile gave good agreement with the observed charge exchange spectrum along the chord looking near the divertor region (chord a). The edge density required as input for this best fit was $1 \times 10^{16} m^{-3}$. Agreement with the observed spectrum was good for the n=9 line where the model is most accurate. This neutral density profile was then used to generate a synthetic spectrum along chords b and c as well. It was the case that the neutral density profile which best approximated the observations along the lower chord greatly overestimated the charge exchange contribution along the chords looking at the midplane and toward the top of the plasma. It is on this basis that it can be concluded that a lower neutral density must be present in those regions.

8.3.1 Diverted/Limited Discharge Comparison

The large up/down asymmetry in the neutral density profile described above was observed during diverted discharge operation. A series of limited discharges with identical plasma

parameters (electron density, temperature, plasma current) was also run in order to investigate whether this asymmetry was also present for limited equilibria. Shown in Figure 8-8 is the magnetic geometry for these limited discharges along with the three chordal views used in this case. Summarized in Figure 8-9 are the brightnesses of the high-n lines along those three chords, again normalized to the brightness of the n=6 lines. Whereas in the diverted case the asymmetry was quite noticeable by looking at the brightnesses alone, it can now be seen that this is no longer obviously the case. The chords looking above and below the midplane now seem to show similar charge exchange enhancement effects in the lines around n=9. In fact, the neutral density profiles which give a best fit to these observed spectra are actually quite similar. The best-fit profiles imply a very small (less than a factor of 2) up-down asymmetry in the limited discharges. The up-down asymmetry in the diverted discharges was found to be at least a factor of 10.

These differences may be understood through a consideration of the neutral sources during each type of discharge. For the limited case, the plasma separatrix is in fact in contact with the inner wall along most of its inboard extent (see Figure 8-8). The recycling source of neutrals is therefore dominated by the inner wall. Since the contact is relatively symmetric, it is perhaps not surprising that the deduced profile is also somewhat symmetric. This is in marked contrast with the source locations during diverted operation (recall Figure 8-3) when there is greatly reduced contact between the plasma and the inboard wall.

8.3.2 Comparison with Other Diagnostics

As mentioned earlier, there is a limited number of techniques available for measuring the edge neutral density, and even fewer for measuring the central neutral density. Where available, however, attempts were made to compare the results obtained with these various methods. Neutral pressure is routinely measured at the plasma midplane and in the divertor region [59]. Shown in Figure 8-10 are the gauge locations. The midplane gauge

is a standard Bayerd-Alpert ionization gauge which has been modified to allow for faster time response and the divertor gauge is an Asdex-type linear ionization gauge specifically designed to operate in a high magnetic field environment. While these gauges provide a direct measurement of cold molecular hydrogen density, an atomic neutral density can nonetheless also be estimated. Since these measurements are remote from the plasma separatrix, some modelling of the ionization of the neutrals between the gauge position and the separatrix is required to make a proper comparison. For the low density diverted discharges investigated, the neutral pressure at the midplane was typically measured to be about 0.1 mTorr of D_2. Using an appropriate conversion factor [60], this corresponds to an atomic neutral density at the midplane gauge location of about $2 \times 10^{18} m^{-3}$. If the scrape-off layer density and temperature profiles are assumed known, then the attenuation of this neutral density can be approximated using the FRANTIC code calculations of the appropriate atomic processes. The profiles of electron density and temperature in the SOL are measured by the fast-scanning probe. The resulting attenuation of the neutrals as calculated by FRANTIC has shown that the value of neutral density at the separatrix is very similar to the midplane neutral density inferred through the consideration of charge exchange with argon. This agreement therefore lends confidence to the modelling carried out in the analysis of the high-n spectra. The divertor gas gauge similarly provides a neutral density remote from the plasma, although the modelling to extrapolate to a value at the separatrix is more difficult due to the greater uncertainty in the electron density and temperature profiles in the private flux region of the divertor. The measured neutral density at the divertor gauge location is found to be about 1 mTorr during the diverted discharges under investigation. While this factor of 10 difference in neutral pressure between the divertor and the midplane appears to be consistent with the differences in neutral density measured with the charge exchange technique during divertor operation, it is not obvious that the results can be compared directly, since different quantities are being measured in each case.

8.4 Conclusions

A technique for determining the neutral density profile on the basis of observations of charge exchange recombination with impurity ions has been demonstrated for low density discharges in Alcator C-Mod. During diverted operation, strong up-down asymmetries were observed in chordal measurements made above and below the plasma midplane. The inferred edge neutral densities in these cases were found to be in general agreement with measurements based on neutral pressure and H_α emission. Much weaker asymmetries were observed during limited operation. The agreement with other edge measurements in these cases was also generally good.

While this technique is dependent on the atomic physics modelling, it nonetheless provides one of the few available measurements of central neutral densities. As the temperatures in Alcator C-Mod increase to central values above about 2.5 keV, these measurements will become easier to make due to the increased amount of hydrogenlike argon which will be present in the plasma. The measurement of the neutral density profiles should then be readily available over a larger range of electron densities. This may become particularly important in the investigation of central neutral particle behaviour during the detached divertor condition.

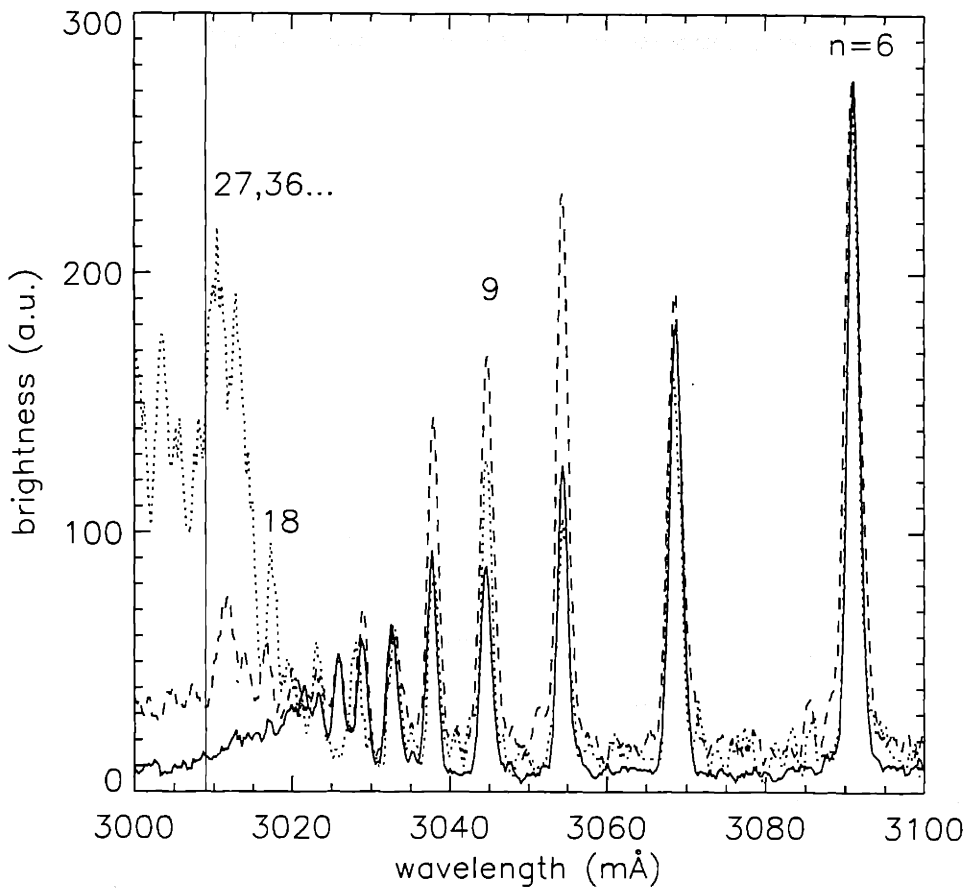

Figure 8-5: Various 1s-np transitions (n $\geq$ 6) from chords (a)–dashed, (b)–solid, and (c)–dotted shown in Figure 8-3. Notice the enhancement on the brightness of the n=8,9,10 transitions in the chord looking toward the lower divertor. Also notice the prominent recombination edge in the spectrum taken from chord (c) at about 3009 Å.

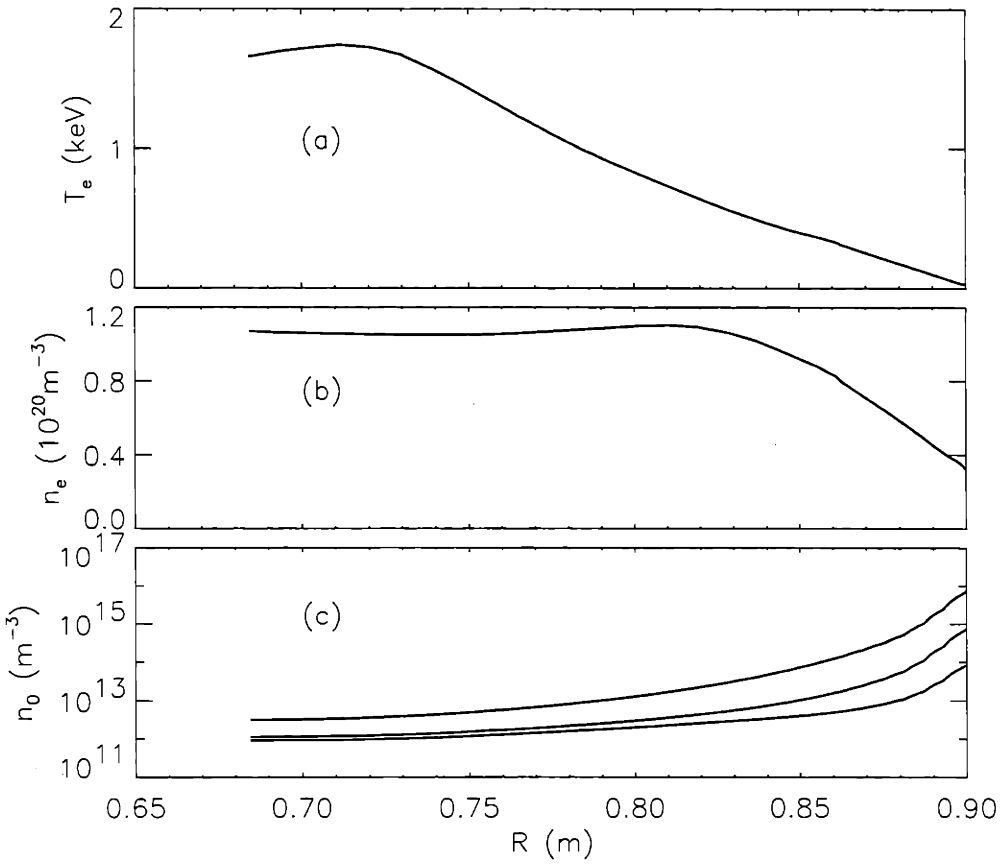

Figure 8-6: Electron density (a) and temperature (b) profiles used as inputs for the FRANTIC code along with calculated neutral density (c) profiles for different values of edge neutral source.

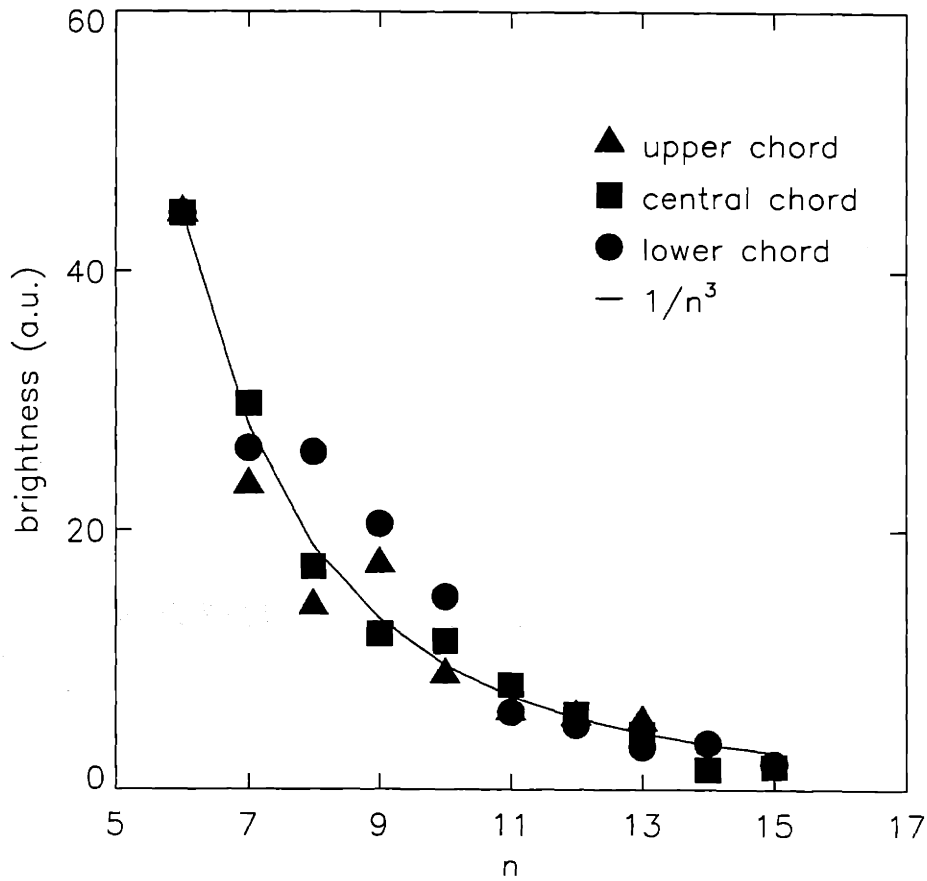

Figure 8-7: Observed brightness of high n argon transitions along different chords in a diverted discharge.

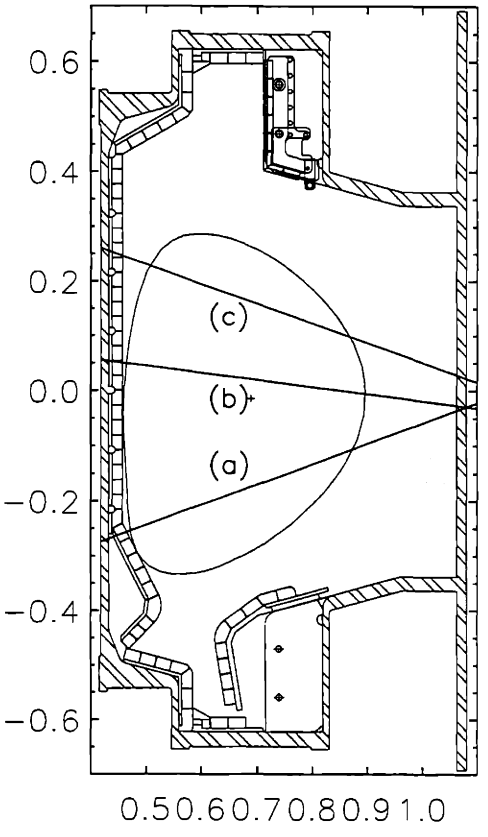

Figure 8-8: Plasma equilibrium and x-ray spectrometer lines of sight (a), (b), (c) for a limited discharge.

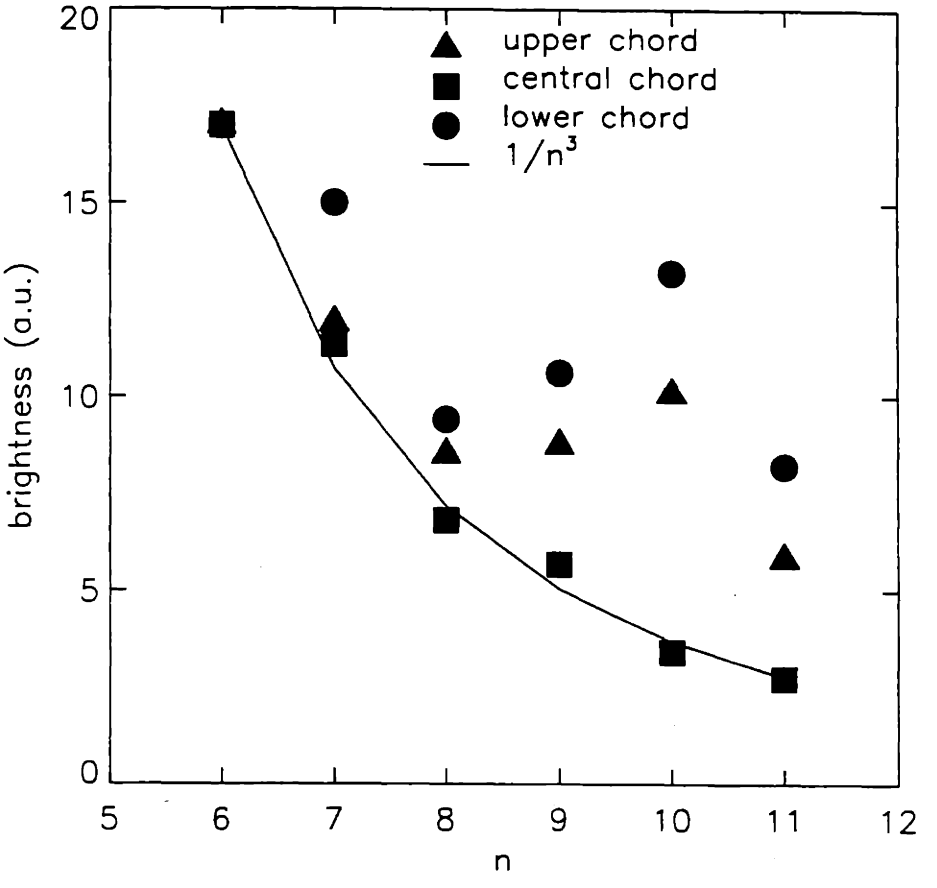

Figure 8-9: Observed brightness of high n argon transitions along different chords in a limited discharge.

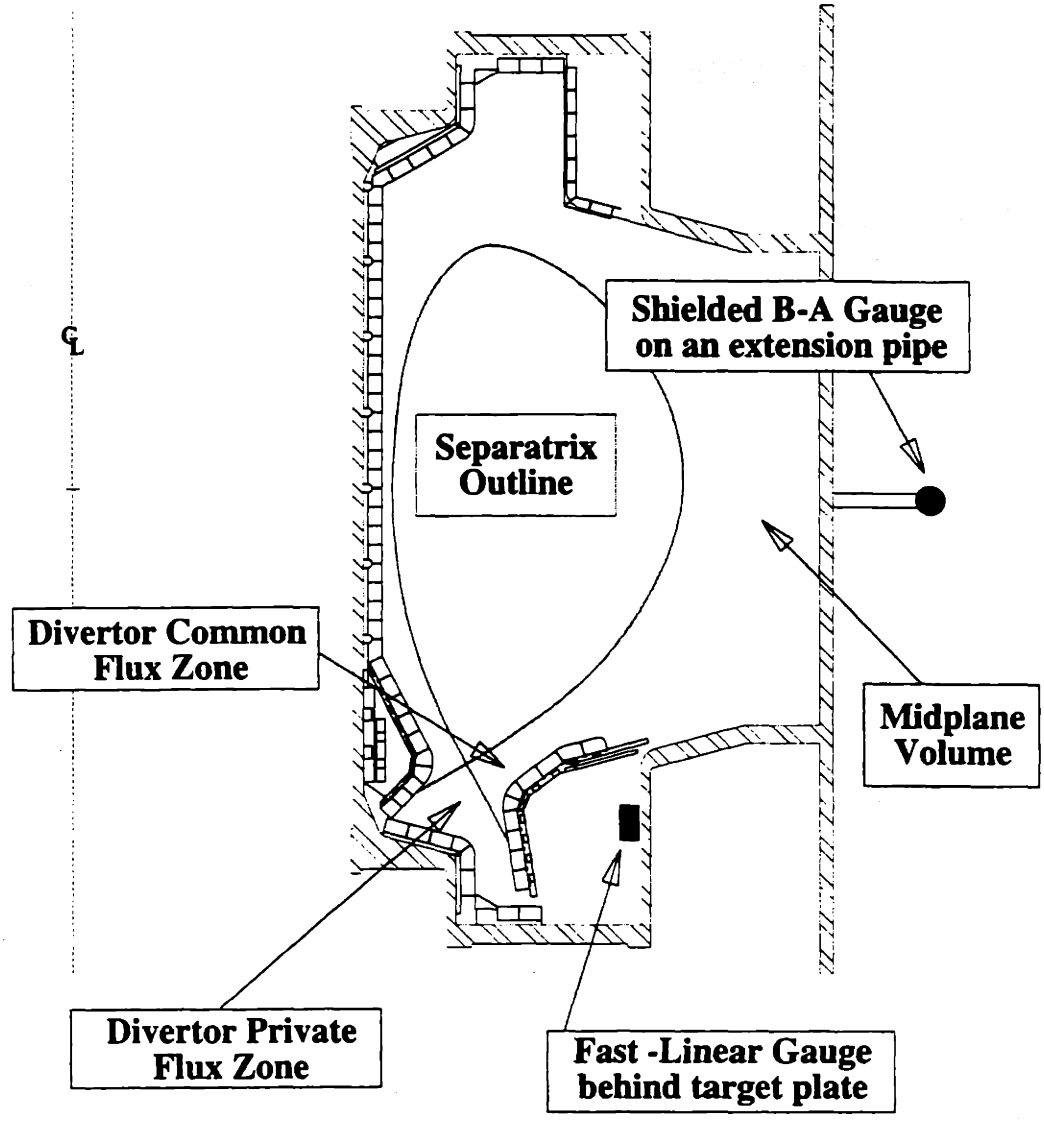

Figure 8-10: Neutral pressure gauge locations.

Chapter 9

Summary and Future Work

The preceding chapters have described a number of experiments which all contribute to a better understanding of impurity behaviour in tokamaks. An overall summary of the key results obtained and their larger significance is therefore appropriate at this time.

Many of the experiments which have been conducted have relied on the laser ablation impurity injection system developed in part by the author. This injection system has provided a reliable and reproducible means of injecting trace amounts of non-recycling impurities into the plasma. The injection system was used to make measurements of the impurity particle confinement time during a variety of plasma operating conditions. Scaling relationships were developed to describe the confinement time dependence on plasma parameters such as current, electron density, mass of the working gas, total input power, and others. As development of C-Mod continues into new operating regimes, these same techniques will be used to characterize further the impurity transport. Important questions regarding this transport will be answered for a host of new operational scenarios such as high field, high input power, and H-mode.

Once the impurity transport had been measured, the MIST transport code could be used to infer intrinsic impurity concentrations in the plasma more effectively. With this code, enough data were analysed to allow for substantial improvements to be made to the database of atomic physics rate coefficients for molybdenum. The analysis has

progressed to the point that the charge state balances now modelled are able to predict spatial profiles of high charge states of molybdenum which are in good agreement with observations. Further development needs to be done to extend this good agreement to a radiated power model as well.

A believable transport model also allowed experiments which measured the screening efficiency of the plasma to be performed for a variety of discharges. These measurements are important to the development of techniques to allow for power dissipation in the divertor on a mantle of highly radiating impurities. Initial measurements of this screening have indicated that large amounts of impurities can be injected at the edge of the plasma without too large an impurity concentration building up in the main plasma. Continued experiments which make use of this finding to exploit the injections of these impurities to meet operational goals are underway.

Further application of the transport model has allowed measurements of the neutral hydrogen density profile in the plasma to be made. These measurements represent one of the only ways that the core neutrals in C-Mod can presently be diagnosed. Use of this technique has led to the observation of strong up-down asymmetries in the core neutral density profile during diverted operation. This is consistent with similar observations of neutral density made at the edge of the plasma. Continued measurement of these profiles during a variety of discharges is ongoing and is hoped to yield new insight into neutral transport in diverted tokamaks.

Appendix A

Molybdenum Rate Coefficients

A.1 Ionization Rates

The ionization rates for molybdenum were fit to the function:

$$S_{iz} = a_0 \exp\left(-\frac{a_1}{T_e}\right) \tag{A.1}$$

The coefficients for charge states 24+ through 33+ are listed in Table A.1.

A.2 Recombination Rates

The radiative recombination rates for molybdenum were fit to the function:

$$\alpha_{rr} = \frac{b_0}{T_e} \exp\left(-\frac{b_1}{T_e}\right) \tag{A.2}$$

The coefficients for various charge states from 25+ through 34+ are listed in Table A.2.

The dielectronic recombination rates for molybdenum were fit to the function:

$$\alpha_{dr} = \frac{c_0}{T_e^{c_2}} \exp\left(-\frac{c_1}{T_e}\right) \tag{A.3}$$

The coefficients for charge states 25+ through 34+ are listed in Table A.3.

charge	a_0	a_1
24+	22.0679	1.15353
25+	19.8665	1.30640
26+	16.9559	1.69036
27+	14.6461	1.76592
28+	12.5175	1.87073
29+	10.3965	1.95117
30+	8.2819	1.95120
31+	6.3011	2.08120
32+	4.6559	2.25460
33+	1.76065	4.16832

Table A.1: Coefficients of the fit for the ionization rate of potassiumlike to fluorinelike molybdenum.

charge	b_0	$b_1(10^{-2})$
25+	2.7946	3.38845
26+	3.10658	3.4494
31+	5.32054	5.9862
32+	5.2730	3.5830
33+	5.7528	3.65479
34+	7.15647	7.45482

Table A.2: Coefficients of the fit for the radiative recombination rate of selected charge states from argonlike to oxygenlike molybdenum.

charge	c_0	$c_1(10^{-2})$	c_2
25+	15.3985	2.72389	1.1
26+	13.6420	3.70976	1.1
27+	10.3001	4.55019	1.15
28+	10.1289	5.75578	1.15
29+	9.58956	5.87206	1.1
30+	8.85118	5.22668	1.0
31+	9.63309	26.7537	1.0
32+	12.9415	80.8415	1.25
33+	9.57859	145.518	1.3
34+	10.4122	94.2598	1.3

Table A.3: Coefficients of the fit for the dielectronic recombination rate of argonlike to oxygenlike molybdenum.

Appendix B

General Rate Coefficients

B.1 Heliumlike Model

The collisional-radiative model used to describe the heliumlike ions which are observed in Alcator C-Mod is presented here. Elements up to about Z=22 (V) are easily stripped to the heliumlike charge state at temperatures of about 1 keV. The HIREX spectrometer array covers a wavelength range in which many strong lines from the heliumlike system radiate. As a result, this system is one which has a great deal of experimental data available for validation of the model.

The processes by which upper levels in the system are populated include, electron impact excitation, radiative and dielectronic recombination, inner-shell ionization from the lithiumlike state, cascades from charge exchange population of higher levels, and collisional coupling between levels. Electron impact excitation from the ground state was modelled according to the formalism found in Mewe [61]. The rate coefficient in cm^3/s for this process is:

$$S_{ex} = a_c \cdot 8.2 \times 10^{-7} \Omega \frac{1}{E_{ij}\sqrt{T_e}} e^{-\frac{E_{ij}}{T_e}} \tag{B.1}$$

where

$$\Omega = A + (B\frac{E_{ij}}{T_e} - C\left(\frac{E_{ij}}{T_e}\right)^2 + D\left(\frac{E_{ij}}{T_e}\right)^3 + E) \cdot g + (C+D)\frac{E_{ij}}{T_e} - D\left(\frac{E_{ij}}{T_e}\right)^2 \tag{B.2}$$

label	λ (Å)	E_{ij} (eV)	A	B	C	D	E	a_c
w	40.27	307.9	0.50	0	0	0.20	3.48	1.05
x	40.70	304.6	0	0	1.11	-0.25	0	1.065
y	40.73	304.4	0	0	0.67	-0.15	0	1.065
z	41.49	298.8	0	0	0.60	-0.17	0	—
f	—	304.2	0.80	-0.55	0	0	0	1.11
o	—	304.2	0	0	0.22	-0.05	0	1.065

Table B.1: Excitation rate parameters for selected lines of heliumlike carbon.

label	λ (Å)	E_{ij} (eV)	A	B	C	D	E	a_c
w	3.9492	3139.4	0.73	0	0	0.30	4.12	1.05
x	3.9660	3126.1	0	0	1.11	-0.17	0	1.065
y	3.9694	3123.4	0	0	0.67	-0.10	0	1.065
z	3.9943	3103.9	0	0	0.60	-0.20	0	—
f	—	3124.6	0.80	-0.40	0	0	0	1.11
o	—	3122.6	0	0	0.22	-0.034	0	1.065

Table B.2: Excitation rate parameters for selected lines of heliumlike argon.

where

$$g = \ln\left(\frac{\frac{E_{ij}}{T_e}+1}{\frac{E_{ij}}{T_e}}\right) - \frac{\left(0.36+0.3\sqrt{\frac{E_{ij}}{T_e}+.01}\right)}{\left(\frac{E_{ij}}{T_e}+1\right)^2} \tag{B.3}$$

and a_c is a multiplier which accounts for cascades from higher levels which are populated by electron impact excitation as well. Values of the parameters A, B, C, D, E, and E_{ij} for carbon, argon, and scandium can be found in Tables B.1, B.2, and B.3 for the strongest lines observed in this system. The notation used for labelling the lines is standard [55]. w refers to the resonance (1s-2p) line in the singlet system. x and y are intercombination lines resulting from radiative transitions of the type 1s-2p in the triplet system. z is the forbidden ($\Delta n = 0$) line. f and o are non-radiative transitions which must nonetheless be included in order to maintain the correct population balance.

A set of equations which account for all of the processes mentioned above can now be generated. In general, the population of upper level k which is denoted by N_k can be described by:

$$N_k\left(A_k + A_{kl} + n_e S_{cc_{kl}}\right) = n_e\left(n_{He}S_{ex_k} + n_H\alpha_k + n_{Li}S_{iz_k} + N_l S_{cc_{lk}}\right) \tag{B.4}$$

label	λ (Å)	E_{ij} (eV)	A	B	C	D	E	a_c
w	2.8731	4315.2	0.75	0	0	0.31	4.17	1.05
x	2.8832	4300.1	0	0	1.0	-0.15	0	1.065
y	2.8870	4294.4	0	0	0.80	-0.12	0	1.065
z	2.9028	4271.0	0	0	0.60	-0.20	0	—
f	—	4295.7	0.80	-0.40	0	0	0	1.11
o	—	4293.4	0	0	0.20	-0.030	0	1.065

Table B.3: Excitation rate parameters for selected lines of heliumlike scandium.

where the A_k and A_{kl} terms refer to the spontaneous decay coefficients between level k and the ground state or adjacent states respectively and α_k is the total recombination rate which populates level k. The rate $S_{cc_{kl}}$ refers to the collisional coupling between states k and l. The rate S_{iz_k} is the inner shell ionization rate of the lithiumlike species which populates level k. Expressions for these terms are found in [55]. Solving the set of equations generated by B.4 yields the populations of all upper levels k. The emissivity of the given line which is used to compare with observations is then simply $N_k A_k$.

B.2 Lithiumlike Model

Also of importance are lines in the lithiumlike ionization state. These were modelled using the formalism of [55]. Small differences in the rate coefficient expressions are noted below:

$$S_{ex} = 1.58 \times 10^{-5} f_{ij} \Omega \frac{1}{E_{ij}\sqrt{T_e}} e^{-\frac{E_{ij}}{T_e}} \tag{B.5}$$

where

$$\Omega = A + (B\frac{E_{ij}}{T_e} - C\frac{{E_{ij}}^2}{T_e} + D) \cdot g + C\frac{E_{ij}}{T_e} \tag{B.6}$$

where g is as given in equation B.3. Values of the parameters A, B, C, D, f_{ij}, and E_{ij} are found in Tables B.4 and B.5 for neon and scandium respectively. In each case, five lines were modelled. These included the 2s-2p resonance lines for $j = \frac{3}{2}, \frac{1}{2}$, as well as transitions between 2s-3s, 2s-3p, and 2s-3d.

A set of equations which account for all of the processes mentioned above can now

transition	λ (Å)	E_{ij} (eV)	f_{ij}	A	B	C	D
2s-2p (3/2)	770.4	16.09	0.102	0.650	0.895	-0.429	0.28
2s-3s	103.5	120.3	0.298	0.157	0	0	0
2s-3p	88.13	140.7	0.298	-0.279	0.666	-0.189	0.28
2s-3d	98.31	126.1	0.298	0.485	-0.195	0	0
2s-2p (1/2)	780.3	15.89	0.0502	0.650	0.895	-0.429	0.28

Table B.4: Excitation rate parameters for selected lines of lithiumlike neon.

transition	λ (Å)	E_{ij} (eV)	f_{ij}	A	B	C	D
2s-2p (3/2)	279.8	44.4	0.0522	0.68	0.96	-0.47	0.28
2s-3s	20.0	621.2	0.367	0.128	0	0	0
2s-3p	16.1	771.7	0.367	-0.304	0.797	-0.239	0.28
2s-3d	17.1	726.5	0.367	0.403	-0.143	0	0
2s-2p (1/2)	326.0	38.1	0.0220	0.68	0.96	-0.47	0.28

Table B.5: Excitation rate parameters for selected lines of lithiumlike scandium.

be generated in a manner analogous to but simpler than that of the heliumlike system. In general, the population of upper level k which is denoted by N_k can be described by:

$$N_k \left(A_k + A_{kl} + n_e S_{cc_{kl}}\right) = n_e \left(n_{Li} S_{ex_k} + N_l S_{cc_{lk}}\right) \tag{B.7}$$

where, as before, the A_k and A_{kl} terms refer to the spontaneous decay coefficients between level k and the ground state or adjacent states respectively and the rate $S_{cc_{kl}}$ refers to the collisional coupling between states k and l. The system of equations B.7 can be solved to yield the emissivity profiles for each of these lines.

Bibliography

[1] G.G. Dolgov-Savel'ev, V.S. Mukhovatov, et al. *Soviet Journal JETP*, 11:287, 1960.

[2] I.H. Hutchinson et al. *Physics of Plasmas*, 1:1511, 1994.

[3] H.L. Manning. Technical Report PFC/RR-86-14, Plasma Fusion Center, 1986.

[4] J. Dolan. *Fusion Research.* Pergamon Press.

[5] M. Greenwald, J.L. Terry, et al. *Nuclear Fusion*, 28:2199, 1988.

[6] M. Murakami, J.D. Callen, and L.A. Berry. *Nuclear Fusion*, 16:347, 1976.

[7] I.H. Hutchinson et al. Technical Report PFC/RR-88-11, Plasma Fusion Center, 1988.

[8] L.L. Lao et al. *Nuclear Fusion*, 25:1611, 1985.

[9] J.E.Rice and E.S. Marmar. *Review of Scientific Instruments*, 61:2753, 1990.

[10] R.S. Granetz and L. Wang. In *Bulletin of the American Physical Society*, volume 37, page 1424, 1992.

[11] C. Christensen and E. Marmar. In *Bulletin of the American Physical Society*, volume 39, 1994.

[12] Keith H. Burrell. *Review of Scientific Instruments*, 49:948, 1978.

[13] J. Urbahn. PhD thesis, Massachusetts Institute of Technology, 1994.

[14] S.A. Cohen, J.L. Cecchi, and E.S. Marmar. *Physics Review Letters*, 35:1507, 1975.

[15] R. Koppmann, S.M Refaei, and A. Pospieszczyk. *Journal of Vacuum Science and Technology*, 4:79, 1986.

[16] Product sold by EG&G Reticon, Salem, MA 01970.

[17] Product sold by J.E. Manson Co. Inc., Concord, MA 01742.

[18] E.B. Saloman et al. *Applied Optics*, 19:749, 1980.

[19] J.L. Terry and H.L. Manning. Technical Report PFC/CP-86-11, Plasma Fusion Center, 1986.

[20] H. VanRegemorter. *Journal of Astrophysics*, 136:906, 1962.

[21] M.J. May. *Review of Scientific Instruments*, 66, 1995.

[22] E.S. Marmar, J.E. Rice, J.L. Terry, and F.H. Seguin. *Nuclear Fusion*, 22:1567, 1982.

[23] R.A.Hulse. *Nucl. Tech./Fus.*, 3:259, 1983.

[24] E.S. Marmar. PhD thesis, Princeton University, 1976.

[25] C. DeMichelis and M. Mattioli. *Nuclear Fusion*, 21:677, 1981.

[26] K. Fournier. *Physics Review A.* to be published.

[27] J.H. Irby et al. *Review of Scientific Instruments*, 59:1568, 1988.

[28] B. Labombard et al. *Review of Scientific Instruments.*

[29] B. Labombard. private communication.

[30] T.C. Hsu et al. In *Eighth Joint Wokshop on ECE and ECRH*, volume IPP III/186, page 409, 1993.

[31] K. Fournier. In *Bulletin of the American Physical Society*, 1994.

[32] J. Hugill. *Nuclear Fusion*, 23, 1983.

[33] K.W. Wenzel. PhD thesis, Massachusetts Institute of Technology, 1990.

[34] P.N. Yushmanov et al. *Nuclear Fusion*, 30, 1990.

[35] I.H. Hutchinson et al. *Plasma Physics and Controlled Fusion*, 36:B145, 1994.

[36] B. Labombard et al. In *Bulletin of the American Physical Society*, 1994.

[37] T.C. Luke. PhD thesis, Massachusetts Institute of Technology, 1994.

[38] F.H. Seguin, E.S. Marmar, and R. Petrasso. In *Bulletin of the American Physical Society*, volume 28, page 1120, 1983.

[39] J.E. Rice, F. Bombarda, et al. *Review of Scientific Instruments*, 66:752, 1995.

[40] D.E. Post, R.V. Jensen, et al. *Atomic Data and Nuclear Data Tables*, 20:397, 1977.

[41] Ian H. Hutchinson. *Principles of Plasma Diagnostics*. Cambridge University Press, 1987.

[42] E.R. Muller, G. Weber, F. Mast, et al. Technical Report 1/224, Max-Planck Institut fur Plasmaphysik IPP Report, 1985.

[43] J.A. Goetz. private communication.

[44] J.E. Rice, E.S. Marmar, et al. *Nuclear Fusion*, 24:329, 1984.

[45] Y. Takase et al. Technical Report PFC/JA-91-33, Plasma Fusion Center.

[46] D.G. Swanson. *Physics of Fluids*, 28:2645, 1985.

[47] D.G. Whyte et al. In *Bulletin of the American Physical Society*, 1994.

[48] G.M. McCracken, U. Samm, P.C. Stangeby, et al. *Nuclear Fusion*, 33:1409, 1993.

[49] G.M. McCracken and P.E. Stott. *Nuclear Fusion*, 19:889, 1979.

[50] D. Jablonski et al. In *Bulletin of the American Physical Society*, 1994.

[51] E.S. Marmar. private communication.

[52] C. Kurz et al. In *Bulletin of the American Physical Society*, 1993.

[53] R. Boivin. private communication.

[54] J.E. Rice, E.S. Marmar, E. Kallne, and J. Kallne. *Physics Review A*, 35:3033, 1987.

[55] R. Mewe. *Astronomy. & Astrophysics*, 20:215, 1972.

[56] R.C. Isler. *Nuclear Fusion*, 24:1599, 1984.

[57] R.K. Janev, D.S. Belic, and B.H. Bransden. *Physics Review A*, 28:1293, 1983.

[58] W.L.Wiese, M.W.Smith, and B.M.Glennon. *Atomic Transition Probabilities Volume I–Hydrogen Through Neon.* National Standard Reference Data Series, 1966.

[59] A. Niemczewski, B. Lipschultz, G.M. McCracken, and B. Labombard. In *Bulletin of the American Physical Society*, 1994.

[60] A. Niemczewski et al. *Review of Scientific Instruments*, 66:360, 1994.

[61] R. Mewe. *Astronomy. & Astrophysics*, 1980.